Development of a Real-Time Technique for In-Situ Measurement of pH in Capacitive Deionisation

Mathavan Tharman

A thesis submitted in fulfillment

of the requirements for the degree of Master of Engineering

Supervisor: Dr. Peter Kovalsky

School of Engineering

The University of Waikato

New Zealand

2025

Abstract

Capacitive Deionisation (CDI) as a desalination technique proves to be one of the most promising technologies owing to its simplicity and ease of manufacturability. The longevity of CDI depends on a number of factors, such as the ability of carbon to withstand Faradaic reactions to CO_2. Furthermore, like other technologies such as (reverse osmosis) RO and (electrodialysis reversal) EDR, scale formation is known to affect its hydraulic efficiency. The slow mineral deposition of magnesium and calcium carbonate is responsible for such phenomena. The extent of the problem is one where the hydraulic efficiency of the device drops well below 10%, a state where the device is considered to be at the end-of-life as it is too difficult to pump water through it. In the preliminary study we examined the performance of an industrial scale (membrane capacitive deionisation) MCDI module that has been in operation intermittently for 5 years to establish familiarity with the performance of a used module.

In the main study, we described a new technique for observing the chemical state within the spacer channel of a CDI cell, the part of the electrode that is prone to blockage. This new technique for the direct measurement of pH is based on colourimetric analysis of a novel synthetic formulation of a pH-sensitive dye dissolved in the electrolyte phase. The basis for this novel technique combined a simple optical microscope integrated with a microfluidic device. This microfluidic device containing a microreactor cell of 750 picolitres in size was fabricated to host the electrochemical reaction (electrode and electrolyte phases) demonstrated in this study that recreates the “CDI effect” of an industrial cell.

The pH indicator formulations were synthesised from a 1:1:2 ratio of phenolphthalein, bromothymol blue and methyl red in an ethanol solution. The pH indicator, which we denote as the standard formulation (SF), had a density of 0.93 kg/L and pH of 2.74. This was the formulation that was subsequently used in the main part of the study. The dye was characterised by visible range spectroscopy and subsequent conversion to (hue saturation value) HSV colourmap coordinates using the 1976 CIE (International Commission on Illumination) chromaticity model. This enabled the development of a range of pH-Hue relationships using best approximated by sigmoid functions. In the analysis of these functions, we investigated the sensitivity of the pH-Hue relationship to variation in the SF formulation due to selective electrosorption of the dye. It was shown that the variation in functions produced was not significant and that the general pH-Hue relationship did not break down into a non-usable form.

Application of the novel technique was initially performed on a membrane less cell configuration. The pH profile was investigated from a starting range of interest of pH 8 to 9 where scale formation occurs. In the second series of reactions, we demonstrated microreactor CDI configurations with varying degrees of membrane coverage from 12.5% to 100%. It was found that the pH variation in the spacer channel was minimal or non-existent across the full charge cycle from adsorption through to desorption. This indicates that obscuration of the carbon surface blocks the protons diffusing from the surface of the carbon where it is generated by way of the standard faradaic reaction in CDI or blocking co-ions from being expelled from the membrane that may result in speciation that affects the pH.

We recommend longer in-situ observation type studies be performed to confirm the speciation chemistry present in the spacer channel typical of many situations where electrodes are reducing in performance by way of fouling and scale formation.

Acknowledgements

First, I am grateful to my supervisor, Dr. Peter Kovalsky, for his guidance, support, and encouragement. His expertise, advice, and patience were significant in completing this thesis. I thank the University of Waikato for providing such dedicated staff who specialise in teaching students for the Master's Research Program.

I especially thank David Dickson for his assistance with the microreactor experiment and data analysis. I also thank my colleagues and fellow researchers (Jojo, Prashant, Enola, and Marko) for their help and for creating a positive research environment. I wish all the microfluidics team members good fortune for their success in their future assignments.

I am very thankful to my family and friends for their constant support and understanding. Finally, I thank my wife, Deepika, and my children for their support and sacrifice during this research tenure.

Thank you all for your contributions and support.

Declaration of Authorship

I declare that this thesis was produced as the sole author, and the work contained within is based on my own research. It contains no material previously published or written by another person.

T. Mathavan

MATHAVAN THARMAN

DATE: 21/01/2025

Table of Contents

List of Figures

List of Tables

1 Chapter – Introduction

1.1 Background

Freshwater for rural people is the biggest concern of this decade. Due to irreversible damages are done to the water supply ecosystem by rapid industrialisation and extensive urbanisation (Saquib, Gupta et al. 2022). This urbanisation and human lifestyle seriously impact the environment and people at the lower economic level. The needs of industrial and common people at a lower economic level can be met with this advancement. Countries with smaller population groups of Pacific islands are under more significant threat due to their remote geographical coastal location; their water supply has become scarce due to seawater intrusion. (Martyr-Koller, Thomas et al. 2021). Mismanagement of water resources and lack of research to date are the key reasons for 30,000 water-sanitation-related deaths per day. (Hukka, Katko et al. 2007). The weakness in water management and exploitation of legal constraints in developing countries like India (Narain 2000). Change in the weather patterns and significant rates of sea level rise (30mm per year) in tropical Pacific islands and the Indian Ocean (Church, White et al. 2006) will force people to depend on groundwater as the only source for their survival. One-third of the world's population is denied safe drinking water. (WHO 2019). Energy efficient operation is researched in this technology compared to conventional methods. Upon facing all these issues, such as the availability of water resources, Mismanagement of resources, weather change, and political exploitation, one remedy to counter all these issues is better technological advancement in water treatment.

This thesis is carried out to help reduce impacts on people and the environment through promising technology CDI in water treatment and enhance its longevity in service. The stages of thesis work consist of characterisation, Development of UI (universal indicator) dye, characterisation and development of DOTH (Direct observation of the Proton [H+]) method, and understanding proton movement in CDI stack. Contributions regarding proton movement in CDI further assist in studying the AC (activated carbon) electrodes in CDI technology and enhance academic knowledge in the CDI process.

1.2 Scope and Objectives

The aim of this study is to develop a new method, DOTH, to observe the spacer channel in CDI cells. The study focuses on understanding the movement of protons in terms of pH variation and faradaic reaction in relation to pH variation, which reflects the real-time changes that happen inside a CDI cell.

2 Chapter - Literature Review

2.1 Introduction:

This chapter provides a literature review on the role of CDI technology as an alternative to conventional methods. There is growing demand for membrane CDI technology (CDI) as the most feasible technique in cooling water treatment, and rural brackish water treatment compared to other available methods. This review section points out the development area in CDI research and implementation of CDI for faradaic reactions. All the available knowledge through the research and gaps to help further improve academic knowledge is discussed here—characterisation of CDI and micropore volume calculation by (electrical double layer) EDL model. The conventional water treatment methods and the effects of rapid industrialisation resulting in indirect global warming, freshwater shortage, and waterborne fatalities worldwide are discussed here.

Clean water access is a basic need of humanity, which is being denied at an alarming rate due to increasing global warming. Over the decades, various technology methods have been tried and found successful in water desalination. In this literature, we focus on how CDI technology has travelled through decades and has become an essential need in the present and future. Parallel options in CDI technologies are discussed as a viable option in developing innovative approaches towards hydrogen production, as the recent development in mCDI techniques provides a larger surface area in activated carbon electrodes. This, in turn, reduces the energy requirement to split the water and drastically reduces the emissions. Due to the best electrochemical performance and low production cost, activated carbon is most commonly used (Zhai, Zhang et al. 2022), with the aim of zero carbon emission. Desalination by thermal methods has high (capital expenditure)CAPEX and (operational expenditure) OPEX, 1-4 kWh/m^3 15-25 kWh/m^3 (Dykstra 2018). Theoretical minimum energy as applied pressure is twice as high as osmotic pressure; this energy requirement for pumps accounts for 40% of total energy consumption in an RO unit. (Energy 2019). Electrical ionosorption-based CDI technology consumes less energy than RO and thermal methods.

Global fresh water supply is reducing; in 2017, an alarming rate of unsafe water-related estimated deaths accounted for 1.2 million people, accounting for 2.2% of all deaths worldwide. Approximately 1.1 Billion people in the world are suffering without access to clean water; mCDI technology is proposed as a solution to Global water and food security concerns (Bales, Kovalsky et al. 2019).

Mincarb's system costs \$1500 per m^3/day for smaller capacities as of 2019, and it is \$5000 per m^3/day for larger capacities.

Another key application of this technology is Nitrate removal (Kim, Kim et al. 2013) In high fertilizer-leached groundwater in farming regions.

2.2 Change in Need for Clean Water: New Zealand and Other Parts of the World

Water access to billions of people will be problematic in the forthcoming decades. Clean water access is the fundamental right of every human in this world. One of the 17 United Nations' sustainable development goals is SDG-6, clean water and sanitisation. SDG-6 aims to achieve universal and equitable access to safe and affordable drinking water. (UNSGD-6)

Although New Zealand's drinking water quality is 100% mentioned in UN SDG Indicator data 6.1.1 2022, there are disturbing heavy metal contaminants like arsenic and nitrate in the drinking water. About 800,000 New Zealanders are supplied with nitrate contamination in drinking water, increasing the risk of colorectal cancer. (Richards, Chambers et al. 2022). Figure 1 shows the groundwater quality of New Zealand, and the trend shows the worsening conditions of contaminants such as different species of nitrogen, phosphorous, E-Coli, and chloride in the groundwater. New Zealand Herald published news about elevated levels of arsenic in Auckland's drinking water. (Herald 2024).

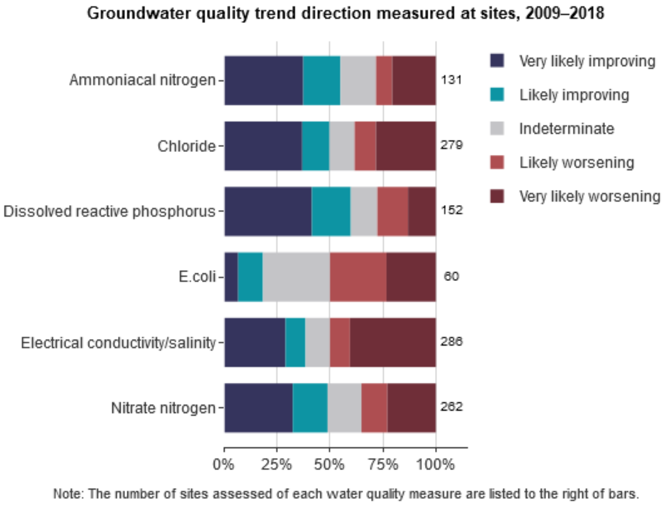

Figure 1 Groundwater quality of New Zealand trend (stats.gov.nz 2020)

These above challenges in access to clean water require a CDI technique as an alternative energy-efficient and cost-effective solution.

2.3 Desalination Methods

Several existing methods for desalination exist. The available desalination technologies are summarised in a table. Various factors, including pressure gradients, thermal gradients, and electrical potential gradients, influence each desalination process. These are outlined in Table 1.

Table 1 Overview of different desalination methods adapted from (Behnam, Faegh et al. 2022)

Technology	**Type**	**Driving Force**	**Key Parameters**
Reverse osmosis	Filtration	Pressure gradient	Feed pressure, temperature, Feed salt concentration, feed flow, Membrane characteristics
Forward osmosis	Filtration	Pressure gradient	The temperature of the draw solution, the velocity of feed and draw solution, membrane property
Membrane distillation	Filtration	Vapour pressure gradient	Feed flow temperature, mass flow rates, module geometric properties, membrane properties
Electrodialysis desalination	Filtration	Electrical potential gradient	Temperature and flow rate of feed flow, applied voltage, feed concentration, membrane properties
CDI	**Filtration**	**Electrical potential gradient**	**Electrode material, salt concentration, electrode specific surface area**
Solar Still	Thermal	Heat	Solar intensity, water depth
Humidification-dehumidification	Thermal	Heat	Mass flow of water to air, packing material, the top temperature of the cycle
Multistage flash distillation	Thermal	Heat	The temperature of the top brine, inlet, outlet, number of stages, temp
Adsorption desalination	Thermal	Heat	Heat source temperature, preheating time, adsorption/desorption time

As outlined in Table 1, the CDI filtration technique, which utilises an electrical potential gradient as its driving force, is further examined regarding technological improvements. Thermal desalination methods are often regarded as energy intensive. In contrast, CDI technology features key controlling parameters that are less complex than those of other methods. The primary factors influencing CDI technology include the properties of the electrodes, such as porosity, surface area, and micropore volume, along with operational parameters like applied voltage, adsorption/desorption cycle timing, and salt concentration.

2.4 mCDI Technology:

2.4.1 Introduction

Capacitive deionisation (CDI) technology is leading research focused on providing modern alternatives to traditional methods such as reverse osmosis, distillation, and other ion exchange filtration techniques. CDI is favoured for several reasons: it has lower energy consumption, is simple to operate, utilises favourable construction materials, and is easy to use. Improvements in electrode materials are anticipated to enhance energy efficiency further.

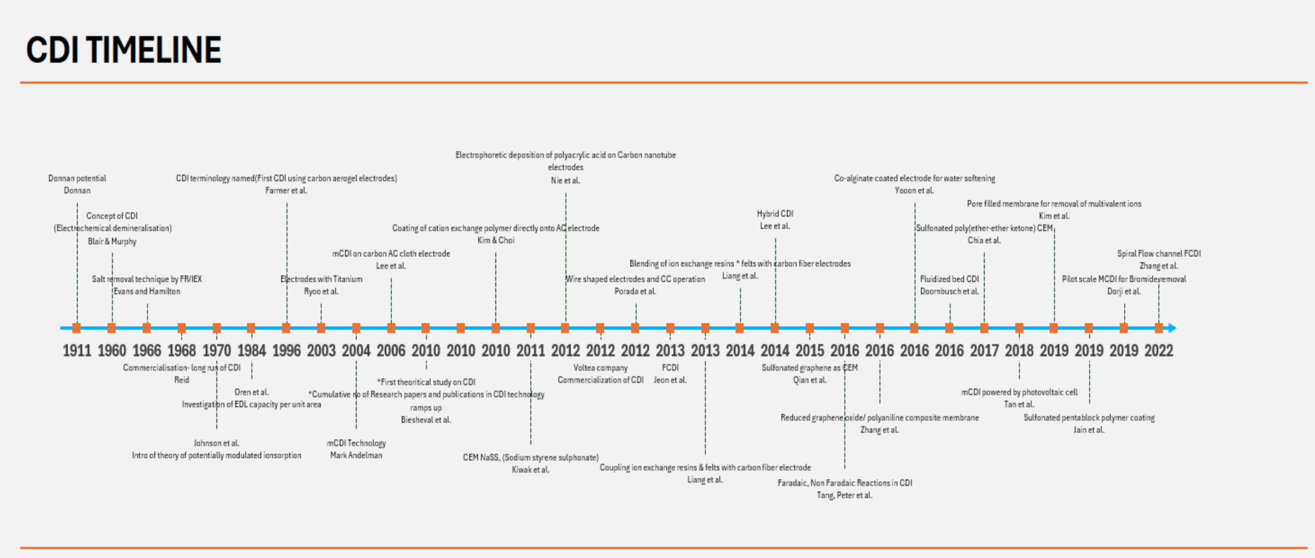

Figure 2 History of electrochemistry development into CDI technology

The 1911 Donnan Potential research marks the initial exploration into ionic equilibria and the nature of membranes (Aydogan Gokturk, Sujanani et al. 2022). In 1960, Blair and Murphy introduced the concept of electrochemical demineralisation of water. Since 2010, there has been a significant increase in research publications focused on this technology. In 2012, Voltea commercialised using mCDI for water treatment, highlighting the permselective characteristics of ion exchange (IEX) membranes at the interface with the solution (Aydogan Gokturk, Sujanani et al. 2022). Today, there is a growing demand for applications in various industries, including cooling towers, water softening, and nitrate removal, positioning the CDI technique as a preferred area for further research and advancement. Figure 2 illustrates the evolution of CDI technology from the Donnan potential to recent advancements.

2.4.2 Concept of CDI

Ionic adsorption is a key process in CDI. This system consists of two porous carbon electrodes arranged in a stack between spacer channels and ion exchange membranes. The process relies on the formation of the EDL, where salt ions are adsorbed into the micropores of the carbon electrode structure. Once the micropores become saturated with salt ions, the electrode's polarity is reversed, releasing the salt ions back into the bulk solution. This process regenerates the electrode for the next adsorption cycle, as illustrated in Figure 3. Due to the inert nature of porous activated carbon, thousands of operational cycles can be performed for water desalination without significant material loss. The EDL concept is also used to characterise the micropores within the activated carbon.

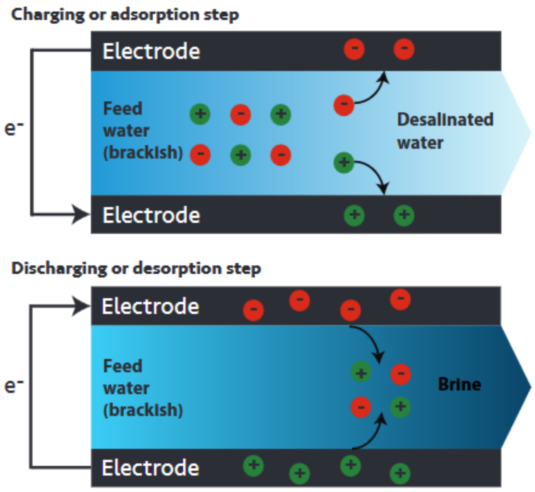

Figure 3 CDI unit adsorption/desorption cycle with opposite ions attraction and repulsion (Dykstra 2018)

The mCDI is an advanced form of CDI technology. Ion exchange membranes act as a barrier during adsorption and desorption, selectively allowing cations or anions in the electrode; during the reverse cycle, this protects against re-entering to the opposite electrode, optimising energy consumption and operating efficiency. There are two basic modes of operation: single pass and batch mode (Porada, Zhao et al. 2013). Adsorption and desorption cycles technically act as charge-discharge of electrodes.

The cycle duration determines the approach to the equilibrium salt concentration in electrodes the maximum salt adsorption capacity.

Constant voltage and constant current operation models are given in Figure 4. Figure 5 shows the modes of operation.

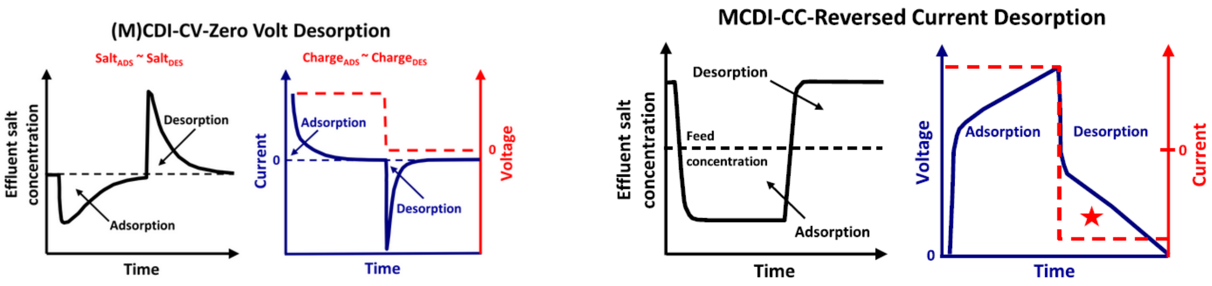

Figure 4 mCDI Single pass constant voltage and constant current operation model (Porada, Zhao et al. 2013)

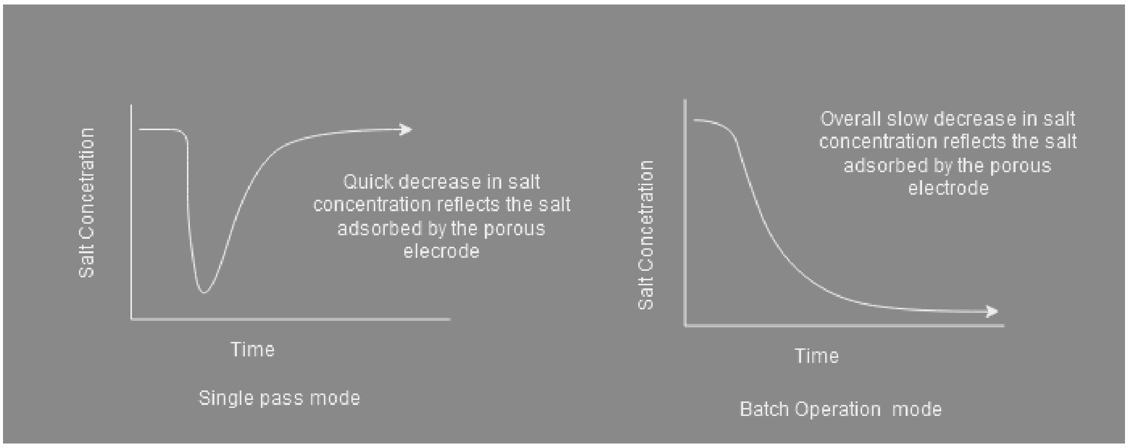

Figure 5 The batch mode and single-pass mode, Salt concentration vs. time graph, is adapted from Porada et al. (Porada, Zhao et al. 2013)

2.4.3 Activated Carbon Electrode

The porous carbon electrode internal structure consists of macropores (>50nm), mesopores (2-50nm), and micropores (<2nm) (Dykstra 2018). The macropore and mesopore act as a pathway for ion transportation into the EDL layers. Micropores are the objective area where the intra-particle pores create EDL while applying the potential difference; ions are pulled in and stored in the form of capacitance. It is imperative to have a more micropore structure at the proper pore size to accommodate more ions in the EDL. The overall desalination performance depends on this physical property as per Appendix 9.2. ACs are derived from coconut shell, wood, coal, and starch, and their combination of high specific surface area (SSA) (1000-3500m^2/g with low cost (approx. 0.5$/Kg) makes them a high priority among other electrode resources (Porada, Zhao et al. 2013). Their activation method contributes to micropore structure. Further electrode forming techniques like high shear mixing with binder or flocculation with polytetrafluoroethylene (PTFE) binders play a vital role in electrode conductive property and strength.

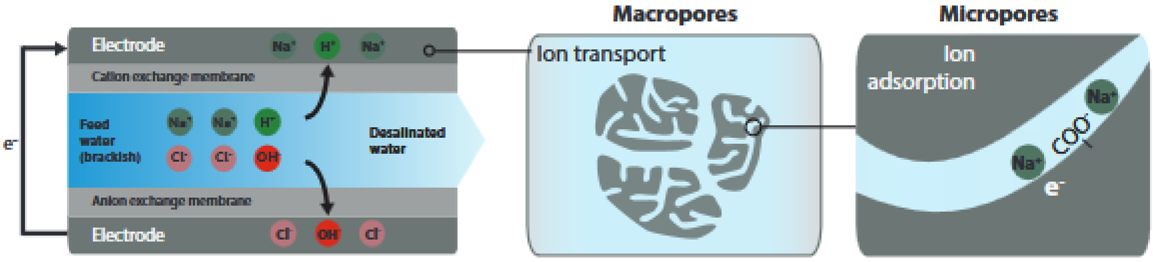

Figure 6 Macropore and micropore structure of porous activated carbon (Dykstra 2018)

2.4.4 Electro sorption Theory and Ion Transport Model

The mass transfer unit operation occurs in the form of ion adsorption in CDI. A modified Donnan model explains ions from the electrolyte to the porous electrode during CDI cycles with an overlapping EDL concept where potential and micropore volume become constant. The Debye length is much larger than the typical micropore size (1-2 nm range) (Porada, Zhao et al. 2013), this method helps to describe charge and salt adsorption theory accurately, hence electrode mass transport theory.

During the adsorption (Charging) cycle, the cation Na$^+$ is attracted to the cathode. (Porada, Zhao et al. 2013) (negatively charged electrode) and Cl$^-$ is attracted to the anode (positively charged electrode). When the polarity is reversed, which is called the desorption (discharging) cycle, the ions are pushed back to the bulk electrolyte, as mentioned in Fig 6.

The ionic charge density (σ_{mi}) in the intra-particle micropore is characterised by the equation below,

$$v_{mi} \times \frac{d\sigma_{mi}}{dt} = J \times A \qquad [1]$$

where J is the current density mol/m^2/s. Total moles of salt in the system conserved

$$v_{tot}C_o + v_{mi}C_{ions,mi,0} = v_{tot}C + v_{mi}C_{ions,mi} \quad = \quad v_{mi}\gamma \qquad [2]$$

$$C_{ions,mi} = \sqrt{\sigma_{mi}^2 + (2.c.\exp(m_{att}))^2} \qquad [3]$$

The current density, salt concentration c, effective total transport coefficient k (m/s) and voltage drop (which drives the mass transfer, applied voltage – voltage in EDL) $\Delta\phi_{tr}$ relation,

$$J = k.c.\Delta\phi_{tr} \qquad [4]$$

$$J = k.c.\left[\frac{V_{cell}}{V_T} - \frac{2.\sigma_{mi}.F}{C_{St,vol}.V_T} - 2.asinh\frac{\sigma_{mi}}{2.c.exp(m_{att})}\right] \qquad [5]$$

The adsorption isotherms are based on the Langmuir and Freundlich equation to fit the model.

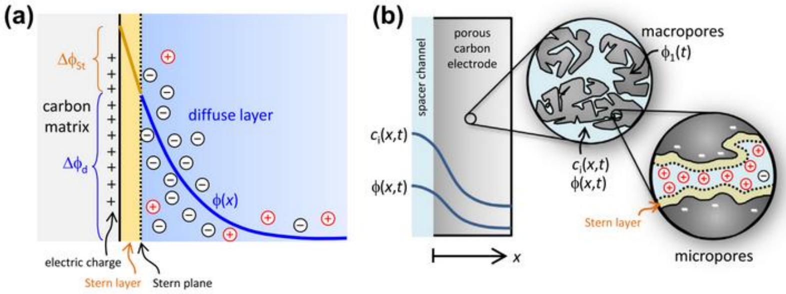

Figure 7 Models for charge and ion storage in porous CDI electrode a) EDL structure according to Gouy Chapmen Stern theory. b) Tow porosity model for the electrode micropore (Porada, Zhao et al. 2013)

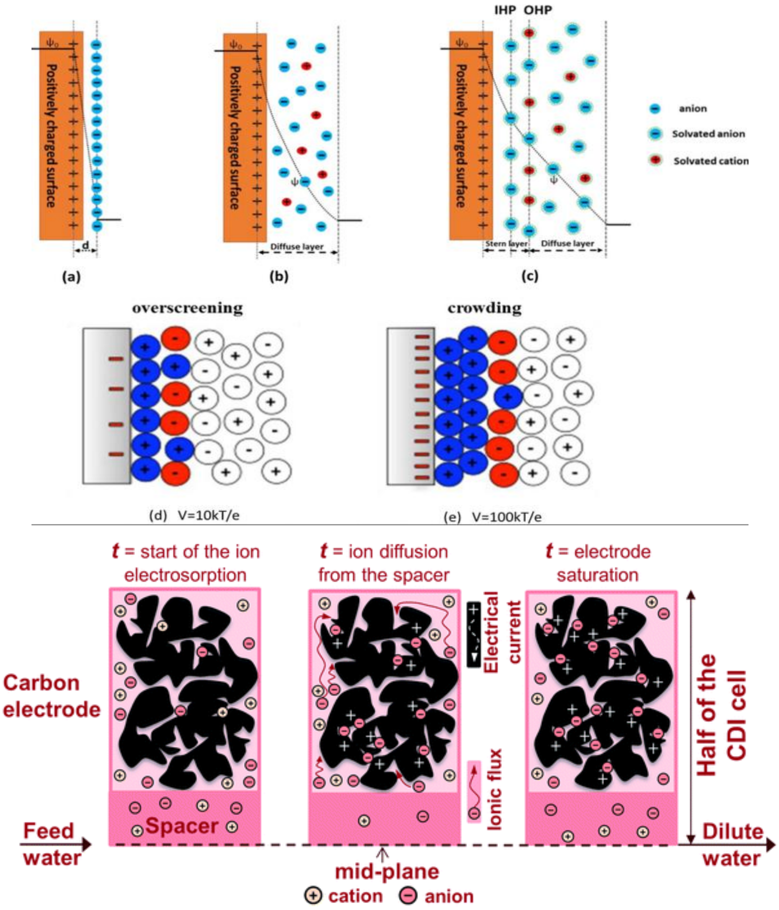

Figure 8 Review of different ionic EDL models: a)Helmholtz model, b) Gouy Chapman model c) Stern layer model d)Structure of ionic liquid layer at low voltage, e) Ionic layer structure at high voltage (Zhai, Zhang et al. 2022),(Porada, Borchardt et al. 2013) Ion transport into porous carbon electrode.

2.4.5 Mode of Operation

Various operating modes are available for CDI units based on applications. This experiment selected the constant voltage (CV) operation mode for characterisation. These two modes will be used at different points in this thesis and are essential to note.

CV- Constant voltage operation – Voltage is applied in the electrode as a driving force to separate ions from the salt solution and maintained through the adsorption cycle; water outlet concentration drops drastically in the beginning and slowly rises to the feed concentration as the electrode pores are saturated with ions. When the polarity is reversed, the salts are released back into the solution, resulting in a high concentration peak, and then normalises close to the feed solution as all the salts are expelled from the pores.

CC- Constant current mode - Constant current is applied to the electrodes, equal to the ionic current in CDI, and the voltage increases according to the cell's state of charge.

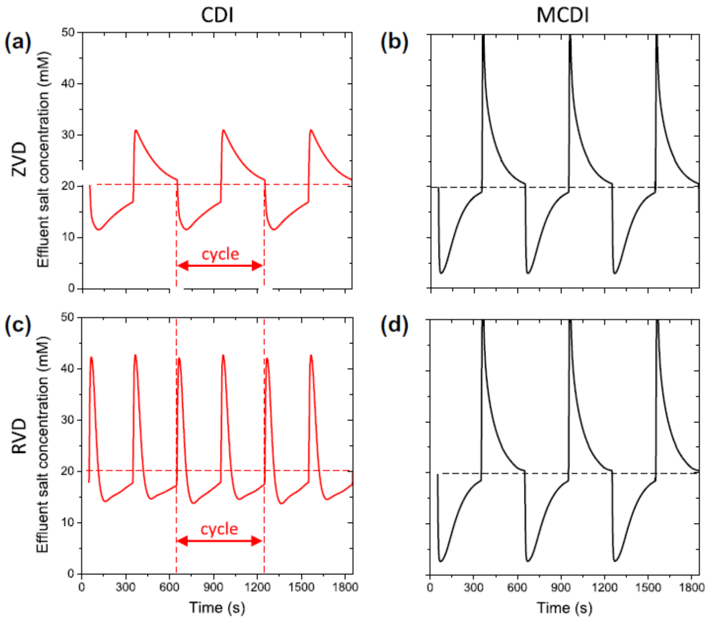

Figure 9 CDI cell operation adsorption desorption modes a) CDI ZVD, b) mCDI ZVD, c) CDI RVD, d) mCDI RVD. (Porada, Zhao et al. 2013)

The (zero volt discharge) ZVD method is considered a more energy-economical method. It can be seen from CDI ZVD and reverse voltage discharge (RVD) that two cycles are completed in RVD mode; the cycle frequency is faster in CDI. Meanwhile, in mCDI, the frequency is the same in both cases. This CDI model RVD is less efficient as opposite ions will be attracted during regeneration. RVD or ZVD is more efficient in mCDI units as per Figure 9. The research team states that RVD had a high salt adsorption rate during the trial, so the ZVD method for mCDI was time-consuming. For VS3 v_{mi} characterisation, the RVD method was utilised.

2.4.6 Energy Consumption and Cost in CDI unit

CDI is considerably more energy-efficient than RO and thermal distillation (TD), making it a promising technology for treating low-salinity water. Table 2 provides a comparison of energy consumption among various water treatment methods. Thermal distillation and reverse osmosis are commonly used techniques for desalination in the industry.

Table 2 Energy consumption comparison of water treatment methods (Anderson, Cudero et al. 2010)

Water Treatment Technique	**Energy consumption (kWh/m^3)**	**Worldwide application %**
Thermal distillation	4	51
Reverse osmosis	2.9 to 3.7	49
CDI technology	0.12 to 1.1	

As mentioned in section 2.3, the overall energy consumption in the CDI stack is characterised by

$$E_{cdi} = E_{ads} + E_{desorb} \qquad [6] \ \text{(Normal cycle)}$$

$$E_{cdi} = E_{ads} - E_{desorb} \qquad [7] \ \text{(Optimized cycle)}$$

Using the desorption cycle without applying external energy, salt ions in the electrodes are used as a capacitor during the desorb cycle.

Zero-volt discharge technique researched by (Bales, Kovalsky et al. 2019) overall energy recovery of 60% and water recovery rate of 80% as per the study below Figure 10. Over a 30,000-hour cycle with the ZVD method would result in significant energy savings.

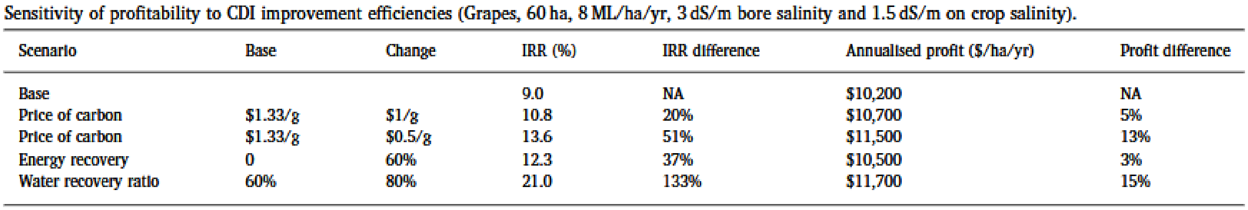

Sensitivity of profitability to CDI improvement efficiencies (Grapes, 60 ha, 8 ML/ha/yr, 3 dS/m bore salinity and 1.5 dS/m on crop salinity).

Scenario	Base	Change	IRR (%)	IRR difference	Annualised profit ($/ha/yr)	Profit difference
Base			9.0	NA	$10,200	NA
Price of carbon	$1.33/g	$1/g	10.8	20%	$10,700	5%
Price of carbon	$1.33/g	$0.5/g	13.6	51%	$11,500	13%
Energy recovery	0	60%	12.3	37%	$10,500	3%
Water recovery ratio	60%	80%	21.0	133%	$11,700	15%

Figure 10 Promising profitably to CDI improvement efficiency (Bales, Kovalsky et al. 2019)

As an improvement in energy efficiency, 35% to 40% of the energy consumed can be recovered from the charging cycle as the porous electrodes act as a capacitor as per Figure 11. Overall, 98% of energy should be recovered thermodynamically (Han, Karthikeyan et al. 2015). 0.85kWh/m^3 for brackish water treatment from 32.7 mM to 5.5 mM.

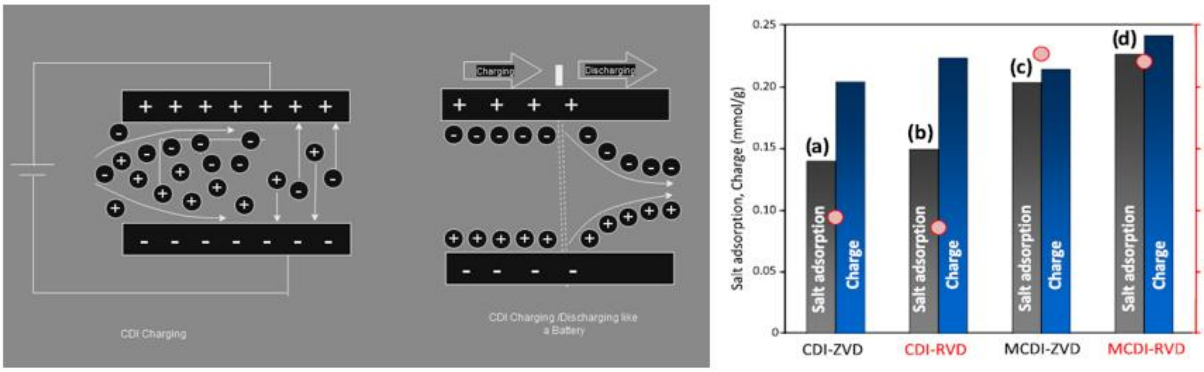

Figure 11 CDI electrodes as capacitors energy recovery mode, buck-boost converter (Chen, Yin et al. 2018)

The Figure 12 Evidence research in CDI technology provides the circuit model theory of CDI stack for Ohmic losses.

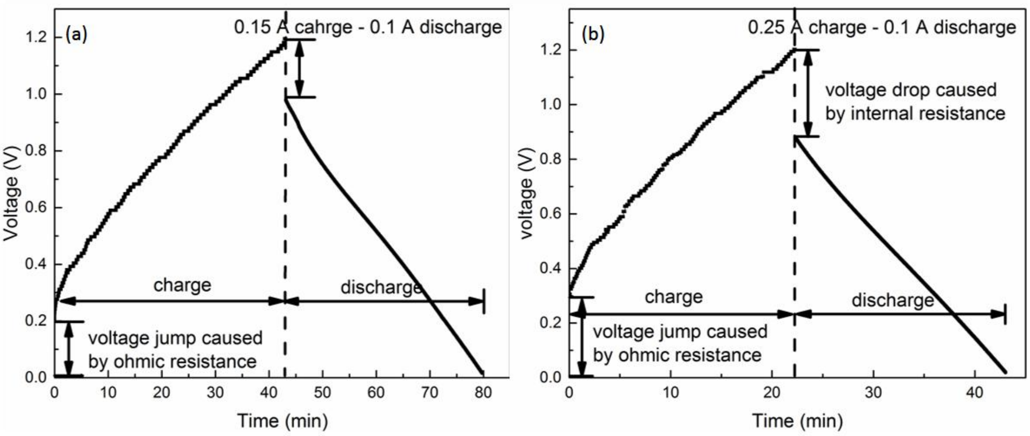

Figure 12 Voltage curve for mCDI 1200 mS solution with 0.1 A discharge with two sets of charging discharging cycles.(Chen, Yin et al. 2018)

The economically feasible operating cost of 1 AUD/kl of brackish water treatment by CDI technology by (Bales, Kovalsky et al. 2019). Energy consumption in CDI unit improved for brackish water treatment is less than 1 kWh/m^3 (Qin, Deshmukh et al. 2019), It was improved from 2006, industrial wastewater such as thermal power plant effluent treatment trailed, and 92% salt removal was achieved with 1.96 kWh/m^3 energy consumption (Lee, Park et al. 2006). The membrane implementation in CDI improved the salt removal efficiency by 19%.

Regarding energy consumption based on the mode of operation, the constant current mode consumes less energy, 26 to 30%, than the constant voltage operation.

$$\Delta G = G_{fresh} + G_{Conc} - G_{feed} \qquad G_i = RT\phi_v, iC_i LnC_i \qquad [8]$$

$$\Delta G = RT\phi_{v,fresh}\left(C_{feed} - C_{fresh}\right)\left(\frac{ln\alpha}{1-\alpha} - \frac{ln\beta}{1-\beta}\right) \qquad [9]$$

$$\alpha = C_{feed}/C_{fresh} \qquad \beta = C_{feed}/C_{fresh}$$

As per thermodynamic calculation, the minimum energy requirement for 100 mM to 5 mM brackish water with WR =0.8 is 0.12 kWh/m^3, which is far lower than the reverse osmosis units. (Porada, Zhao et al. 2013).

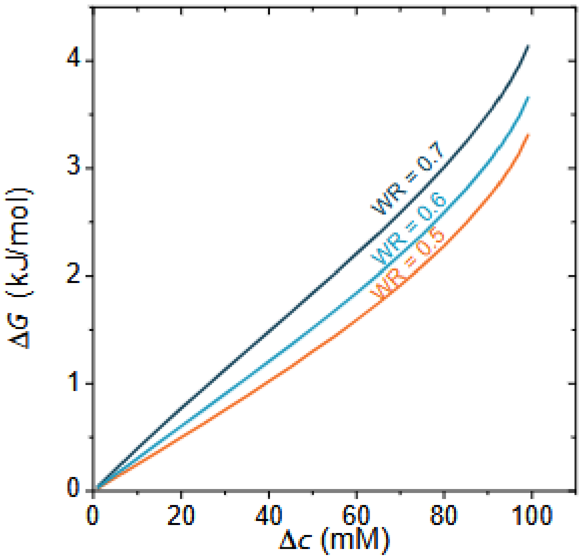

Figure 13 Thermodynamic minimum energy consumption with respect to water recovery rate (Dykstra 2018)

Although the above research Figure 13 states that CDI units consume little energy, as the efficiency drops due to scaling, energy consumption tends to increase drastically as the duration of the treating cycle increases.

2.4.7 Reasons for pH Change in CDI

When we investigate the CDI unit fouling and scaling issues, the key parameter influencing the scaling is the pH change in the CDI unit. As per theoretical calculation (Dykstra, Keesman et al.

2017), research conducted by two main mechanisms causing pH change in the mCDI spacer channel can be classified (Arulrajan, Dykstra et al. 2021)

- **Faradaic Reactions-** Redox reactions play a significant role in CDI electrodes, including water splitting and the oxidation or reduction of electrode materials (Porada et al).

- **Non-Faradaic Processes** - such as different mobility of various ions and chemical surface charge groups present in the micropores of AC electrode. The faradaic reactions in CDI occur unfavourably and result in reduced charge efficiency, unwanted pH changes, and oxidation of carbon (He, Wong et al. 2016, Dykstra 2018, Zhang, He et al. 2018). Individual ion adsorption rates (Arulrajan, Dykstra et al. 2021) as the non-faradic processes also influence pH change.

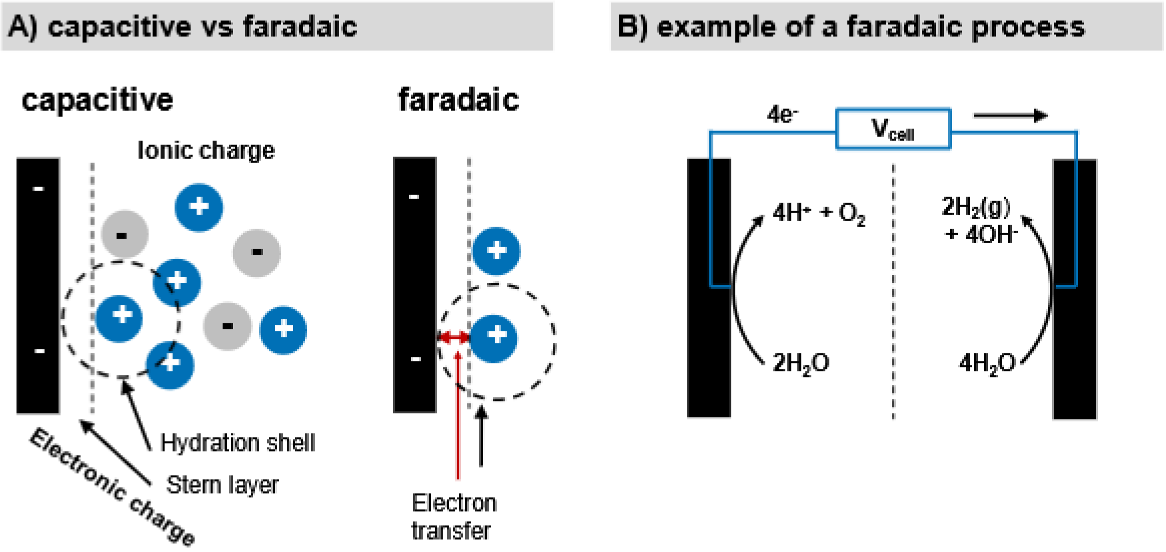

Figure 14 Capacitive vs faradaic process in CDI. Ion storage in capacitive process and electron transfer in Faradaic process.(Dykstra 2018)

Significant finding by other studies (Tang, He et al. 2017) regarding faradaic reaction and formation of hydrogen peroxide, Faradaic reactions were observed by (Tang, He et al. 2017). The variation in pH was recorded. A redox reaction in CDI and mCDI cells was experimented with. The hydrogen peroxide formation was observed only in CDI cells; no significant H_2O_2 production was observed in mCDI. This mechanism is shown in Figure 15. The illustration in Figure 14 effectively demonstrates CDI units by highlighting the crucial roles of capacitive effects and Faradaic processes, supported by a relevant example.

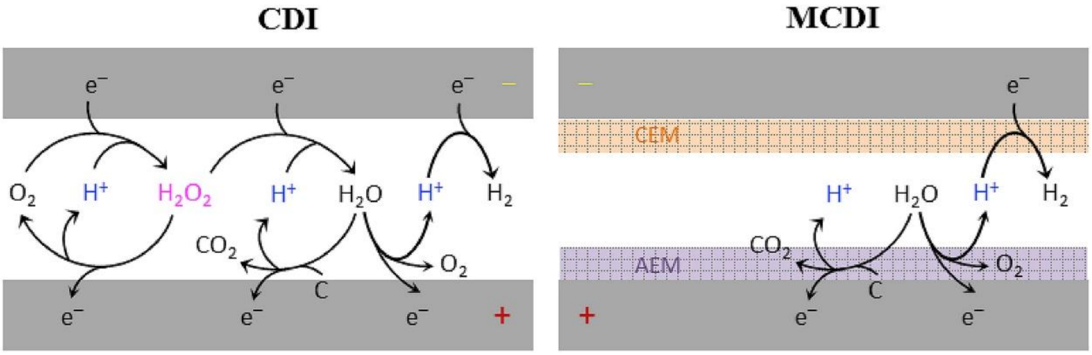

Figure 15 Faradaic reaction comparison in CDI and mCDI cells (Tang, He et al. 2017)

2.4.7.1 Faradaic Reactions in CDI

Following reactions at cathode as summarised by Tang (Tang, He et al. 2017);

$$\frac{1}{2}O_2 + e^- \xrightarrow{H^+} \frac{1}{2}H_2O_2 \qquad E^0 = 0.69 \ \ V/SHE \qquad [10]$$

$$\frac{1}{2}H_2O_2 + e^- \xrightarrow{H^+} \frac{1}{2}O_2 \qquad E^0 = 1.78 \ \ V/SHE \qquad [11]$$

$$H^+ + e^- \rightarrow \frac{1}{2}H_2 \qquad E^0 = 1.78 \ \ V/SHE \qquad [12]$$

Reactions at anode;

$$\frac{1}{2}H_2O_2 \rightarrow \frac{1}{2}O_2 + H^+ + e^- \qquad E^0 = 0.69\, V/SHE \qquad [13]$$

$$\frac{1}{2}C + H_2O \rightarrow \frac{1}{2}CO_2 + H^+ + e^- \qquad E^0 = 0.7 - 0.9\, V/SHE \qquad [14]$$

$$\frac{1}{2}\, H_2O \rightarrow \frac{1}{4}O_2 + H^+ + e^- \qquad E^0 = 1.23 \quad V/SHE \qquad [15]$$

Table 3 CDI units and pH change contributing reactions (Tang, He et al. 2017)

Cell	**pH increase contributing reaction**	**pH decrease contributing reaction**
CDI	Reaction 10-12	Reaction 13-15
mCDI	Reaction 12	Reaction 14-15
AEMCDI	Reaction 10-12	Reaction 14-15
CEMCDI	Reaction 12	Reaction 14-15

Table 3 outlines the driving reactions occurring in all CDI-related units. Our focus is on the CDI and mCDI units, precisely the driving reaction responsible for hydrogen peroxide formation in the electrodes. This reaction affects the pH levels in both the CDI and mCDI units. The variations in pH across different CDI units are plotted in Figure 16 with the charging and discharging cycle (Tang, He et al. 2017).

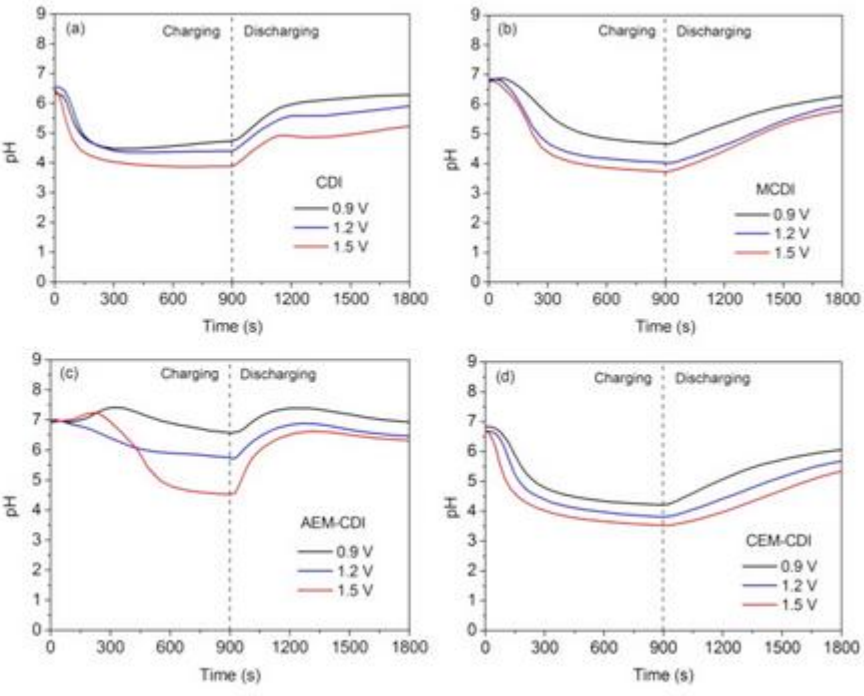

Figure 16 pH variation in CDI, mCDI, AEM CDI, CEMCDI (Tang, He et al. 2017)

All faradaic and non-faradaic reactions in CDI electrodes are illustrated Figure 17 by (Zhang, He et al. 2018) are the main reasons for the energy loss by faradaic reactions.

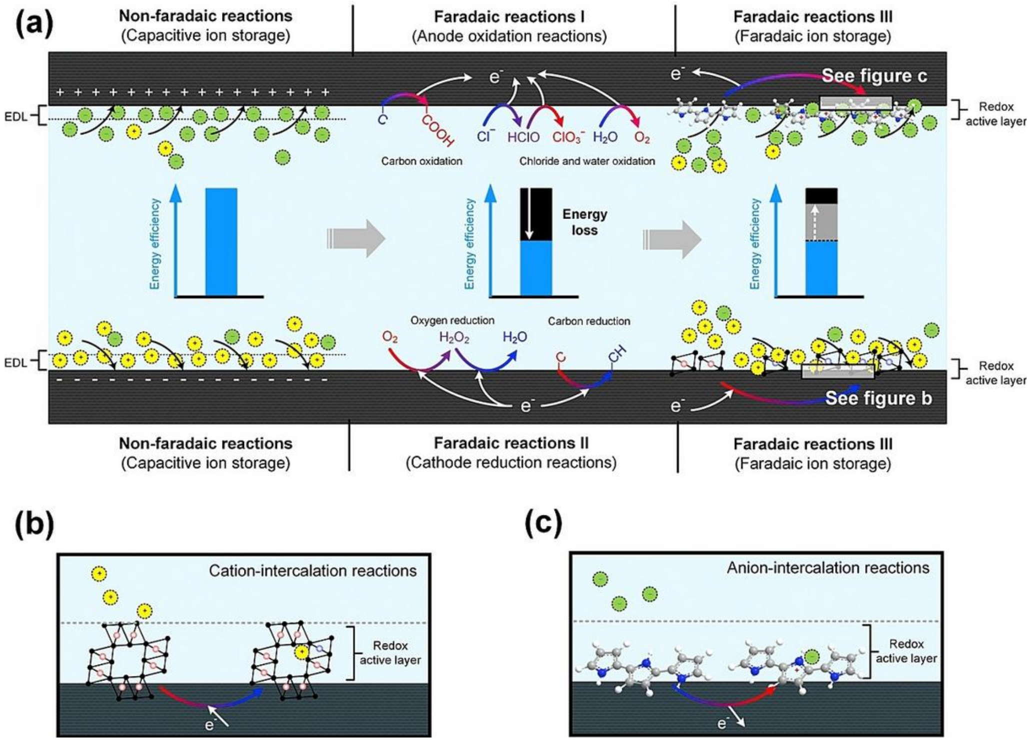

Figure 17 Overall Reaction in CDI cell (Zhang, He et al. 2018)

In the study by Lee et al., experiments (Figure 18) demonstrated that the stack voltage increased to 1.6 V, indicating alkaline conditions, even when the feed was varied from acidic to basic. The underlying cause of this phenomenon remains unclear. In CDI, the Faradaic reaction is negligible at lower operating voltage ranges. However, as the applied voltage exceeds the standard hydrogen electrode (SHE) or reaches a certain threshold, water undergoes electrolysis, splitting into hydrogen and oxygen molecules through the faradaic reaction, Lee et al. reported an experiment that observed pH changes in a CDI system at higher DC voltages.

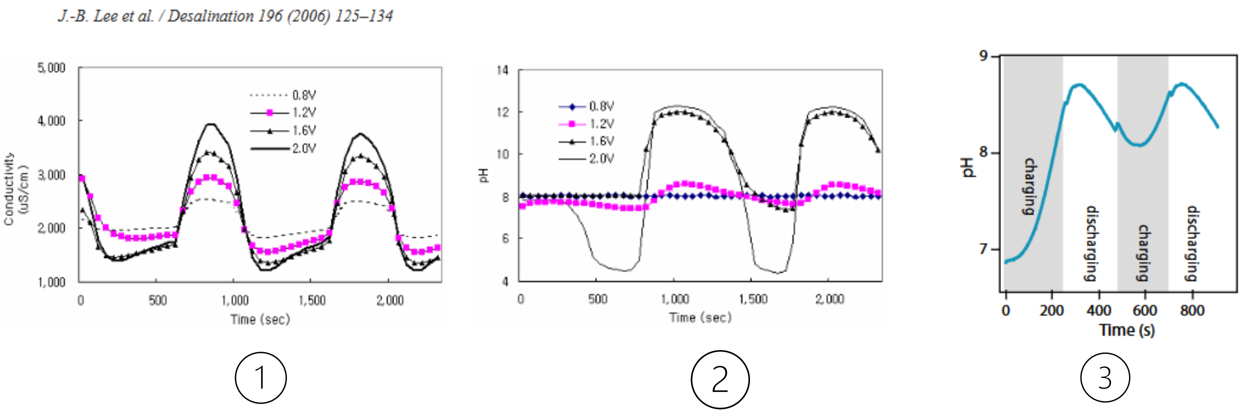

Figure 18 Conductivity and pH change at different DC voltage applied to the system. Image 1. Conductivity vs Time. 2. pH vs Time 3. pH vs Time (charging-discharging cycle) (Lee, Park et al. 2006, Dykstra 2018)

In 2021 (Nur, Nazriati et al. 2021), research revealed a pH variation of 2 to 12. The higher pH at the cathode and lower pH at the anode chamber affect electrosynthesis (Figure 19).

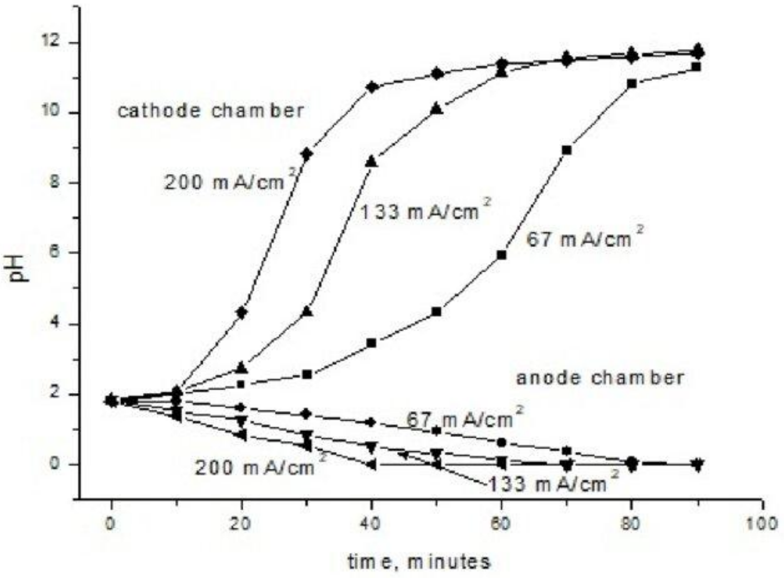

Figure 19 pH variation in anode cathode chamber in electrosynthesis research by (Nur, Nazriati et al. 2021)

2.4.8 pH-Related Mechanisms Affecting Performance of CDI Units

One of the key factors influencing the efficiency of CDI cells is fouling. According to a study by Chen et al. (Hassanvand, Chen et al. 2019), fouling resulted in a 70% loss in adsorption efficiency and a 90% loss in charge efficiency. The research also highlighted that external cleaning methods can further damage the carbon electrode, primarily due to the erosion of the binder or carbon when strong alkalis are used to remove the scale. Additionally, dissolved organic matter, such as humic acid, appears to contribute to fouling by blocking electrode pores and impairing salt adsorption capacity. Furthermore, the presence of ferric ions has been shown to exacerbate the fouling of electrodes in CDI units (Mossad and Zou 2013).

One of the mechanisms of blocking the spacer channel is similar to the fouling phenomena in membranes. Fouling acts to block the open hydraulic pathways, typically approaching the micron and sub-micron size range. The permeability K of a porous material can be given by the Carmen Kozeny equation.

$$K = \frac{d_p^2}{180} \frac{\varepsilon^3}{(1-\varepsilon)^2} \qquad [16]$$

Where d_p is the diameter of the fouling particle in a bed of packed particles and ε is the porosity. As fouling accumulates, d_p effectively decreases, as shown below on the image outline of a spacer channel (Noor 2023)

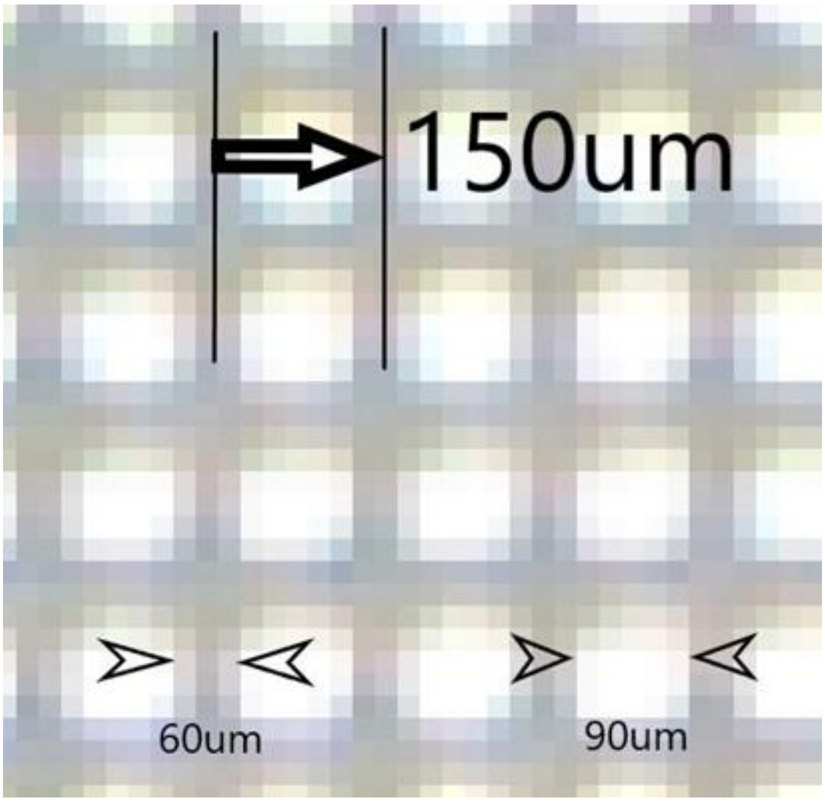

Figure 20 Diagram showing the full repeating dimension of the square in a spacer mesh made up of the solid substrate and pore space. As the substrate grows due to scale formation or fouling, the pore dimension reduces.

As fouling accumulates, the effective particle diameter was $d_p=d_{p0}+dz$ where dz is the fouling matter forming on the mesh substrate as a solid. The initial substrate size in this study was d_{p0} (size of 60µm).

The porosity was modelled as $\varepsilon = 1-(60+dz)/150$ and substituted into the permeability equation. From this, three possibilities were presented.

1) Fouling in CDI is a time-based process such that the accumulation of solids occurs over time such that $dz/dt>0$,
2) Fouling is based on the amount of liquid passed through the CDI, in other words, volume-based,
3) Or a combination of both.

The study of (Talebi, Chen et al. 2019) showed that an increase in hydraulic resistance, and hence a decrease in permeability, was a time-based phenomenon when investigating the scale formation in water containing whey protein with high levels of Ca^{2+} present. Here, the feed pressure increased over several weeks. The recovery of the cell responded to acid cleaning, indicating the importance of pH during the cleaning process. This is further motivation to understand the mechanisms that are driving pH in the CDI spacer channel.

It can be noted that the concept of blocking due to scale formation and blocking due to fouling are different mechanisms. The formation of scale due to the formation of minerals that are no longer soluble is highly varied depending on the composition of the feed water. The Langlier Saturation Index in water chemistry is a model to describe the potential for the formation of scale containing calcium and magnesium carbonates. The *LSI* is given as

$$LSI = pH - pHs \qquad [17]$$

and pHs is calculated as.

$$pHs = (pK'2 - pK's) + pCa + pAlk \qquad [18]$$

where *Ks'* and *K'2* are constants and *pCa* and *pAlk* relate to the amount of calcium and alkalinity present. When $LSI > 0$, it is expected that calcium carbonate will form and participate as a scale. When calculated, the regions of interest for CDI operation are where the pH is between 8 and 9.5. This is where we expect scale to form and form the basis for the region of interest in this study. It is also noted that not only is it uncertain what pH condition is reached inside the CDI cell as it has never been characterised or measured before, but also many feed waters that are treated by CDI are in this range of 8 to 9.5. Hence, in later chapters, we will investigate the CDI effect close to this range of pH values as the technique is developed to measure the pH in situ.

2.4.9 Alternative Methods for Measuring pH In-Situ

The characterisation of pH in situ to CDI has yet to be reported in the open literature. It is a difficult task due to the dimensions of the spacer channel, anywhere from 100 to 500 microns. Simultaneously, it is an environment incompatible with conventional glass electrode apparatus.

In an experimental study associated with (Kovalsky 2016) an attempt was made with a PreSens implantable pH microsensor. The measurement principle is based on a patented (dual lifetime referenced) DLR method, as also indicated in the Figure 21.

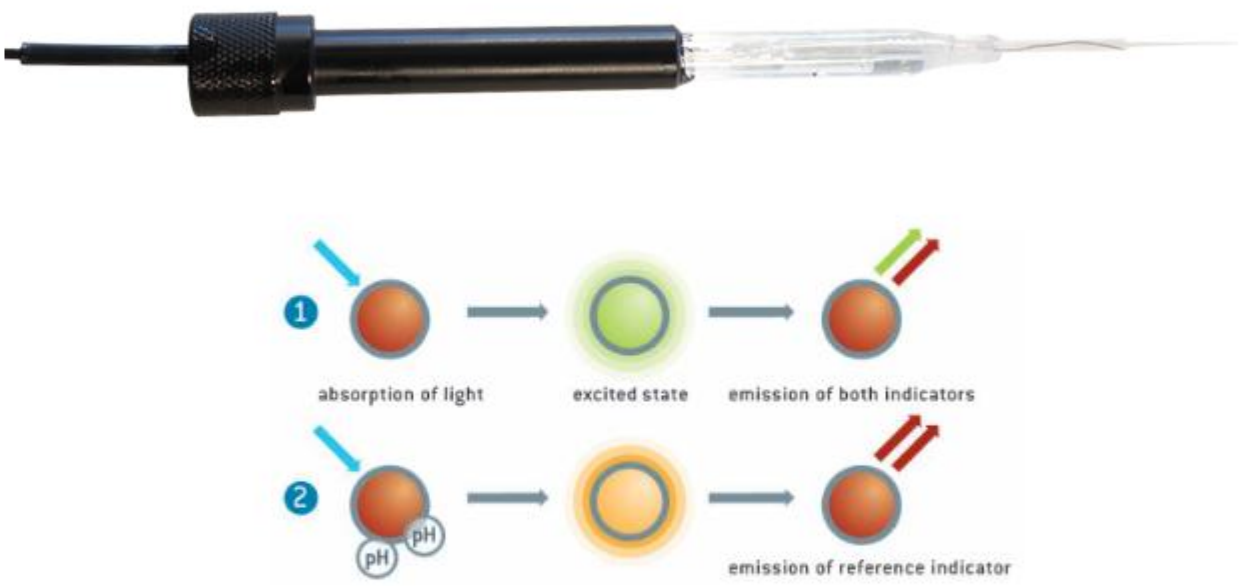

Figure 21 PreSens implantable pH microsensor

Attempts were made to position the probe in the spacer channel as shown in Figure 22. Initial calibration showed that there was significant interference when the cell voltage was applied. Limitations to this sensor include a narrow pH range from 5.5 to 8.5 and cross-sensitivity to salinity. Thus, this technique proved to be not viable. This, and the delicate nature of the expensive probe (>$50,000 USD), meant that alternative techniques need to be developed. This brings us to the current state of pH characterisation in situ to CDI.

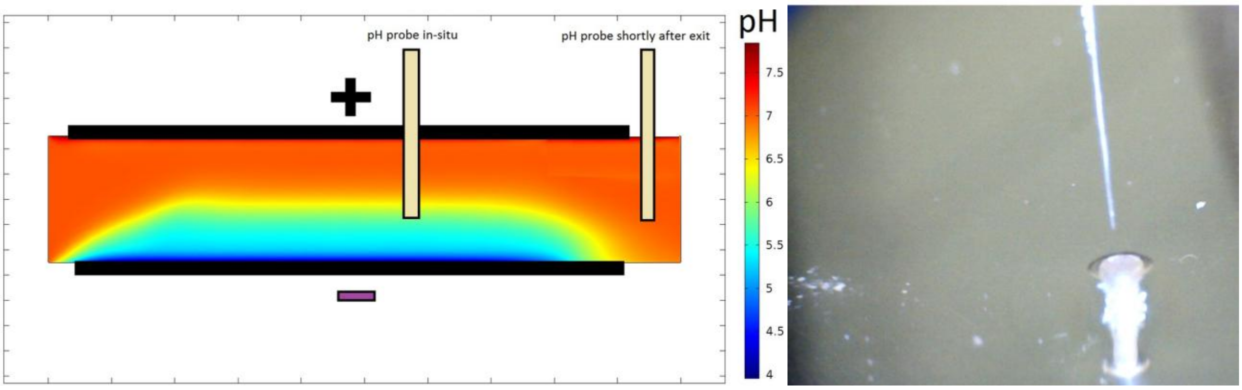

Figure 22 Image showing the 30um demo tip of the pH probe compared to a 500um hole created to access the carbon layer

2.5 Summary

This literature review covers the various characteristic aspects of CDI technology. It has been established there is a gap in knowledge in several key areas that has limited the speed of uptake of the technology that will be needed in key applications in the future. Heavy impact on freshwater supply is foreseen due to the emission and global warming by seawater intrusion and groundwater contamination. The CDI technology shows promising lead in providing clean water to all economic level people, energy saving option in water treatment. mCDI offers a notable advantage in terms of reducing environmental emissions. Understanding the characteristics of CDI will further improve the optimisation of this technology.

The longevity of a CDI cell depends largely on the efficiency of its electrodes. From the literature review, it is evident that the main factor affecting CDI performance is fouling and scale formation. Perhaps new, improved electrode designs with modified membrane arrangement techniques and energy-efficient process control methods would improve the mCDI unit in supporting uninterrupted global clean water accessibility. Before this can happen, it is necessary to develop techniques to directly observe one of the main properties of the underlying CDI process, and that is the pH in situ.

Visualising the real time pH variation in a CDI cell was a challenge faced by researchers in the past. A potential technique capable of measuring pH in an implantable form was one of the ideas explored. However, due to technical limitations, it has been established that there is an opportunity to develop a novel method that is customised to the CDI mechanism and works within its unique constraints.

3 Chapter – Electrosorptive Characterisation of VS3

The purpose of this chapter is to examine the operation of a commercially produced mCDI module that has been in periodic operation for 5 years. mCDI modules of this age and much younger reduce desalination efficiency due to scale formation. This is the formation of mineral precipitates in the spacer channel. Here, we look at the operating characteristics and establish the reasons to take a closer look at the conditions in situ to the electrode.

3.1 Background

CDI technique has the following advantages over other technologies: It is energy efficient and sustainable, and it has the potential to be an easy way of manufacturing electrodes, easy to manufacture. The key parameters controlling electrode nature properties, such as micropore volume and characterisation, are vital in understanding and improving the technology.

The purpose of studying the VS3 was to establish a fundamental understanding of CDI's underlying physical, electrical, and chemical processes using readily accessible laboratory techniques and a commercial electrode stack of moderate size, the Voltea VS3. These tests included;

- Electrokinetic characterisation of the CDI stack,
- Determine Ohmic Losses using the circuit modelling theory.
- Characterising the micropore volume v_{mi},

Tests in later chapters will involve smaller cells and microfluidic-sized configurations. However, this chapter will establish the foundation and the necessity of focusing on unexplored aspects of the CDI mechanism.

3.1.1 EDL Model in Porous Activated Carbon Sheet

CDI stack was operated in multiple adsorption and desorption cycles. After the adsorption cycles, ions stored in porous electrodes must be released via the ZVD or RVD cycle (Figure 9). The adsorption cycle was conducted with a voltage of up to 1.4V. Theoretical equilibrium calculations are done with an mD-model, and the data fits with experimental and theoretical values. This overlapping diffuse layer model considers stern layer (C_{st}) and μ_{att} term, ion concentration inside the micropores and macropore (Figure 7) concentration; at equilibrium, the macropore concentration equals the solution outside the electrode.

Ionic charge density (σ_{mi}) relation to J (Current density) as per Section 2.4.4. To characterise the v_{mi} study, the dynamic model for batch mode constant voltage model and three different salt concentrations at two different applied electrical potentials are selected. The mD-model model is fit with experimental values to equilibrium data, v_{mi} and k values are calculated.

Salt concentrations vs time study model results as below with different time intervals for 5mM,10mM, 20mM for the constant voltage batch mode operation.

The simplified dynamic model of CDI is founded on a modified Donnan model, which is deemed the most appropriate framework for the electric double layer (EDL) representation. Figure 23 illustrates the essential operational stages within the VS-3 CDI unit and provides an analysis of the characteristics associated with the CDI operational model.

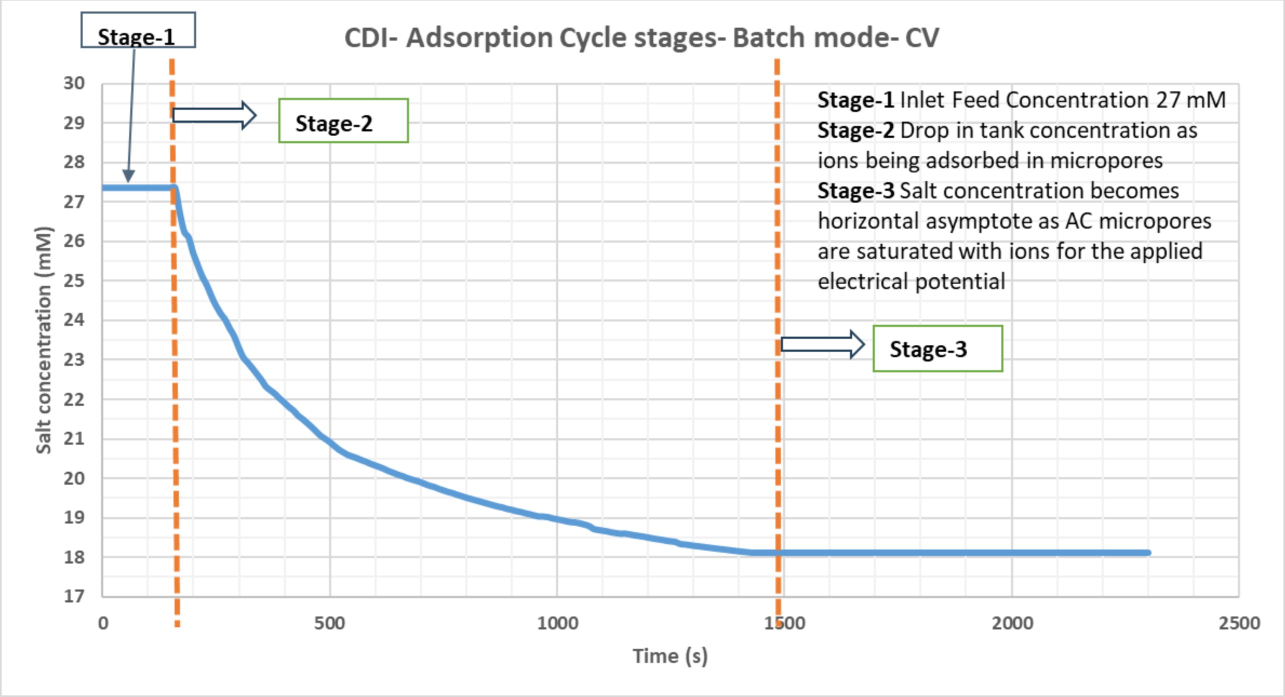

Figure 23 CDI batch mode adsorption cycle- constant voltage operation

CDI batch mode ion adsorption model illustrated in Figure 23 explains the salt concentration vs time. There are 3 stages in salt adsorption:

Stage-1 Initial tank concentration is 27 mM; as the voltage is applied (0.8V), salt ions are pulled out from the spacer section into micropores (Figure 8) of activated carbon. The tank salt concentration starts to drop at the beginning of stage 2; the rate of adsorption is faster at the beginning of the stage and slows down as the micropores are saturated with salt ions. Stage 3 is the completion of the adsorption cycle where AC can not take any more ions from the solution as the electrode micropore is saturated with ions for the applied electrical potential. The tank concentration becomes a horizontal asymptote (salt concentration 18mM).

v_{mi} - Micropore volume is the internal volume of intraparticle nanostructure (size <2nm) inside the porous activated carbon (Porada et al). High v_{mi} means large volume for charge storage, resulting in higher capacitance and better performance of ion storage in the micropores of activated carbon. The salt adsorption capacity is directly related to the micropore volume of activated carbon. The variable parameters, constants, operating parameters used in micropore volume calculations are tabulated in Table 4, Table 5, Table 6.

Table 4 Parameters for v_{mi} modelling, variable

Parameters - Model fitting		
k	Effective transport co-efficient	m/s
v_{mi}	Micropore volume	m^3
μ_{att}	Chemical attraction energy term for ions to travel into intra-particle of pore	kT
Variables from calculations		
$C_{St,vol}$	Volumetric stern layer capacity	F/m^3
$\Delta\phi_{St}$	Stern layer potential difference	F/m^3
V_T	Thermal voltage	25.7mV
$C_{cation,mi}$	Cation micropore concentration	mM
$C_{anion,mi}$	Anion micropore concentration	mM
$C_{salt,mA}$	Macropore salt concentration	mM
$c_{ions,mi}$	Micropore ion concentration	F/m^3
σ_{mi}	Ionic charge density in micropore	mM
$\Delta\phi_d$	Donnan electrostatic potential difference, Voltage difference between micropore and macropore (inside and outside carbon particle)	-
T_1	Main electrical driving force for ion separation from solution	-
T_2	Major opposing force term, ionic charge density in micropore	-
T_3	Minor opposing force term, based on Concentration	-
$c_{ions,mi}$	Micropore ion concentration	mM

Table 5 Parameters for v_{mi} modelling, constants

Constants in model calculations		
μ_{att}	Chemical attraction energy term for ions to travel into intra particles of pore	kT
F	Faraday's number	96,485 C/mol
α	Parameter to describe the non-linear part of the stern capacity. (Charge dependence of stern capacitance)	Fm^3
β	Beta	-
γ	Gamma	-
b	Calculation term for Cions	-

Table 6 Parameters for v_{mi} modelling, operating parameters

Operating Parameters		
c	Salt concentration	mM
V_{cell}	Cell voltage	V
$\Delta\phi_{tr}$	Voltage drop for ion transport (between electrodes)	-
J	Flux current density	mol/m^2/s
A	The cross-sectional area of the electrode	m^2
V_t	Total volume	m^3
t	Time in seconds	s

3.2 Materials and Equipment

3.2.1 Reagents

The electrosorption characteristics were analysed in this experiment using a monovalent salt, specifically a sodium chloride solution. The following reagents were utilised in the study;

- Citric acid monohydrate,
- Demineralised water,
- Lab-grade NaCl.

Citric acid was utilised as the low pH reagent for acid washing to facilitate scale removal. A 1250 ppm NaCl solution was prepared in the CDI supply reservoir, while demineralised water was used for both flushing and the preparation of the salt solution.

3.2.2 Equipment

Voltea is a renowned market leader in CDI technology, in water treatment with a wide range of applications, such as residential, horticulture, cooling towers, and the wine industry. The Voltea VS-3 module with the technical specification mentioned Table 7 was chosen for this experiment. One of its ease-of-handling features is that it can be fixed easily on a benchtop and assembled for simple experiments.

Table 7 VS-3 mCDI unit technical specification

Module model	**VS-3 (AC with AEX&CEX membrane unit- mCDI)**
Dimension	26.6 cm x 22.5cm x8cm (LxWxH)
Weight	5Kg
Feed in coupling	Size 10 push-in connection female (3/8")
Product outlet coupling	Size 10 push-in connection male (3/8")
Electrode connection	M5 Copper rod with M5 bolts.
Instant Flow Rate	0.2 - 4.1 LPM (Based on 320ppm TDS at 50% removal)
Net Produced Flow	0.2-4.1 LPM (Based on 320ppm TDS at 50% removal)
Recommended power	0-120 A/ 0-2V
Max Pressure	2 bar
Water Temp	5 - 30ºC
Mfc power consumption rating	< 0.5kWh/m^3

The micro diaphragm pump (Propumps) of 60W (max power), a pressure rating of 0.8MPa (8 bar), and is designed to operate with a rated DC power supply of 12V. For this setup, the pump was operated at 8V DC with a maximum current of 5A to meet the required pressure and flow rate as recommended for the experiment. The measurement devices include a Vernier Go Pro Voltage Meter and a Vernier Go Pro Conductivity Sensor with a platinum cell, ensuring accurate monitoring and measurement of system performance.

3.3 Methodology

This section outlines the detailed methodology employed for setting up and operating the VS-3 CDI module, including system prechecks and cleaning procedures prior to characteristic experiments to ensure reliable data collection. The VS-3 CDI stack is mounted on a benchtop skid for experiment data collection. The system consists of a CDI stack module and pumping unit, a Water circulation pump reservoir, a Program controller unit consisting of an H-bridge, and an Arduino program controller board.

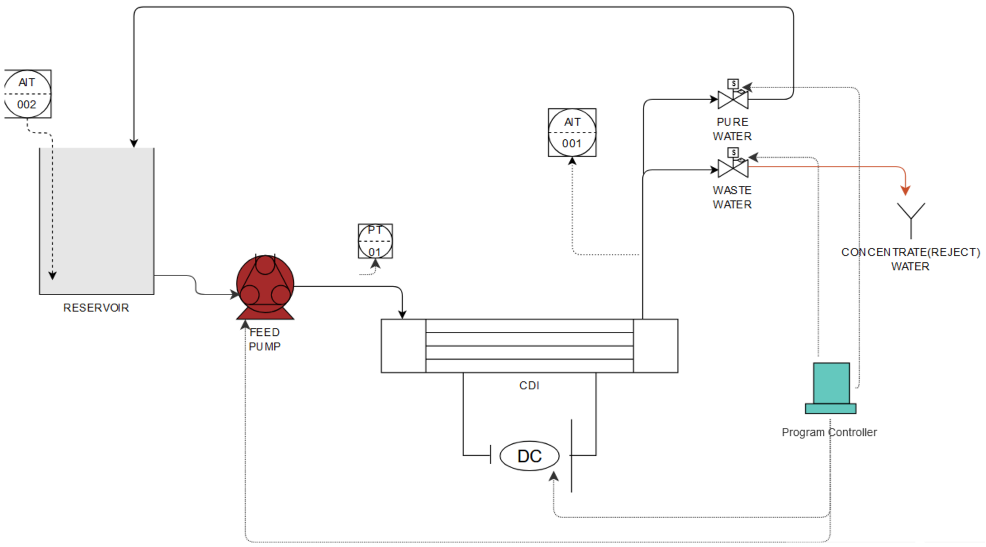

Figure 24 CDI system VS-3 batch mode

3.3.1 Prerequisites

The system check prior to start-up was done in 2 sections: mechanical integrity and electrical circuit checks. The mechanical integrity was confirmed by the hose connections, and the fittings are in secure condition. Checked for all electrical leads to be properly connected to avoid voltage loss, current leakage, and shorting. The conductivity sensor was secured in the pressure-tight encapsulated device. The system is powered up to check whether the outlet solenoid (reject and product) operates alternatively. Any one outlet must always be open. The manual switching of the H-bridge relay function was checked by activating the toggle switch and observing the relay pattern switching in the power supply unit.

3.3.2 CDI Clean in Place

A clean-in-place procedure was necessary after extended periods of operation to remove the scale caused by water hardness and to eliminate biofilm. The cleaning process was conducted in two stages: first, a citric acid wash was performed, followed by an air scour method. The CDI stack was pre-flushed using demineralised water under electrode shunt conditions.

3.3.2.1 Stage 1: Acid wash

Pre-flushing of the CDI stack was done with demineralised water. Then, 5 g of citric acid was dissolved in 3L of demineralised water. The CDI electrode stack was kept in shunt condition. CDI inlet was fed from the tank containing citric acid solution, and the reject and product outlet houses were placed back into the reservoir for continuous circulation. After acid washing, the system is flushed with demineralised water until the citric acid is completely eliminated from the system; this can be ensured until the conductivity of DM water is reached. The pH of the cleaning solution during washing was 3; after flushing, it was found to be equal to the DM water pH reached.

3.3.2.2 Stage 2: Air scouring

The air scouring step is followed to clear any biofilm or particulate iron fouling present in the electrode surface, which could affect the system's performance. This method (Pulse jet water-air cleaning system) is used to clean the electrode mechanically by applying physical force on the electrode surface to remove fouling. The air scour skid blows compressed air and water through the CDI stack inlet, dislodges the fouling material, and scours away through the outlet. The performance of the CDI can be checked after the first stage trial tests to determine if further cleaning is required.

The 2-stage cleaning process effectively removed the scales and biofilm from the CDI system. Approximately 4 litres of water circulated through the system; no floating components, debris, carbon material, or scale material were observed in the outlet collected water.

3.3.3 Experiment

An experiment in batch operating mode was set up with the 5L container as a reservoir, a vernier Go Pro conductivity sensor, VS-3 module CDI stack, power supply unit 0-40A, 1-15VDC Powertech MP3094) switching mode power supply unit.

The process flow diagram shown in Figure 24 CDI system VS-3 batch mode consists of a 12V Micro diaphragm pump (Propump), PVC tubing, and power supply skid containing Arduino Mega controller, H-bridge relay setup, with a manual toggle switch to change between adsorb and desorb mode.

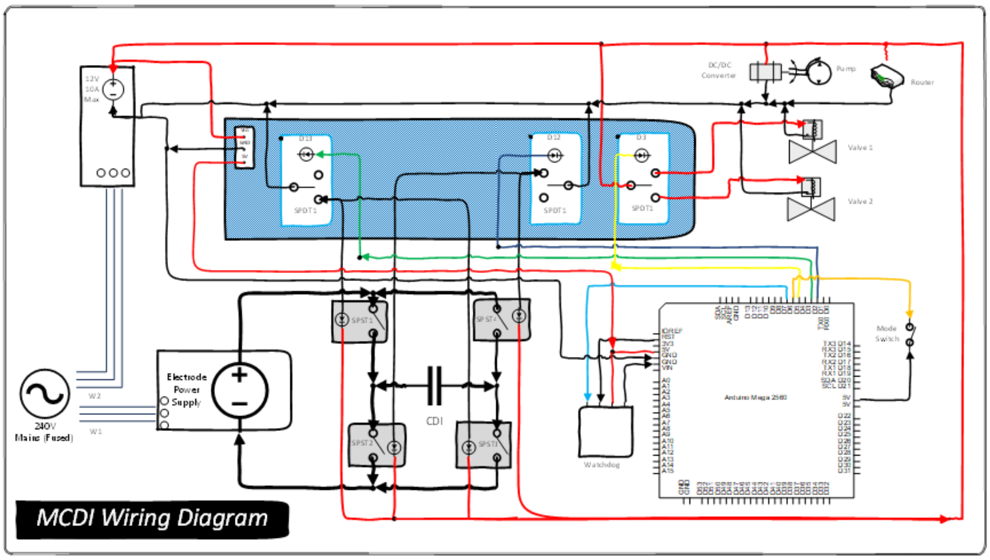

Figure 25 mCDI wiring diagram H-bridge setup

Figure 25 represents the control loop system for manual toggling of electrode polarity reversal for the adsorption and desorption process. One of the essential functions is to keep the CDI water outlet solenoid valves energised with respect to the adsorption/desorption cycles. The control system was configured in such way that always one valve (the best choice was reject solenoid to enable the flushing of the system) is open continuously. The H bridge employs 2 sets of controls;

1. 60A SPST (Single pole single through) switch for electrode power supply,
2. 10A SPDT (Single pole double through) switch relay for water outlet solenoid.

There are 4 SPST switches in the H-bridge for the CDI electrode power supply. During one (Adsorption) cycle, SPST1 and SPST3 are energised, making a forward flow circuit. When the toggle switch is activated, the next (Desorption) cycle, SPST2 and SPST4, are activated for the reverse flow of the circuit. The toggle switch is configured in the program along with the water outlet solenoid through the SPDT relay (D3). During the adsorption cycle, it is energised to the tank reservoir; after switching to desorption mode, the solenoid valve at the reject line is activated, and salty water is sent to the reject.

With the CDI electrode leads in ZVD shunt condition, the new experiment 3L batch solution with NaCl is prepared. System dead volume was calculated by calculating the concentration change in the system by adding a known salt concentration to the system, which was calculated as 570 ml. The salt concentration in the whole system is kept uniform prior to the v_{mi} characterisation test; the shunt condition of the electrode makes them zero charges and zero absorbance of salts in the micropores. Few normal adsorb desorb cycles were allowed to stabilise the system stability, and the repeated pattern was verified prior to the experiment. 28.5mM (1664) ppm salt solution prepared and circulated 3L batch.

3.3.4 Method Set – Micropore Volume v_{mi}

This section elaborates on the methodology used in fitting dynamic CDI to the EDL model. This model aims to align the experimental data with theoretical model values (Conductivity vs Time) as closely as possible by adjusting the v_{mi} and k values.

First, the constant values are listed in Table 5. Parameters for v_{mi} modelling

The basic governing equation σ_{mi} (charge density) as a function of current density from equation [1].

$$v_{mi} \times \frac{d\sigma_{mi}}{dt} = J \times A$$

The secondary relations to salt concentration and J (current density) from equations [2], [3], and [4].

Dynamic stern layer capacity calculation was issued to fit the data; stern layer volume increases with time as the charge increases in the adsorption cycle.

- Conductivity measurement:

Conductivity measurements were taken at both the CDI stack outlet and the tank. An immediate drop in conductivity was observed as the clean, porous electrode adsorbed salt from the feed solution. As the system approached saturation, the outlet conductivity began to increase. Additionally, a gradual decrease in tank conductivity was noted. A small recycling batch was preferred for the v_{mi} model, and a 3-litre batch was selected. The salinity difference between the initial and final measurements was compared to determine the amount of salt ions removed by the CDI.

- Data Collection:

Three different sets of voltages were applied, revealing that salt concentration decreases as the applied voltage increases. The raw data for salt adsorption cycles was obtained using Vernier software and subsequently exported to MATLAB, where curve fitting was performed, yielding an R^2 value of 0.99.

The initial set of readings was taken at 1.2 V. The first few cycles involved a 2-minute adsorption and desorption cycle, which were implemented to stabilise the system. The main testing commenced after observing a consistent pattern in the adsorption/desorption cycles. Key parameters such as time (t), concentration (c), micropore charge density, flux (J), volumes, and flow rates were inputted into the model. Forward Euler's method was employed for subsequent iterations starting from time = 0, continuing until the final time point.

Experimental data was incorporated into the model, and all three voltage readings were recorded for the lowest v_{mi} and k values. This model aims to minimise the sum error by optimising the v_{mi} and k values for all three sets of voltage readings.

3.4 Results

3.4.1 Conductivity vs Time Raw Data

The VS-3 unit tested with batch mode at three different sets, the salt conductivity vs time data as per Figure 26 explains the relationship between the electrical potential (Table 1) as a driving force and salt removal rate in the tank for different voltages applied as a driving force.

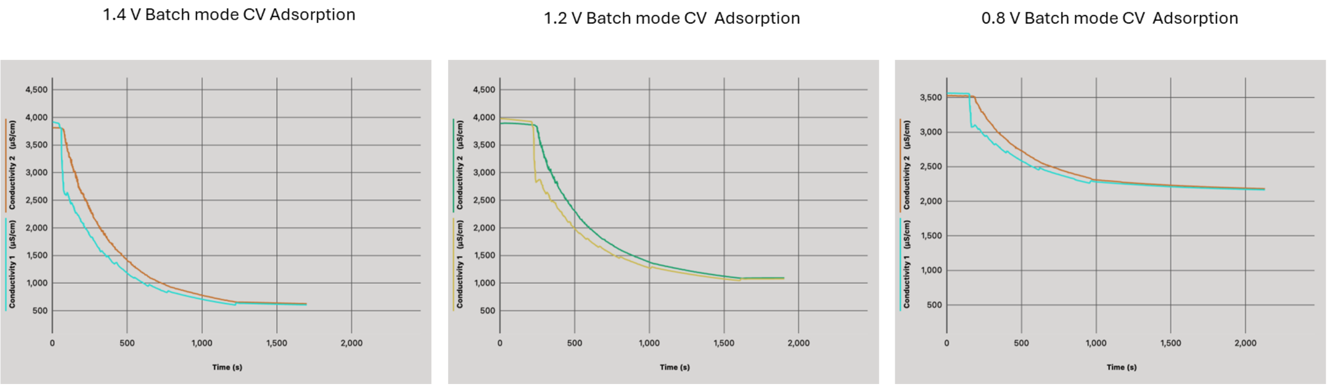
1.4 V Batch mode CV Adsorption

1.2 V Batch mode CV Adsorption

0.8 V Batch mode CV Adsorption

Figure 26 Raw data of VS-3 batch mode adsorption cycle Salt concentration in conductivity(µS/cm) vs time(s) at Voltages 1.4V, 1.2V, 0.8V

The raw data mentioned in Figure 26 shows a gradual decrease in conductivity (Concentration of salt) and reaches the equilibrium value. As the applied voltage increases, the capacity of ion removal is increased. T_1 is the major driving force (V_{cell}/V_t), which is the reason for the fast kinetics, as the opposing forces T_2 and T_3 rise as time increases and the electrode saturates with ions. At equilibrium conditions, J is close to zero. $T_1 = T_2 + T_3$ The major driving force is overcome by resistive forces, ionic charge density and Concentration gradient terms.

3.4.2 Model Analysis – Micropore Volume v_{mi}

This section provides a comprehensive analysis of the model according to (Porada, Zhao et al. 2013). The simulated model results are presented in graphical and Excel tabular format to represent the relationship and to fit the model with theoretical and experimental values. Global Parameters and constants are entered as per Table 4 and 5. The theoretical calculations are done using the inlet concentration of salt. Key calculated parameters in the table are $C_{st,vol}$ (Stern layer volume), σ_{mi}, and the current flux J. As the concentration of salt reduced as the electrode pores adsorbed the ions, the concentration of water at the spacer channel decreased. The $C(mM)$ model column represents this dynamic behaviour.

The graph NaCl (mM) vs Time(s) shows the model-predicted values plotted in blue. The yellow line represents the actual experiment values. Three different voltages were chosen to obtain the experimental data, and the model fitting was done to make the v_{mi} value inaccurate.

3.4.3 Micropore Volume v_{mi} Results

The best fit found at 67.5 ml micropore volume and effective total transport co-efficient k value of 0.3 µm/s, chemical attraction energy $\mu_{att} = 1\ kT$.

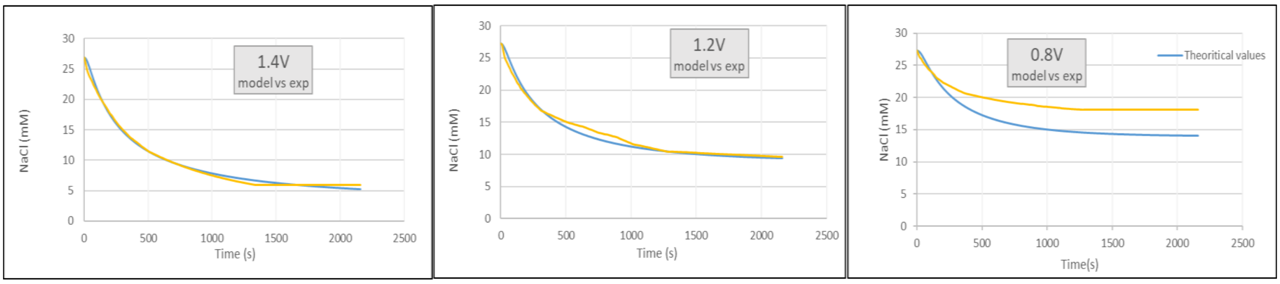

Figure 27 Experiment at 1.4V, 1.2V, and 0.8V and salt concentration vs time data plotted in the dynamic model.

The v_{mi} values were calculated based on (Porada, Borchardt et al. 2013) for batch mode constant voltage operation. The initial salt concentration data was input into the model. The theoretically calculated values were then plotted on a graph (represented by the blue line). Subsequently, the experimental data was entered into the c(mM) exp data column. The error between the theoretical and experimental values was calculated for each time step, and the total sum of errors was taken as the deviation from the theoretical calculations to the actual results. This deviation is reduced by adjusting v_{mi} and k values. A higher k value represents faster kinetics, and a higher v_{mi} value represents the larger capacity of the AC. For all three sets of voltage and concentration of salts, the sum error was adjusted to an optimum kinetics k and v_{mi} value where all the sum error comes close to the minimum. It was observed that at voltage 1.4V and 1.2V data set, the sum error was brought to a minimum of 75 and 89, respectively. In the lower voltage test at 0.8V, the data set did not fit, and the sum error was 686, a significant deviation from the theoretical value. The standard experiment by (Porada, Borchardt et al. 2013) showed the v_{mi} value of 0.22mg/L (by nitrogen sorption) here in this experiment, the value found was 0.27mg/L

3.4.4 VS3 mCDI unit CC Operation and pH variation

The VS3 unit was tested for pH variation using a 20L batch of NaCl at a concentration of 1000 ppm, operating in constant current mode. A 3-way junction was positioned near the CDI outlet and recirculated back to the reservoir to enable the use of a flow cell conductivity meter. A conductivity sensor was installed at the nearest water outlet to assess the instantaneous concentration change at the outlet of the CDI stack. Downstream of the conductivity sensor, an AKTA pH sensor was connected to monitor pH variations over time, with the sensor unit placed adjacent to the conductivity sensor. The AKTA sensor was equipped with a dedicated system for flushing and calibration.

3.4.4.1 Results and Discussion:

The pH changes during the adsorption-desorption cycle were monitored and analysed. The initial pH of the feed solution was measured at 5.9, establishing the baseline. The results of both the adsorption and desorption phases are discussed as follows:

pH variation in the Adsorption cycle:

The adsorption cycle commenced by toggling the H-bridge switch to adsorb mode, which resulted in an initial spike in the pH reading—possibly influenced by the electrical field affecting the sensor. This reading was then normalised back to the original value of the feed salt solution. As the adsorption process continued for approximately 11 minutes, the pH remained relatively stable and unchanged. However, after surpassing 700 seconds, the current began to decline, and the cell voltage at the electrode supply connection was recorded at 1.3V, at which point the pH started to rise, reaching a value of 9. Experimental results shown in Figure 27, Figure 28, and Figure 29 clearly indicate that pH levels are high during the adsorption cycle. During constant current operation, the current remains the same while the initial voltage increases from 0.2 to 1.5V.

pH variation in the Desorption cycle:

During the desorption cycle, a sharp increase in pH was observed when the polarity of the electrodes was reversed, with the pH value reaching 12. This sudden spike is believed to be influenced by the electric field. Following this, a gradual decrease in pH was noted as the CDI electrodes discharged, ultimately reaching a pH value of 7 by the end of the desorption cycle. Similar pH patterns were observed during experiments conducted at three different constant current settings: 5A, 7.5A, and 10A.

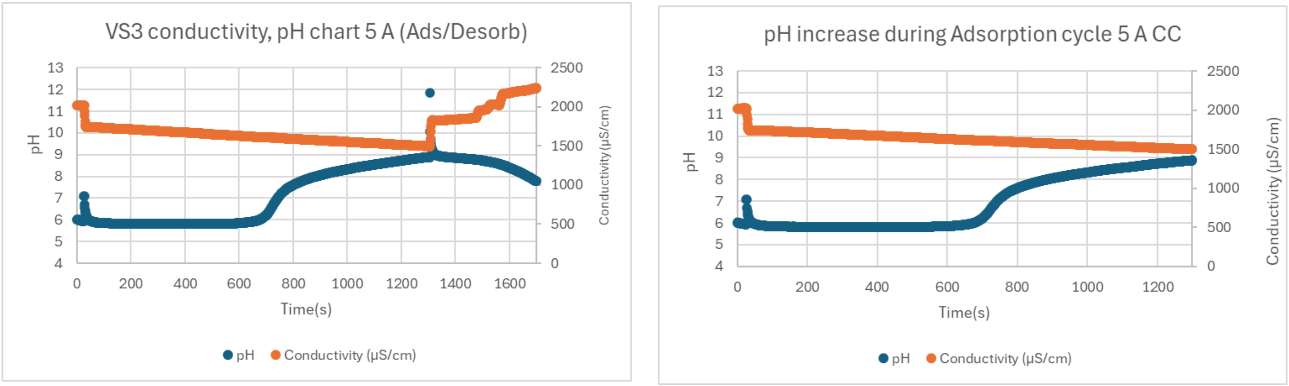

Figure 28 VS3 module CC operation at 5A

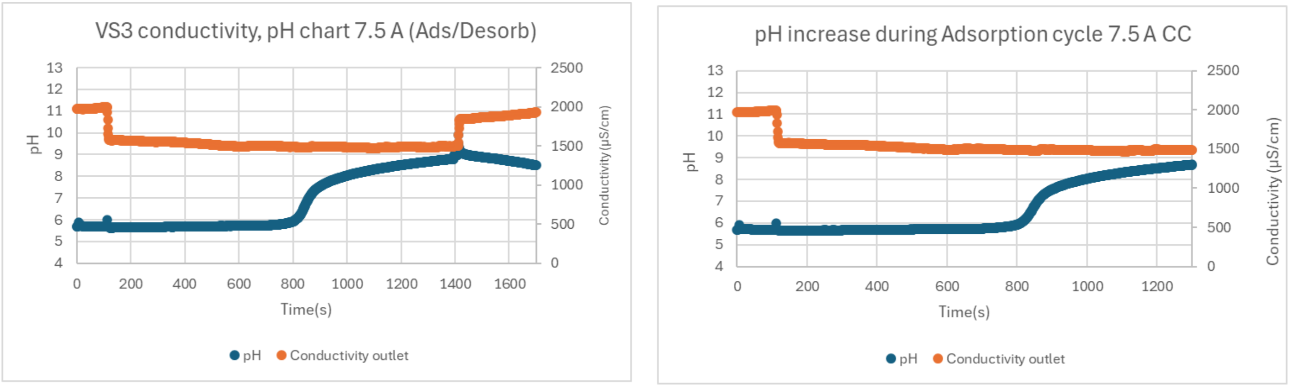

Figure 29 VS3 module CC operation 7.5 A

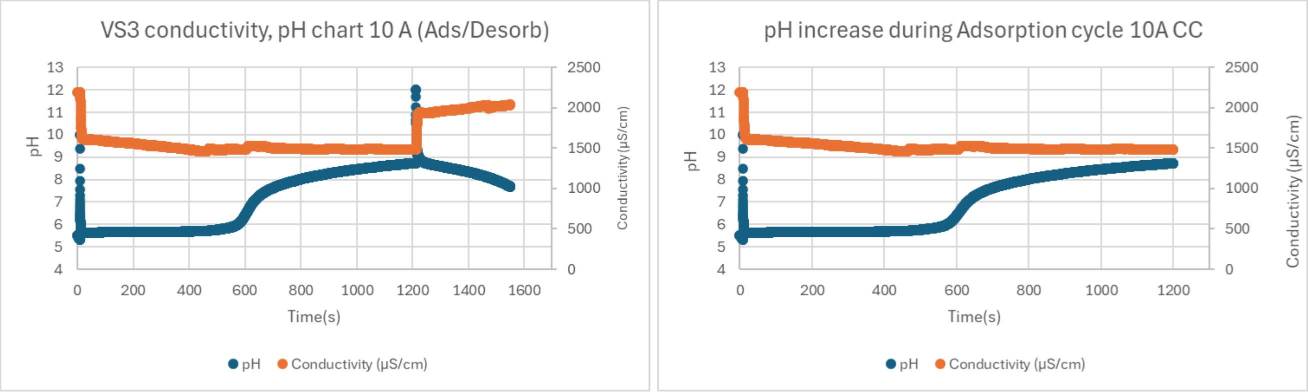

Figure 30 VS3 module CC operation 10 A

The results from these experiments indicate that the pH rose from approximately pH 6 to 9 during the adsorption cycle, highlighting the higher pH region in the spacer channel.

3.4.5 VS3 Electrode Material After Long Service

The images of the industrial VS model electrodes are presented in Figure 31. These images highlight the activated carbon situated on a graphite-based sheet, illustrating the components involved in the system. Additionally, they highlight the fouled membrane and the configuration of the spacer channel mesh, providing a clearer understanding of the functioning and design of the mCDI unit.

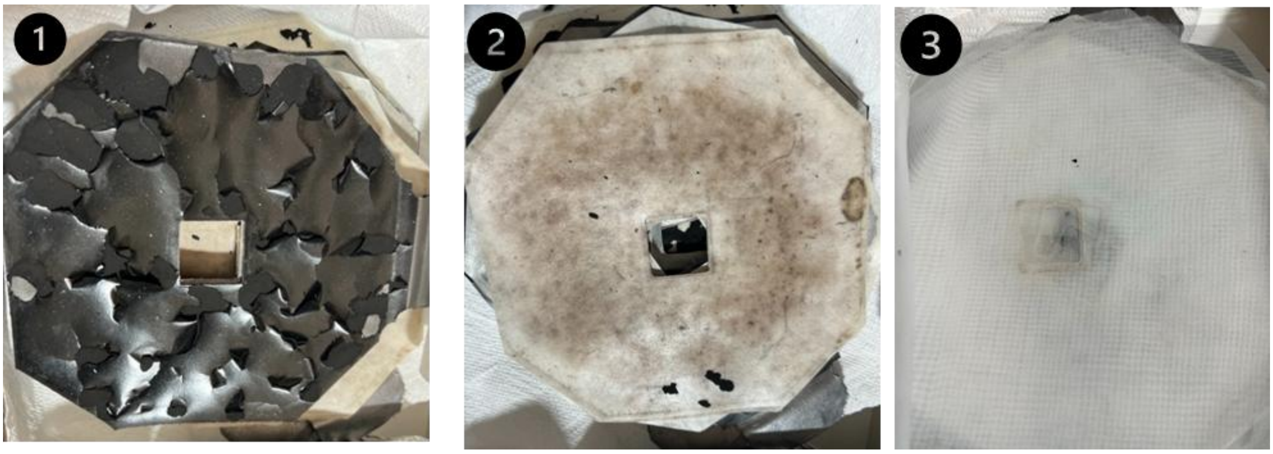

Figure 31 1. VS model CDI electrode AC sheet 2. Ion exchange Membrane 3. Spacer mesh

3.5 Discussion

The major reason for the poor performance of the CDI stack is Initial experiment data showed a very poor power consumption for the corresponding voltage. After the CIP (Cleaning in Place), the performance boost for the same amount of potential difference is applied across the electrode. After each test, the CDI stack was flushed with demineralised water to avoid biofilm formation until further testing. The micropore volume found increased by 27.5 ml in the VS-3 stack.

An earlier experiment in VS3 by (Ott 2023) showed v_{mi} 40 ml, Following the acid cleaning and air scouring, the volume of micropores measured (v_{mi}) reached 67.5 ml for 250g of activated carbon. A significant increase in micropore volume was observed after the treatment of the porous carbon. During the desorption cycle, the peak current consumption was recorded at 39A, indicating a notable improvement in the CDI capacity.

This trend of result highlights the need to further study the internal processes associated with the change in hydraulic properties over time and in response to aggressive, high-energy events like cleaning and scouring.

3.5.1 Circuit Equivalent

The circuit equivalent model helps in understanding the potential and Current characteristics of the CDI stack. The resistive losses through each joint to the final AC stack are calculated; it was found that a 0.4V drop from the power source (power control unit) to the electrode stack at the beginning of the cycle slowly reduces as the current consumption drops. Most importantly, it relates to how the capacitance in the stack behaves.

Zero Volt discharge method data state the discharge characteristics of the CDI. The capacitance of the CDI electrode is obtained with respect to salt concentration. Initial current consumption was seen higher in concentrated electrolyte in CDI system. This key finding can be utilised in performance measuring CDI. Improving energy recovery during ZVD. Optimizing the RVD to ZVD method can save energy spent during the adsorption cycle. 6000F was measured discharged during ZVD by the electrode in the VS-3 model.

3.6 Conclusion.

This experimental chapter goes through the process of characterizing a VS3 electrode module, and establishes key operating characteristics of an aged cell. The modified Donnan model helped in calculating the efficiency of activated carbon electrode by way of the numerical method used to determine the kinetics and capacity of the VS3 module.

The first characterisation method was carried out in porous activated carbon electrode of a CDI stack. The importance of precleaning methods in determining the v_{mi} is compared with the previous tests. The effect of biofouling and scale formation is clear evidence in our experiment in reduced v_{mi} in electrode, The effect of superficial biofilm affects the ion access to micropores.

Furthermore, circuit model results underscored the importance of energy losses occurring in CDI cells. A higher potential at the power control outlet indicates significant power loss across each joint and layer of the CDI section. More economical operations for CDI and energy-saving modes can be achieved; we measured a capacitance of 25 F/g for 1000 ppm salt solution using the circuit model. This experimental result demonstrates that the ZVD mode for desorption, combined with stored capacitance in the CDI stack, allows for effective salt removal and regeneration of the electrode. This approach can save 30-40% of energy in CDI desalination units. This chapter clearly demonstrates the efficiency and accuracy of experimentation and modelling for the characterisation of activated carbon, with the VS3 model with CV mode.

4 Chapter - Development of Indicator System for Observation of pH in CDI by Colorimetry

In the literature review it was established that a number of processes take place within the working mechanism of a capacitive deionisation cell to enable salt removal to occur at such high rates. These include the process of electrosorption, Faradaic reactions, chemical speciation and the convective movement of chemical species in and out of the cell. The CDI effect was established as a combination of these processes occurring within a “stack” of layered materials, the spacer channel being the central portion where chemical species are at a junction in their journey.

Thus far, research efforts have modelled the behaviour of these processes to the extent that commercial products exist. However, questions remain over how well our understanding of these processes reflects the true state of the system. By developing a method of visualising the pH of the observable region of the cell mechanism will advance our knowledge of this technology substantially. This chapter is the first part of the process of developing an in-situ method of pH characterisation in CDI, i.e., the development of the indicator system.

4.1 Introduction

This chapter introduces the concepts related to the indicator system. An indicator system is a dye formulation that varies in colour depending on its pH. The pH colour spectrum and measurement by visible range spectrophotometry were the two concepts serving as the dominant themes during the development. In the upcoming chapters, this indicator formulation will be used during the visualisation of pH in-situ of the microreactor.

4.1.1 Electrosorption of Phosphate: A Motivator for Developing DOTH

Investigations into the electrosorption of phosphate in CDI were first investigated by Dr Kovalsky in 2016, with the first attempt to model simultaneous electrosorption and chemical speciation in COMSOL. Whilst the first publishable findings from this work led to a paper by Huang 2017, some of the speciation modelling work appeared in conference proceedings (Kovalsky 2024).

Phosphate adsorption to MCDI electrodes is complicated by chemical speciation.

$$H_3PO_4 \rightleftharpoons H^+ + H_2PO_4^- \qquad [19]$$

$$H_2PO_4^- \rightleftharpoons \; H^+ + \; HPO_4^{2-} \qquad [20]$$

$$HPO_4^{2-} \; \rightleftharpoons \; H^+ + \; PO_4^{3-} \qquad [21]$$

The equilibrium reactions can be described as follows

$$K_{a1} = \frac{[H^+][\,H_2PO_4^-]}{[\,H_3PO_4]} \quad \simeq 7.5\ C\ 10^{-3}\ \ (pK_{a1}\ 2.12) \qquad [22]$$

$$K_{a2} = \frac{[H^+][HPO_4^{2-}]}{[HPO_4^-]} \quad \simeq 6.2\ C\ 10^{-8}\ \ (pK_{a2}\ 7.21) \qquad [23]$$

$$K_{a3} = \frac{[H^+][PO_4^{3-}]}{[HPO_4^{2-}]} \quad \simeq 2.14\ C\ 10^{-13}\ (pK_{a3}\ 12.67) \qquad [24]$$

So far, we have discussed simple anions such as F^- and Cl^-. They have a -1 charge. The Phosphate involves multiple species with different charges and different diffusion coefficients. The migration of charged species towards the oppositely charged electrode can be described by the Nernst-Einstein relationship. If we look at the governing equation for the transport N_i of a charged species

$$N_i = -D_i \frac{dc_i}{dx} - z_i u_{mj} F c_i \frac{d\phi}{dx} + u c_i \qquad [25]$$

we note three terms on the right-hand side as;

1) diffusive flux driven by the concentration gradient dc_i/dx,

2) migrative flux in an electric field experiencing a potential gradient of df/dx,

3) convective flux where the flow velocity is u m/s.

The Nernst-Einstein relationship u_{mj} is

$$u_{mj} = \frac{D_i}{RT} \qquad [26]$$

Because of these multiple species and their different properties, we can expect the pH (for example) to be variable at various points inside the CDI. Just looking at the above equations it is difficult to picture in your mind what this will look like. In the work of Kovalsky 2024, a COMSOL model of the spacer channel being fed a solution of sodium phosphate was performed. The following assumptions were made.

Assumptions	
Geometrical Scope	Just the Spacer Channel
Physics	- Laminar Flow (SPF), - Secondary Current Distribution (SIEC), - Transport of Dilutes Species (TDS).
Chemistry	Reaction Engineering (RE) – Phosphate speciation
Components	0D – RE 2D – SPF, SEIC, TDS
Geometry	A spacer channel of dimensions 0.5mm by 0.1mm (thick). Flow enters from the left and exits on the right 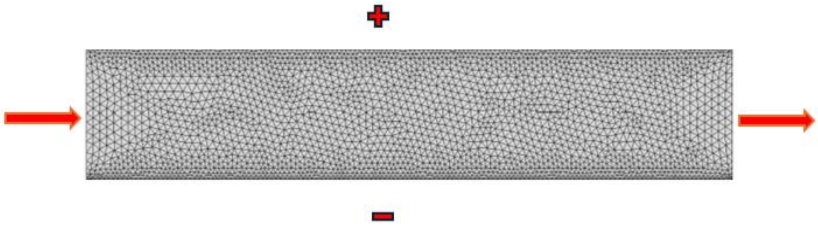

During simulation, the above flux equations attempt to represent the three processes present in a simple CDI spacer channel. This is where ions are moving simultaneously under the influence of diffusive flux, migrative flux, and convective flux, all at the same time but in different amounts at different points in space and time.

The following result of the simulation shown Figure 32 illustrates the simulated change in pH as a function of position inside the spacer channel. There is a clear variation in the x and y planes between 4 and 9. This is somewhat expected as the range of values we might see under the electrosorption of phosphate. In this Figure 32 we have also applied an approximate hue scale to predict what our DOTH indicator might look like

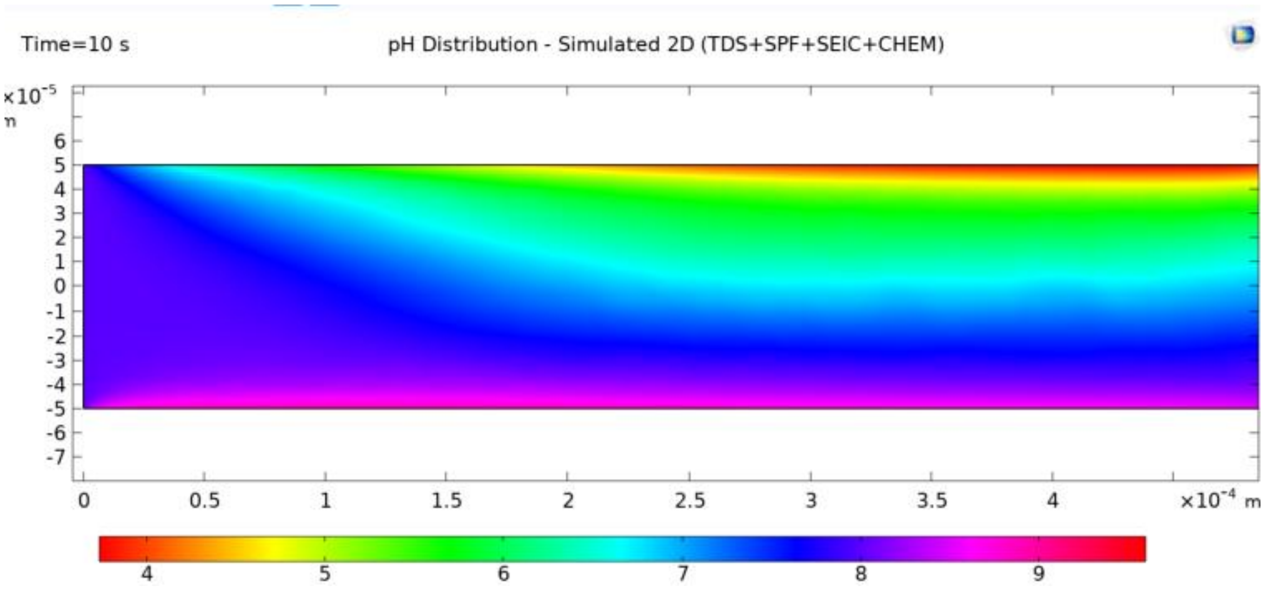

Figure 32 The expected distribution of pH based on simple diffusive, convective and migrative flux under the influence of a CDI electric field and phosphate equilibrium enforced by way of chemical speciation calculations at each time step. We have also applied an approximate Hue scale to predict what our DOTH indicator might look like (image from Kovalsky 2024).

Because of the previous work on phosphate described here conducted by researchers actively contributing to this thesis, this has served as a useful background into why initial work on DOTH involved phosphate-containing systems and quickly recreated results approximating. Figure 32, early in the development of the DOTH procedure, as will be shown later in the section 5. Before we do so, the theory of colourimetry and pH-sensitive dyes will be investigated.

4.2 Background of PH Sensitive Dyes

The DOTH and its development can be considered an incremental innovation in how we visualise protons in solution. In this instance, we are developing a universal indicator that is optimised for use in CDI spacer channels and is robust to various factors that could affect the pH-Hue relationship of our system. Before we embark on the development process, let’s look at the history of pH dyes, colourimetry and the visible colour spectrum.

Many products exist in the marketplace that provide approximate measures of pH. The pH strips found at hardware stores (Figure 33) are examples of such products. Many involve a “universal indicator”, which is a chemical dye formulation that has a distinct light wavelength response after undergoing a chemical reaction

Figure 33 An example of a pH indicator product with a pH-sensitive dye.

4.3 “Colour”

Colour that is perceived by the human eye is made up of hue saturation and brightness. (Jameson and Hurvich 1964). Depending on the source of the light, many different combinations of wavelengths can produce the same colour perception in the eye.

The RGB (Red, Green, Blue) concept of colour has been popularised by the idea that three simple colours can make up white light. By manipulation of micro sized elements of illuminated light, known as pixels on a computer screen, any colour of any wavelength in the visible spectrum can be perceived by the eye by simply blending varying levels of red, green and blue light. The RGB concept has resulted in a simplified understanding of colour and chromaticity. Here, we will explain in more detail the concept of colour and its relevance to producing a novel microfluidic colourimetry system for the in-situ determination of pH.

There are a series of standards and methods for understanding light. The main concepts are;

- Colour perceptions,
- Colour fundamentals,
- Colour vision systems and chromaticity,

- Colorimetry,
- Measurement of colour,

To develop a novel method for measuring pH in-situ to CDI, many concepts above were consulted, studied and utilised in the development of this new technique with the limitations expressed accordingly.

4.3.1.1 Causes of Colour

There is a limited number of discovered physics attributed to the cause of colour in light; these include incandescent gas excitations like neon tubes and auroras. Other physics, such as refraction, scattering and diffraction, are responsible for variations in light colour.

For the device illumination used in this study, lighting was by LED in combination with a 250 µm or 500 µm light pipe made of acrylic for back illumination. The light used was a Jaycar LED Array Type ZD0657 (4400K). The function of the light piping was to achieve consistent colours in the x and y dimensions. The temperature is also assumed to be consistent regardless of luminosity, noting that the light source was connected to a 0-24V variable voltage power supply.

4.3.1.2 Chromaticity – The C.I.E System

The CIE chromaticity diagram represents all colours perceivable by the normal human eye (below). The corresponding wavelengths are labelled adjacent to the colour's chromaticity diagram. Thus, any colour can be expressed in terms of x and y coordinates as shown in Figure 34.

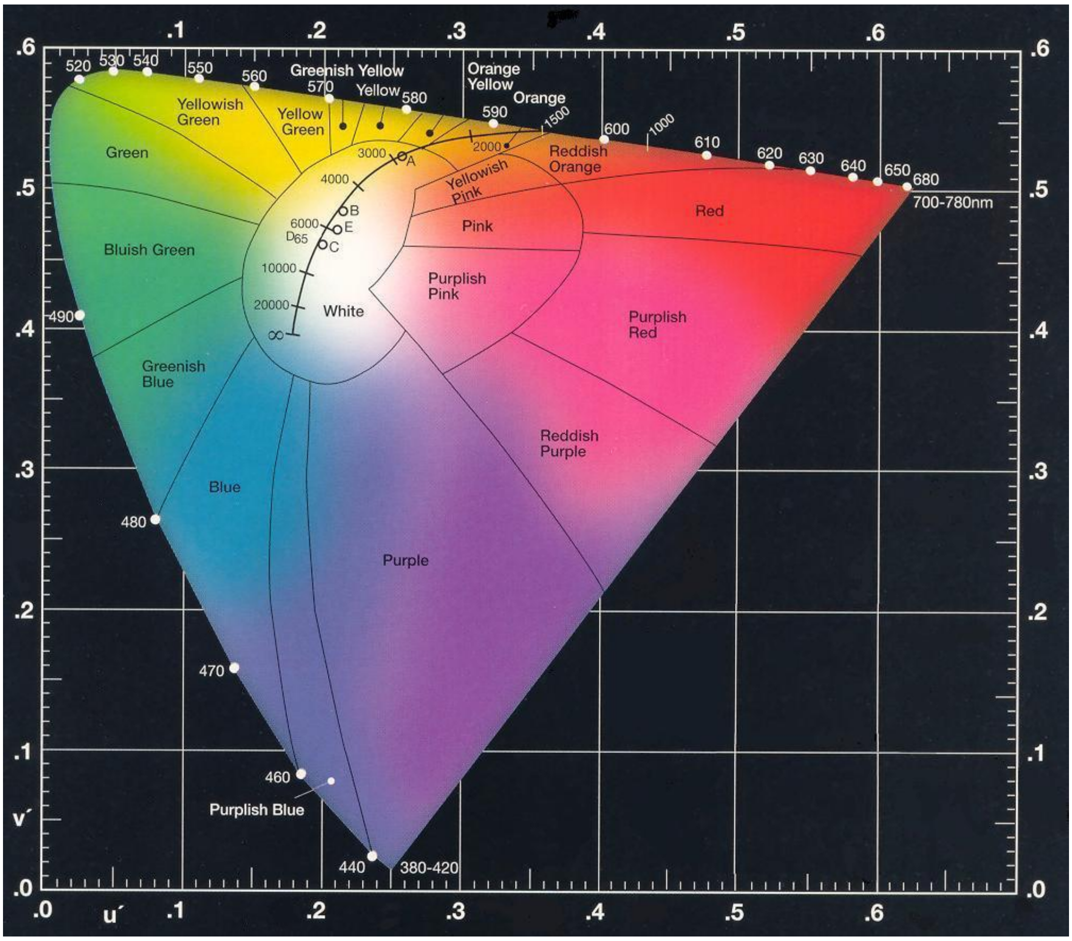

Figure 34 C.I.E Chromaticity diagram.

4.3.1.3 Newton Colour Circle

Newton's colour circle explained additive colour mixing from the basic primary colour RGB. The complementary colours are placed in the circle corresponding to the primary colour. The colour arrangement in the circle follows the wavelength of the respective spectral colours.

In the Newton colour circle (Figure 35), for example, if a visible range absorbance spectra of a solution had a peak at the green wavelength, then the appearance of the solution would be magenta (opposite). Similarly, an absorbance peak at magenta would have the opposite effect, and the solution would appear green. The same can be said for the other colour pairs.

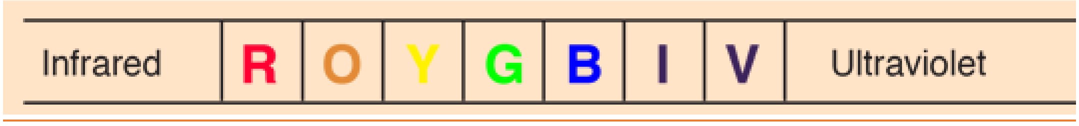

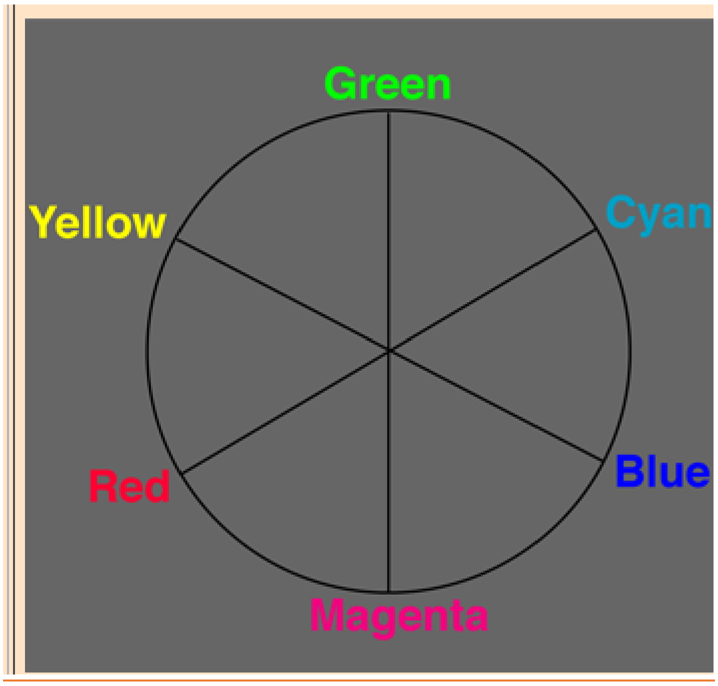

Figure 35 Newton colour circle showing pairs of colours opposite each other (Nave 2024)

Munsell's system (Figure 36) further quantifies the formal colour system in terms of hue (circumference of the circle) and saturation (radius of the circle).

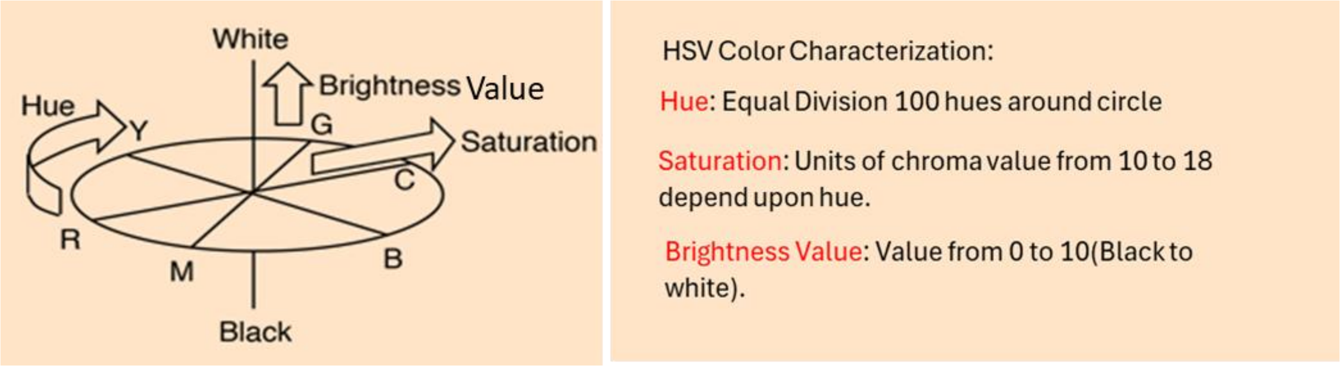

HSV Color Characterization:

Hue: Equal Division 100 hues around circle

Saturation: Units of chroma value from 10 to 18 depend upon hue.

Brightness Value: Value from 0 to 10(Black to white).

Figure 36 Munsell colour system (Nave 2024)

Colour characterisation is done by Munsell and Ostwald by a set of standard colour samples. The colour circle (hue) is divided into 100 equal divisions. Each notable difference in saturation is assigned a unit of radial distance from the centre (unit of chroma). This value differs for different hues, ranging from 10 to 18, depending on the perceptible saturation level. The brightness value is perpendicular to the circular plane formed by hue and saturation. This “Value“ scale is divided into 0 to 10 (black to white). Thus, a colour point is specified by HSV in colour space (Figure 37).

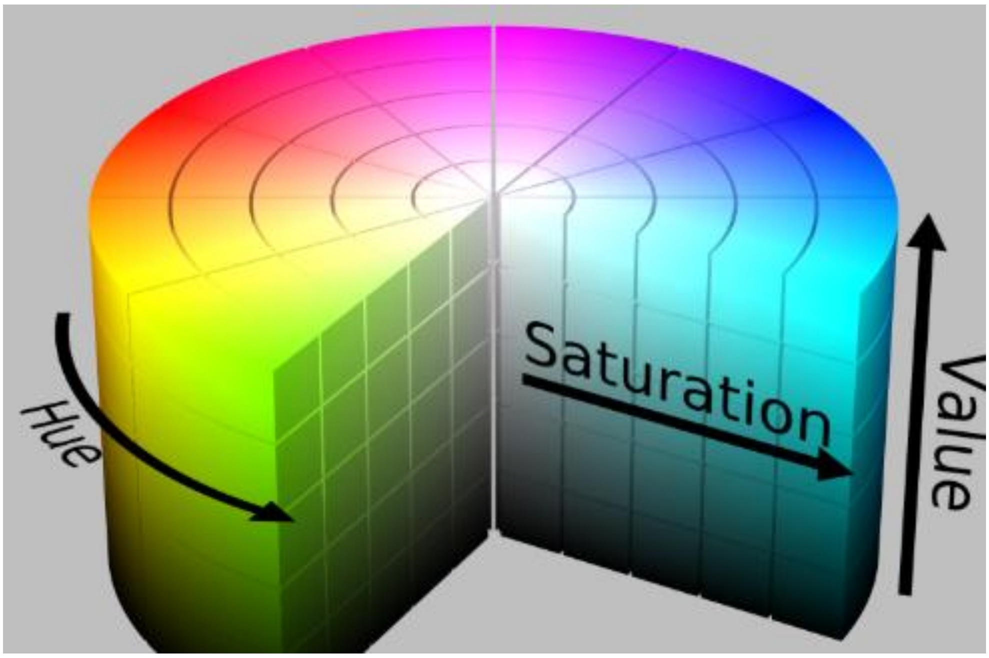

Figure 37 HSV: Pictorial representation of basic colour pattern units Hue (angle of the circle) Saturation (Radius of the circle) Value (Height) of spectrum

4.4 Summary of Requirements- – DOTH Indicator Formulation

The requirement for the dye system was for it to have a hue-saturation-value or HSV colour map correlated to the proton concentration (pH) in the aqueous phase optimised for use in a CDI microreactor. Some of the challenges were optical density within such a narrow rector light-path-length, interference of the dye chemistry with CDI, selective adsorption of the dye at different points in the CDI cycle, precipitation of the dye, presence of volatile organics in the dye formulation, solubility of the dye, chemical speciation of the dye, producing a CDI condition that was realistic to normal operation.

Some of the other challenges of the microreactor were light path length, repeatability, flow pathway, integrity of flow, integrity of the CDI mechanism, excess out-of-plane carbon, uniformity of shape, cross-contamination, inconsistent starting conditions, contact resistance, lighting, focus, chromatic aberration, leaks, But despite these challenges, the experimental design process and systematically overcome each issue by problem identification and designing solutions for them. One of the most important starting points was the dye formulation, method of data acquisition, and data analysis. These three fundamental components were developed in unison and functioned as a cohesive mechanism to produce a satisfactory in-situ method for observing the proton concentration in an electrochemical device.

4.5 Methodology - DOTH Indicator Design

With the requirements now established, the next step was to formulate a chemical system of dyes to have the correct behaviour for the application of observing pH in micron-sized spacer channels under the effect of an electric field.

4.5.1 Dye Selection

Three dyes were chosen for our dye formulation for the purpose of creating a continuous colour sensitive system with a correlation between Hue and pH. That system was robust to deviations in lighting, such as diffusion, diffraction, and scattering. Also, it was robust to dilution of dye and selective adsorption of dye. Also, changes in optics. The ideal system is where Hue is directly correlated to pH to the exclusion of brightness or saturation. Furthermore, we desire this requirement to be present across a very wide range of pH, ideally the full range of 0 to 14. However, such a task is exceptionally difficult. In this study we will demonstrate a technique refined for range 4 to 11 in our microfluidic CDI system under controlled lighting and optics/image acquisition.

The three dyes of choice are Bromothymol Blue (BTB), Phenolphthalein (PH) and Methyl Red (MR). The chemical speciation of each dye is as follows

$$HMr \quad \overset{pKa = 5.1}{\rightleftharpoons} \quad H^{+} + Mr^{-} \qquad [27]$$

The second dye of choice is bromothymol blue, which dissociates as follows

$$HBp \quad \overset{pKa = 7}{\rightleftharpoons} \quad H^{+} + Bp^{-} \qquad [28]$$

The third dye was phenolphthalein as indicated by the following reaction

$$HIn \quad \overset{pKa = 9}{\rightleftharpoons} \quad H^{+} + In^{-} \qquad [29]$$

4.5.2 Preliminary Calculations of Indicator System

Here we simulated the speciation of the dye components in PhreeqC to predict the fraction of each species present at each pH. By understanding the fraction of charged species present, we may understand any effects caused by the CDI process on the charged dye species in advance.

4.5.2.1 Introduction to PhreeqC

PhreeqC is a program that runs in C & C++ languages for aqueous geochemical calculations. It can perform speciation and saturation indices, batch reaction, 1D transport and inverse geochemical calculations. Its most useful feature in this context is the ability to perform equilibrium speciation calculations. This is based on an algorithm that calculates a charge balance on all species present and provides the most thermodynamically consistent distribution of species present. In our case, it can calculate the dissociation of the dye present in our indicator formulation and help inform us on how to prepare our formulation to meet our unique set of pH indicator objectives.

Solution batch mixing is selected for this experiment. This program has three important parts: input data, output data, and a database file.

Input Data

Solution Input properties feed data such as temperature pH, composition, and feed properties are mentioned are entered as per Table 8.

Table 8 PhreeqC solution input data details

Parameter	Value	Description
temp	25	Enter the solution temperature
pH	7 charge	pH value to be adjusted to charge balance
pe	4	Negative log of activity of electron default value is 4
redox	pe	Redox couple used to calculate pe-default value pe or 4
units	mmol/kgw	concentration unit
density	1	solution density in Kg/L
Bp	1	element item1
Na	51	element item2
P	21	element item3
water	1 kg	water mass in Kg

Output Data;

- Initial solutions calculation,
- Composition, description of solution(properties), distribution of species, saturation indices calculation,
- Mixed solutions calculation by batch reaction using the database. The solution species are calculated using gamma, *dW* (diffusion coefficient (molar volume) values from the database, and aqueous species are calculated using *log_k* value(equilibrium constant), enthalpy, *dW*, and *Vm* values from the database.

4.5.2.2 Methodology - Input File Configuration to Simulate Indicator Speciation

The PhreeqC simulation contains an input file containing the starting concentration of an equimolar mixture of Phenolphthalein (In) and Bromothymol Blue (Bp) 0.001M, but a 0.1 fraction of Methyl Red (Mr) 0.0001M due to its reduced solubility in the dye mixture.

The input file containing all 14 solution definitions is provided in the Appendix. 9.4. Similarly, the custom database entry for the three dye compounds is included in the appendix. This input file was used to perform a simulation.

4.5.2.3 PhreeqC Result – Distribution of Dye Species at Different pH

The simulation of the PhreeqC input file in Appendix 9 produced the following distribution of chemical species resulting from the dissociation of each of the three acid dyes. For each dye, three figures are provided (Table 9): the amount of undissociated dye, the amount of dissociated dye anion, and the fraction of the anion dissociated relative to the original amount of dye added. In this case, it was 0.0001M Mr denoted as starting concentrations HMr0, 0.001M Bp as HBp0 and 0.001M Hin as Hin0.

In UV spectroscopy and colourimetry, chemical compounds that vary the spectrum of wavelengths adsorbed in response to a change in pH are documented extensively in the scientific literature. In the third row of each dye column, we denote the expected colour at each fraction of dissociation based on a simulated mixing of the three individual colours in the column on the left.

Dye results of chemical speciation calculation of a mixture of 0.0001M methyl red, 0.001M bromothymol blue and 0.001M phenolphthalein. The colours presented are general approximations from direct visual observation for the individual dye, and the far-right column is a projection of the colour obtained by observation.

Table 9 Chemical speciation of dyes present in UI dye.

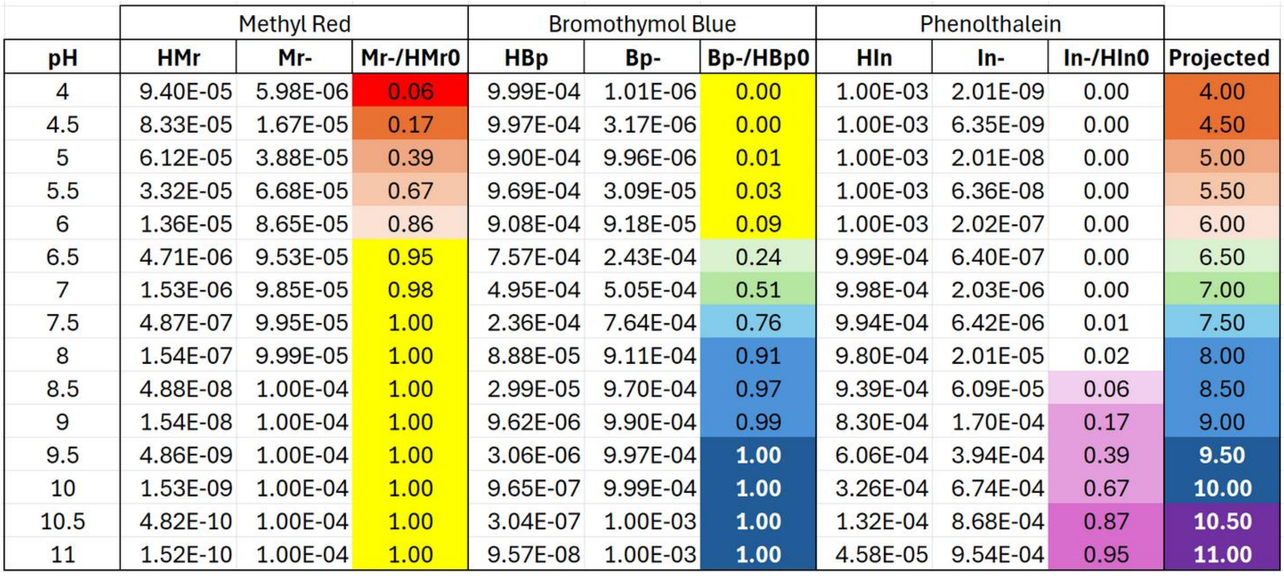

	Methyl Red			Bromothymol Blue			Phenolthalein			
pH	**HMr**	**Mr-**	**Mr-/HMr0**	**HBp**	**Bp-**	**Bp-/HBp0**	**HIn**	**In-**	**In-/HIn0**	**Projected**
4	9.40E-05	5.98E-06	0.06	9.99E-04	1.01E-06	0.00	1.00E-03	2.01E-09	0.00	4.00
4.5	8.33E-05	1.67E-05	0.17	9.97E-04	3.17E-06	0.00	1.00E-03	6.35E-09	0.00	4.50
5	6.12E-05	3.88E-05	0.39	9.90E-04	9.96E-06	0.01	1.00E-03	2.01E-08	0.00	5.00
5.5	3.32E-05	6.68E-05	0.67	9.69E-04	3.09E-05	0.03	1.00E-03	6.36E-08	0.00	5.50
6	1.36E-05	8.65E-05	0.86	9.08E-04	9.18E-05	0.09	1.00E-03	2.02E-07	0.00	6.00
6.5	4.71E-06	9.53E-05	0.95	7.57E-04	2.43E-04	0.24	9.99E-04	6.40E-07	0.00	6.50
7	1.53E-06	9.85E-05	0.98	4.95E-04	5.05E-04	0.51	9.98E-04	2.03E-06	0.00	7.00
7.5	4.87E-07	9.95E-05	1.00	2.36E-04	7.64E-04	0.76	9.94E-04	6.42E-06	0.01	7.50
8	1.54E-07	9.99E-05	1.00	8.88E-05	9.11E-04	0.91	9.80E-04	2.01E-05	0.02	8.00
8.5	4.88E-08	1.00E-04	1.00	2.99E-05	9.70E-04	0.97	9.39E-04	6.09E-05	0.06	8.50
9	1.54E-08	1.00E-04	1.00	9.62E-06	9.90E-04	0.99	8.30E-04	1.70E-04	0.17	9.00
9.5	4.86E-09	1.00E-04	1.00	3.06E-06	9.97E-04	**1.00**	6.06E-04	3.94E-04	0.39	**9.50**
10	1.53E-09	1.00E-04	1.00	9.65E-07	9.99E-04	**1.00**	3.26E-04	6.74E-04	0.67	**10.00**
10.5	4.82E-10	1.00E-04	1.00	3.04E-07	1.00E-03	**1.00**	1.32E-04	8.68E-04	0.87	**10.50**
11	1.52E-10	1.00E-04	1.00	9.57E-08	1.00E-03	**1.00**	4.58E-05	9.54E-04	0.95	**11.00**

Methyl Red

Here it is interesting to note the fractional change of colour between 4 (Red) and 6 (Yellow) with orange in between.

Bromothymol Blue

For Bp, we observe a transition from 6 (Yellow) to green at 7, blue at 8 and darker blue from 9 to 11. Yet one could argue a change in saturation rather than a change in hue is the more dominant change, reference (Figure 37).

Phenolphthalein

When looking at In, we see the expected behaviour of the solution is clear in colour up until pH 8. In fact, at about pH 8.2, the first signs of pink appear, with full saturation around pH 10.5. Here, we see that phenolphthalein is unique in that it is the only dye that has no change in hue across the whole pH range. According to the HSV definition, the only parameter that appears sensitive to pH is the *S* (saturation) and/or *V* parameter (brightness).

Another interesting issue worth raising here is the electrosorption of the dissociated dye ions. In all three cases, they are anion versions of the dye. One might expect some electrosorption to occur, but due to the low charge-to-mass ratio, it will be insignificant over the short time scales we are investigating.

4.5.3 Analysis and Recommendations of Theoretical Investigation

At this point, we emphasise the critical nature of the continuous pH-hue response to the viability of the DOTH technique. Having analysed the PhreeqC results and their potential effect on colourimetry, we can begin to define our requirements for a DOTH indicator. This shows an ideal example of an indicator that starts at 12 O'clock (green) with pH6 and ends at 4 O'clock with pH 11 (purple). In this example, the relationship is a continuous, monotonically increasing function (Figure 38).

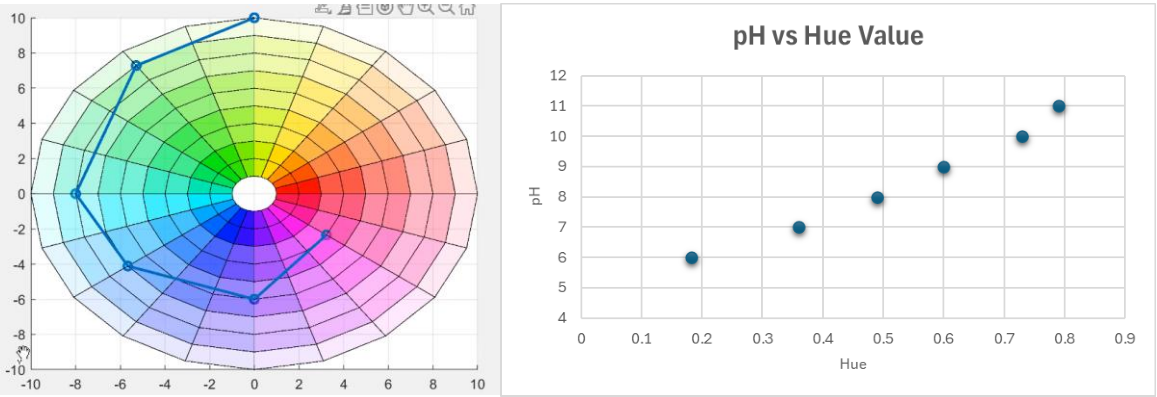

Figure 38 A viable pH vs Hue relationship (left), in this case, a continuous monotonically increasing function (right) that we wish to formulate.

The objective is to make a formulation comprised of dyes with the following characteristics;

- Highly concentrated – given the extremely short light path length of 100-1000μm, to discern light within the dynamic range of the CMOS (Complementary Metal-Oxide-Semiconductor) sensor being used requires the concentration to be sufficient to absorb light (Beers Law),
- Dyes must be soluble within the range of conditions experienced in the CDI spacer channel,
- Indicator must have low sensitivity of variation in hue to variation in indictor concentration such that minor electrosorption of any dye component does not have excessive variation on the pH-hue relationship.

Three different dyes are selected: phenolphthalein, bromothymol blue, and methyl red. The preparation of the DOTH indicator formulation will be given in the next section.

4.6 DOTH Indicator Preparation

The First stage of formulating concentrated dye is preparing individual dyes.

- Phenolphthalein dye:

This preparation step aimed to get a concentrated dye solution without any crystals in the container. Phenolphthalein (weak acid) 1g powder was measured in a petri dish. Meanwhile, 20 ml of ethanol was taken in a 100 ml beaker provided with a magnetic stirrer, and then 10 ml of milli-Q water was added to the beaker. Phenolphthalein powder was added slowly to the beaker while the solution was mixed at a medium speed using a magnetic stirrer. Mixing continued until a clear solution was obtained in the beaker. During mixing, a drop in liquid level was observed due to the evaporation loss of ethanol, and an additional 5 ml of ethanol was added to compensate for the evaporation loss. It was important to add this additional 5 ml ethanol after mixing. Otherwise, phenolphthalein crystals can be seen at the bottom of the storage container, which could affect the performance of UI dye.

- Bromothymol Blue dye:

Similar to the Phenolphthalein dye preparation steps, the concentrated BTB dye is prepared. 0.1 g of BTB powder weighed in a petri dish. 20 ml of ethanol was measured in a beaker with a magnetic stirrer. BTB powder was gradually added to the beaker with a stirrer at medium speed, and then 20ml of milli pure water was added to the solution. The mixed solution was transferred to a container and kept closed to avoid ethanol evaporation loss.

- Methyl Red Dye:

Unlike the previous 2 dyes, Methyl red has a different physical property while dissolving. There is an additional filtration step followed by dissolution.

Methyl Red (weak acid) 0.1 g weighed in scale and taken in a Petri dish. 12 ml of ethanol was taken in a beaker with a magnetic stirrer. While stirring the ethanol in the beaker, methyl red powder was added slowly to the beaker. An additional 10 ml of ethanol was added after adding the powder. 5 mins of continuous mixing was allowed, and then an additional 5 ml of ethanol was added. Once a satisfactory clear solution was obtained, milli-Q water 10 ml was added to the solution and mixed thoroughly. It was crucial to clearly remove the methyl red dye crystals from the concentrated solution as this could negatively affect the performance of UI dye in the microreactor. Mixing was stopped, and the solution settling time of 15 minutes allowed to separate fine MR suspended powder. Then the solution was poured into a fresh beaker containing funnel and a Whatman filter paper. Gravity filtration was followed for this filtration step. The residue in the filter paper was discarded carefully. Due to the precipitating nature of methyl red from the prepared solution, an optimum concentration was chosen.

All these dyes are well-soluble in ethanol. To avoid ethanol evaporation loss, they must be kept contained. The storage container must be closed immediately after each use.

The ratio of IN: BTB: MR is 1:1:2; this combination is obtained by different trials.

4.7 Results of Indicator Formulation

The formulated dye, after different trials, was red in colour (Figure 39) and had a pH value of 2.74. The density of the dye solution was found to be 0.93 kg/L. The evaporation rate tested in the laboratory atmosphere was observed as a 10% drop in volume per hour. The reaction with activated carbon was checked, and it was found adsorbed in the electrode surface while placing a drop of dye in the microreactor after priming the electrodes. The filterability was checked with Whatman 40 grade paper (8μm); it was permeating easily through the filter media, leaving no residue at room temperature. The dye concentration test was conducted by mixing the dye with a titrated solution of sodium phosphate and phosphoric acid. When the dye concentration exceeded 5% by volume in the experiment, the MR dye tended to precipitate out of the solution, settling at the bottom at room temperature. Figure 39 illustrates the absorbance values obtained from the Vernier spectrophotometer, indicating a high absorbance within the spectrum ranging from 400 to 600 nm.

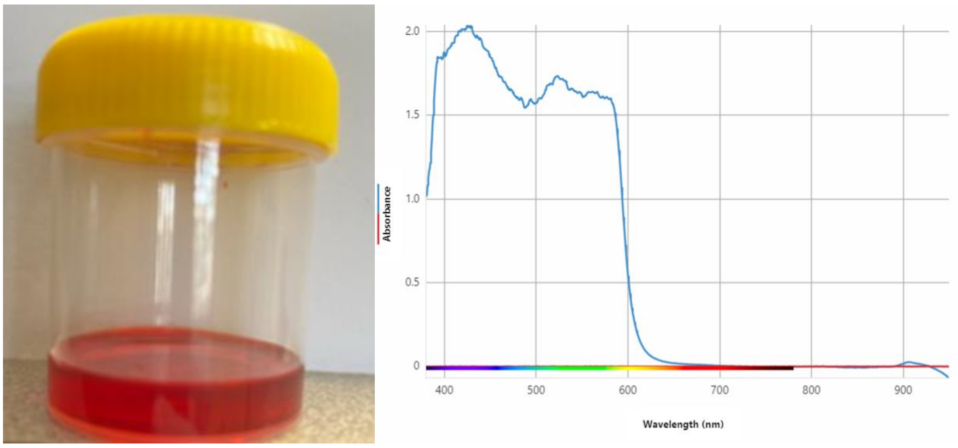

Figure 39 Formulated UI dye (1:1:2) (left) and absorbance value of concentrated UI dye spectrum (right)

4.8 Conclusion

Overall, a stable, functional, highly concentrated dye was synthesised and tested. The dye demonstrated compatibility with the specific application, with a pH of 2.74 and a density of 0.93 kg/L. However, the evaporation loss, which was 10% per hour due to ethanol loss, indicates the importance of following controlled storage conditions to preserve the dye's stability and functionality.

The visible range spectra were recorded for reference purposes indicating strong absorbance across a broad spectrum of the 400-600nm range at its native pH of 2.74. The anticipated pH-Hue characteristics were well defined in preparation for indicator characterisation in Chapter 5 at varying pH.

5 Visible Range Spectrophotometry Characterisation of DOTH Indicator System

As set out in previous chapters, there are many requirements and constraints for a DOTH indicator to perform in situ to a range of applications being developed here. These are the microreactor, which measures 250µm by 1000µm by 3000µm (or 750 picolitres) functioning as a CDI device. In this chapter, we define the functionality of the DOTH system, define its practicality and limits, and establish quantitative and scientific rigour in this new technique.

5.1 Introduction

Having developed the indicator formulation in Chapter 4 and establishing the objectives behind developing a robust pH/Hue function, we now examine the performance of the DOTH formulation under controlled conditions where the visible range spectrophotometer (VIS) can be characterised and pH measured under microreactor flow conditions.

In our study of the pH dependence of the indicator system, we have established the following workflow;

1) Formulate the indicator system as a concentrate with the prescribed ratio of the three dyes. This can be later diluted as needed per application,

2) Test the effect of pH on the indicator system by way of a controlled experiment with a flow cell pH meter and VIS in the flow loop and a controlled method of adjusting the pH in the loop. This is known as the Flow Cell Experiment,

3) Apply the OSRAM Color Calculator v7.59 colour space transformation to simulate the process of colorimetry from a range of VIS spectra at different pH (5, 6, 7, 8, 9, 10 and 11). These pHs were chosen as the initial scope was to investigate phosphate speciation in the CDI spacer channel with an expected pH range of 5 to 11,

4) Observe the hue using a microscope and image acquisition system focused on imaging the flow cell under controlled lighting and image analysis in MATLAB (import video->analyse individual frames-> select pixels -> identify RGB values -> convert RGB to HSV -> apply

hue to pH function -> pH calculated at all points in space). This is also known as a spatial colourimetry system,

5) Compare the observed hue through the microscopic colorimetry system with the hue predicted by the VIS spectrophotometer and CIE1976 colour space transformation.

Using this technique, we would like to ascertain the sensitivity of the pH-Hue function to changes caused by dye electrosorption or other physical/chemical effects. Thus, the aims of this chapter will be given next.

5.1.1 Aims of Chapter

The aim is to create an investigative framework for characterising the sensitivity of the pH-Hue function to physical or chemical changes in the indicator system. The motivation is to determine how confident we are in using our custom imaging system as a spatial colourimetric method to determine the pH distribution. As we suspect one of the dye components may selectively electrosorb from the system it is necessary to investigate this phenomenon. Thus, the aims of this chapter are;

- Investigate the sensitivity of the pH/Hue function to variation in any one chemical component of the indicator system,
- Apply the data theory used to characterise the indicator system as developed in Chapter 4,
- Simulate expected behaviour and compare to results.

5.2 Methodology – Flow Cell Experiment

The purpose of the flow cell experiment was to measure the pH and collect absorbance readings.

The flow cell experiment was a closed-loop circulation of the DOTH indicator through the titrated solution from the working solution reservoir through the pump and UV-vis apparatus for analysis as illustrated in Figure 40.

5.2.1 Flow Cell Experiment Setup

The flow cell experiment had several hydraulic constraints and, as such, had to be ordered in a particular sequence with fluidic features positioned at locations to address constraints and retain certain key functionality. Many constraints were requirements on precision and maintaining good quality data.

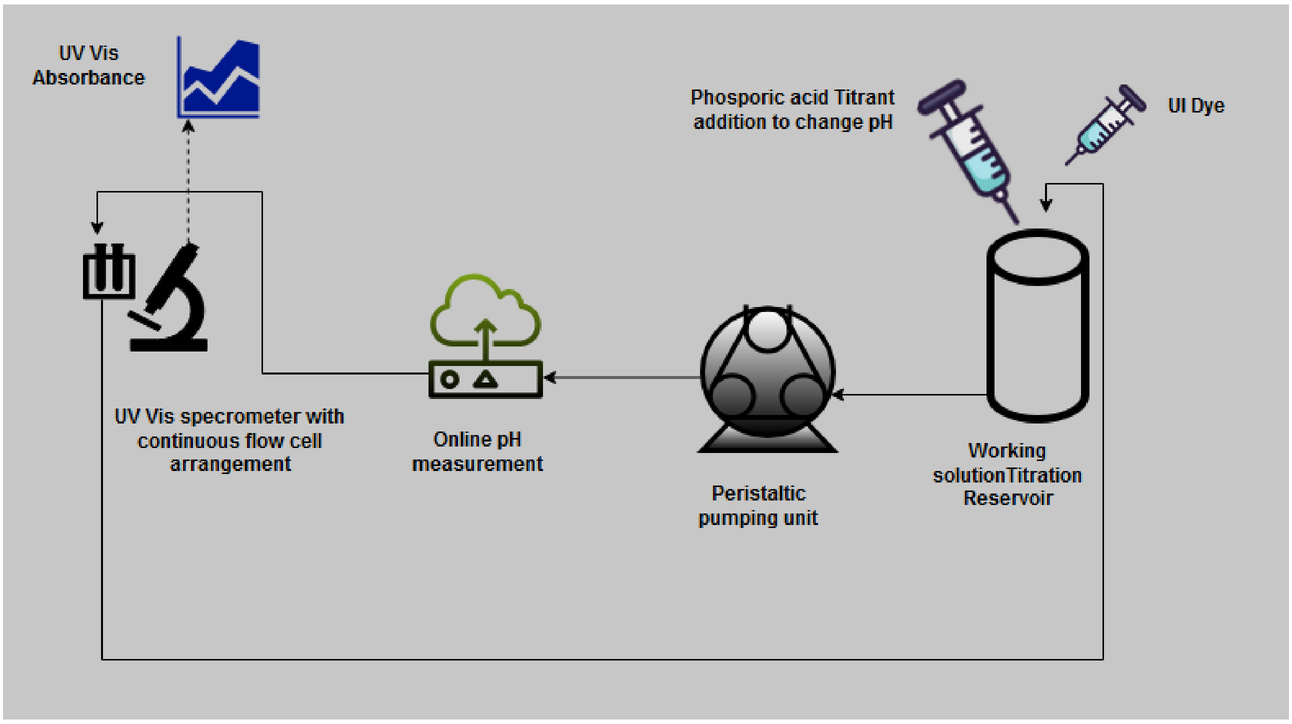

Figure 40 UV-Vis experiment setup

5.2.1.1 Working Solution Titration Reservoir

The reservoir was fabricated out of a 50mL polyethylene container with an outlet hole created by drilling/tapping a ¼” hole near the bottom of the reservoir and installing a female luer-to-¼” thread fitting. This reservoir could be left closed or opened to add reagents to the circulating loop of the reagent mixture.

5.2.1.2 AKTA Flow Cell pH Sensor

The AKTA flow cell pH sensor is ideal because of its low dead volume which was required in microfluidic applications. The low dead volume makes the sensor more responsive.

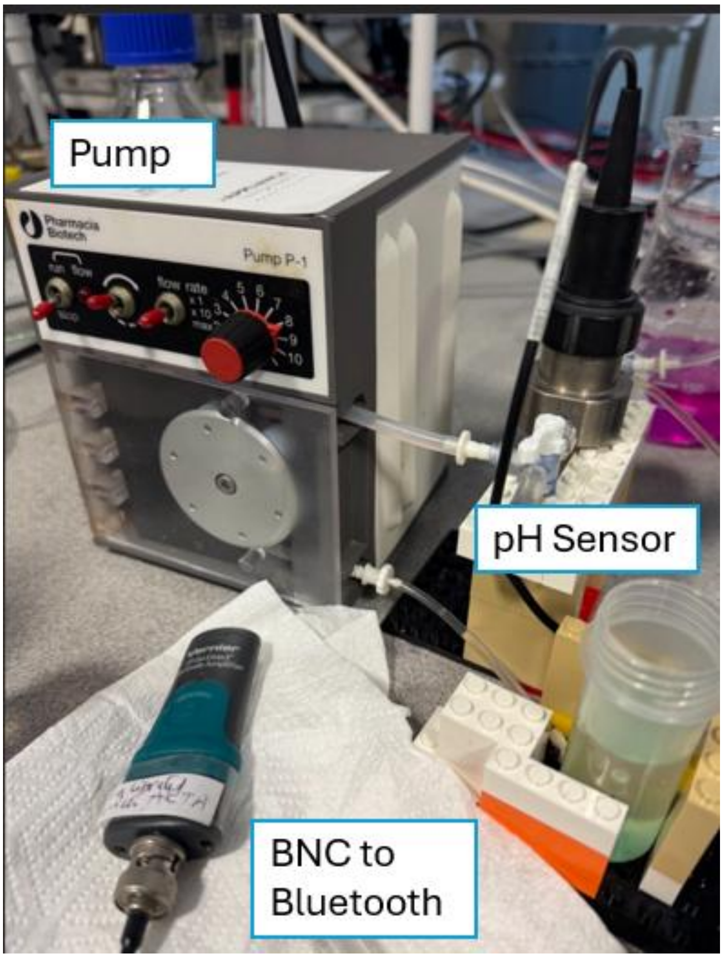

Figure 41 The pH sensor is connected to the BNC to bluetooth adapter. Conversion from mV to pH is done on the host computer capturing the data in a vernier graphical interface at one-second intervals.

AKTA pH Sensor Calibration

The expected calibrated electrode slope is shown in Figure 42. The manufacturer's recommended sensor response shows a 1V full range for the sensor, well within the Vernier BNC to Bluetooth adapter specification. The calibration procedure used was to connect the AKTA pH/C-900 Flow Cell to the Vernier BT-BNC adapter (Figure 41) and used the VGS software 3-point calibration procedure. The calibration values chosen corresponded to the range of calibration solutions available to us, Merck CertPUR (NIST certified) values 4, 7 and 10.

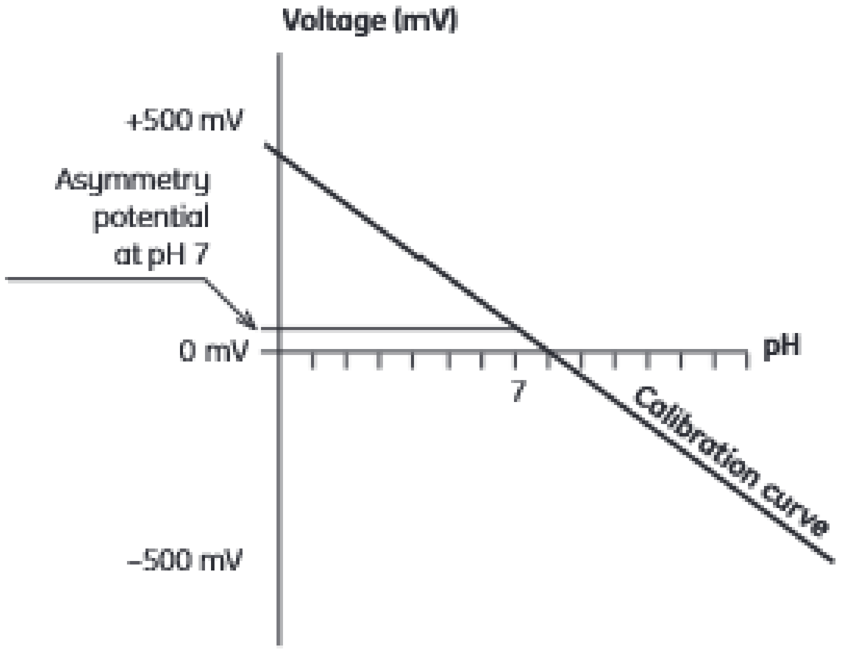

Figure 42 The manufacturer-recommended sensor response shows a 1V full range for the sensor, well within the vernier BNC to bluetooth adapter specification.

5.2.1.3 Visible Range Spectrophotometric Flow Cell

A Vernier GO Direct SpectroVis Plus was used in flow cell mode using a flow cell cuvette. The full spectrum resolution was 1nm~wavelength intervals at points in time when the flow condition was stable.

A visible range spectrophotometer uses an incandescent white bulb with a detector range of 380-950nm. Given that our ultimate application is colourimetry, a visible range spectrophotometer (Figure 43) is sufficient for our work.

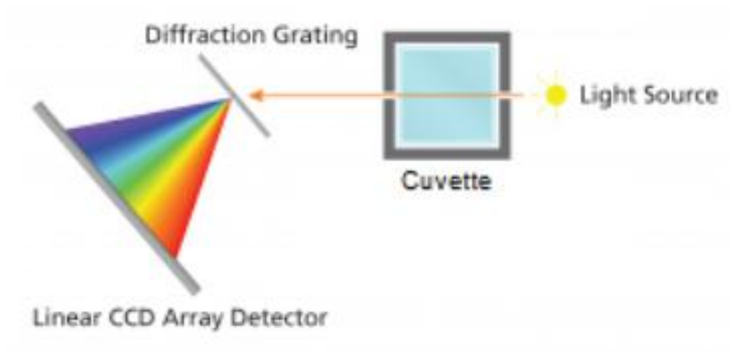

Figure 43 Visible range spectrophotometer

The configuration of the flow cell loop is shown below in Figure 44**Error! Reference source not found.** Go-Direct SpectroVis plus device for VIS experiment setup with pH-11 (purple colour) (with cuvette light-blocking cover not affixed).

Figure 44 Go-Direct SpectroVis plus device for VIS experiment setup with pH-11 (purple colour).

5.3 System Assembly Steps

The system integrates working fluid circulation, continuous online monitoring of pH value, and inline modified VIS spectrophotometry for continuous spectral measurement using the flow cell.

5.3.1 Preparation of Liquid Circulation Loop

Peristaltic pump P-1 was equipped with suction discharge silicone tubing, and the pump head and hoses were securely locked to avoid leakage. Constant flow was checked separately, suitable tubing size was chosen for the required flow rate for the experiment approx. 3ml/min. The AKTA pH sensor with the dedicated flushing and calibration arrangement was connected downstream of the titration reservoir for continuous pH monitoring. The flushing arrangement provided a 3-way valve and flushing lines to flush the sensor immediately after the experiment and recalibrate it.

A modified UV-VIS cuvette was fixed in an arrangement with the reservoir level into a flow cell to continuously measure pH spectrum absorbance readings. During the initial trials, the flow cell outlet tubing height was adjusted and fixed for continuous flow and maintaining levels in the flow cell. In the later stage of the experiment, an adjustable stage was used to maintain the constant liquid level in the flow cell. Additionally, base plates were used in the reservoir to ensure the proper liquid level was maintained while capturing the absorbance reading in the spectrophotometer device. Base plates were adjusted for the VIS flow cell hydrostatically to balance the level in the flow cell.

5.3.2 Leak Test and Flushing

The pump, AKTA pH meter, reservoir, and flow cells were initially connected without the spectrophotometer. After verifying the valve arrangements, the system was flushed with demineralised water and checked for leaks. The reservoir was filled with 10 ml of demineralised water, and the pump was activated to circulate the fluid for 5 minutes. Subsequently, the flow cell was connected to the spectrophotometer setup, and proper fluid flow was established, ensuring that the flow cell remained level. This precaution was taken to prevent any chemical spillage into the spectrophotometer during the operation with chemicals. Once the leak test was confirmed, the system was thoroughly flushed before introducing any chemicals. The AKTA pH meter underwent calibration using the stand-alone calibration flushing arrangement, employing a 3-point calibration method.

5.3.3 Chemical circulation & Titration

5.3.3.1 Chemical Circulation

The system reservoir was drained for flushing with demineralised water. A 5 ml syringe fitted with a 22G needle was used to fill the reservoir with the saturated sodium phosphate solution. This base solution was introduced through the top of the reservoir. It's essential to ensure that there is no colour change in the reservoir upon adding the colourless sodium phosphate; any residual dye present from improper flushing will cause the sodium phosphate to turn pink or purple. This indicates the need to empty the system again and properly flush it with demineralised water.

5.3.3.2 Titration

Once the sodium phosphate reservoir was filled, a few drops of concentrated dye were introduced using a 1 ml syringe. The saturated sodium phosphate with dye exhibited a purple colour. This colour development was observed throughout the reservoir, pump, sensor, and return line as the dye circulated through the system. Circulation was maintained for 5 minutes. The initial pH of the saturated sodium phosphate was recorded at 11.4. A 2.5% weight/weight solution of phosphoric acid was prepared and placed in a beaker, ready for titration, with two drops of UI dye mixed in to compensate for the loss of acid added to the system. This step ensured a constant dye concentration throughout the titration process. Circulation was conducted to obtain spectra at various pH levels (11, 10, 9, 8, 7, 6, 5, and 4) by adding dilute H_3PO_4 dropwise to the saturated Na_3PO_4 with the dye. At each pH level, circulation was maintained for 5 minutes to achieve stable pH readings on the sensor, and samples were collected at each pH interval.

5.3.3.3 Post-experiment Cleaning of the System

The AKTA pH sensor was initially flushed with deionised water using the designated flushing arrangement, and the pH reading was recorded at the end of this process. Upon completing the trial, the system underwent 3 to 5 additional flushes to thoroughly clear the dye from the system. Deionised water was added to the reservoir and circulated. The return line from the flow cell was disconnected and redirected to a dump container, after which the pump was activated. Initially, residual dye in the system caused the deionised water to appear green. The flushing of the flow cell was performed carefully while maintaining system circulation. Calibration with deionised water in the spectrophotometer was conducted before each absorbance test. The reservoir was filled and flushed repeatedly until clear deionised water was observed in the system. In the final run, the flow through the AKTA sensor was confirmed to have a pH of 7.

5.3.4 Converting Spectra to Hue Values

Once the spectra are obtained, the OSRAM Colour Calculator converts them into CIELUV values. CIELUV values at the located points are converted to RGB, and then MATLAB's built-in RGB2HSV function is used to extract the hue values (Figure 45).

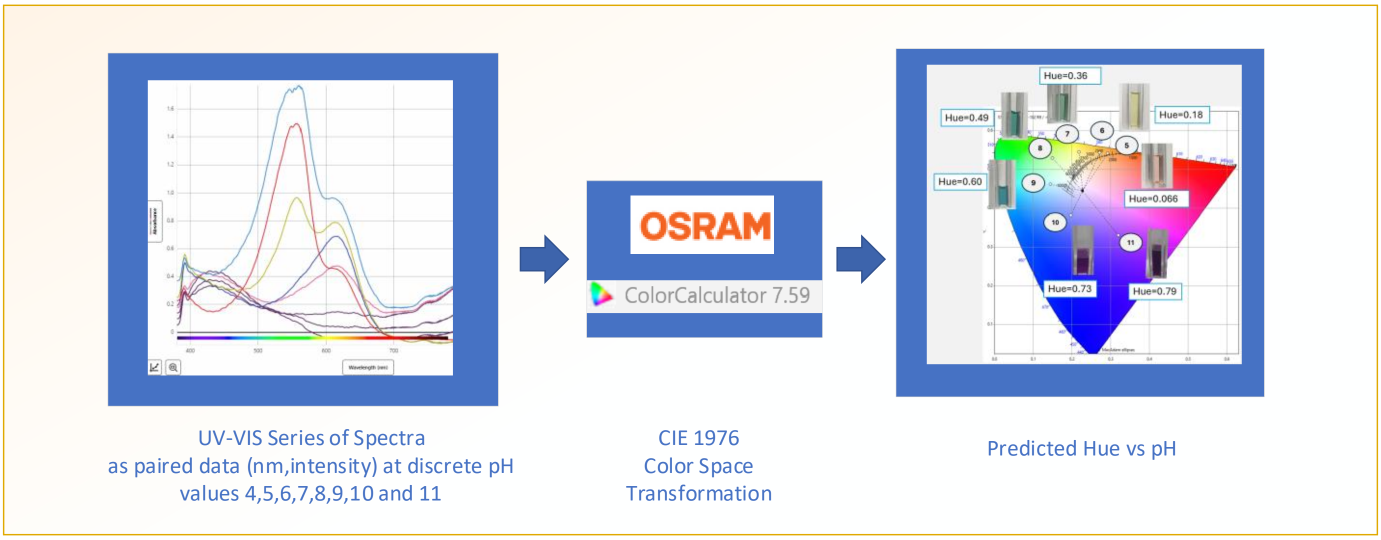

UV-VIS Series of Spectra
as paired data (nm,intensity) at discrete pH
values 4,5,6,7,8,9,10 and 11

CIE 1976
Color Space
Transformation

Predicted Hue vs pH

Figure 45 Spectra Conversion to Hue values in CIE OSRAM software

To convert CIELUV (L*, u*, v*) to RGB, then ultimately HSV, the following equations were used(CIE 2018). The variables with subscript '*n*' refer to values of the white point which depend on the standard illuminant used. The incandescent light used in the spectrophotometer requires standard illuminant A to be used, which has luminance $Yn=100$ and chromaticity coordinates $(x, y)_n$ = (0.44758, 0.40745).

$$u'_n = \frac{4x_n}{-2x_n+12y_n+3} \qquad [30]$$

$$v'_n = \frac{9y_n}{-2x_n+12y_n+3} \qquad [31]$$

$$u' = \frac{u^*}{13L^*} + u'_n \qquad [32]$$

$$v' = \frac{v^*}{13L^*} + v'_n \qquad [33]$$

This can be converted to the intermediate universal X, Y, Z colour coordinate system as follows

$$Y = \begin{cases} Y_n \cdot L^* \cdot \left(\frac{3}{29}\right)^3, & L^* \leq 8 \\ Y_n \cdot \left(\frac{L^*+16}{116}\right)^3, & L^* > 8 \end{cases} \qquad [34]$$

$$X = Y \cdot \frac{9u\prime}{4v\prime} \qquad [35]$$

$$Z = Y \cdot \frac{12-3u'-20v'}{4v'} \qquad [37]$$

In the next step a conversion was made to the more familiar 8-bit RGB system via the following transformation;

$$\begin{bmatrix} R \\ G \\ B \end{bmatrix} = \frac{1}{3400850} \begin{bmatrix} 8041697 & -3049000 & -1591847 \\ -1753003 & 4851000 & 301853 \\ 17697 & -49000 & 3432153 \end{bmatrix} \begin{bmatrix} X \\ Y \\ Z \end{bmatrix} \qquad [38]$$

Hue was calculated from RGB by the following;

$$H = \begin{cases} 60° \times \left(\frac{G'-B'}{\Delta} mod6\right), & Cmax = R' \\ 60° \times \left(\frac{B'-R'}{\Delta} + 2\right), & Cmax = G' \\ 60° \times \left(\frac{R'-G'}{\Delta} + 4\right), & Cmax = B' \end{cases} \qquad [39]$$

where the normalised values are;

$$R' = \frac{R}{255} \qquad [40]$$

$$G' = \frac{G}{255} \qquad [41]$$

$$B' = \frac{B}{255} \qquad [42]$$

and further support functions given by;

$$Cmax = \max\,(R', G', B') \qquad [43]$$

$$Cmin = min\,(R', G', B') \qquad [44]$$

$$\Delta = Cmax - Cmin \qquad [45]$$

Hue can then be normalised to a value between 0 and 1 by dividing by 360 °.

5.4 Results

The section contains the results of the pH/Hue sensitivity study. It is arranged into the following sections;

- Baseline Indicator,
- Indicator with IN varied,
- Indicator with BTB varied,
- Indicator with MR varied.

5.4.1 Baseline Indicator Analysis of pH/Hue:

The pH vs Hue function is defined (Figure 46) depending on the best available curve fitting function in MATLAB's curve fitting toolbox. A range of functions were used. The first function used was as follows

$$pH = aHue^{b} + cHue^{d} \qquad [46]$$

The values a, b, c and d are obtained by custom fit in MATLAB's curve fitting toolbox.

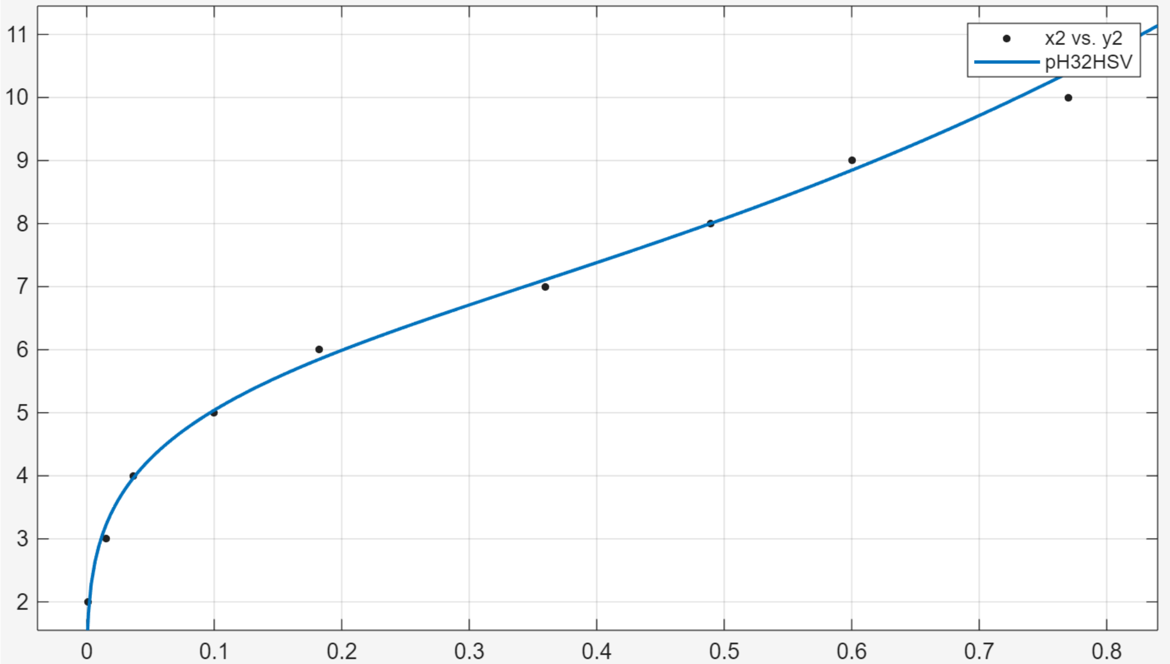

Figure 46 pH versus Hues as a double power law function

When spaced out on a HSV plot (Figure 47) from the top view (the location of circles indicates the position of each sample on Hue) the anticlockwise increase in Hue can be seen starting with the reddish pH 4.

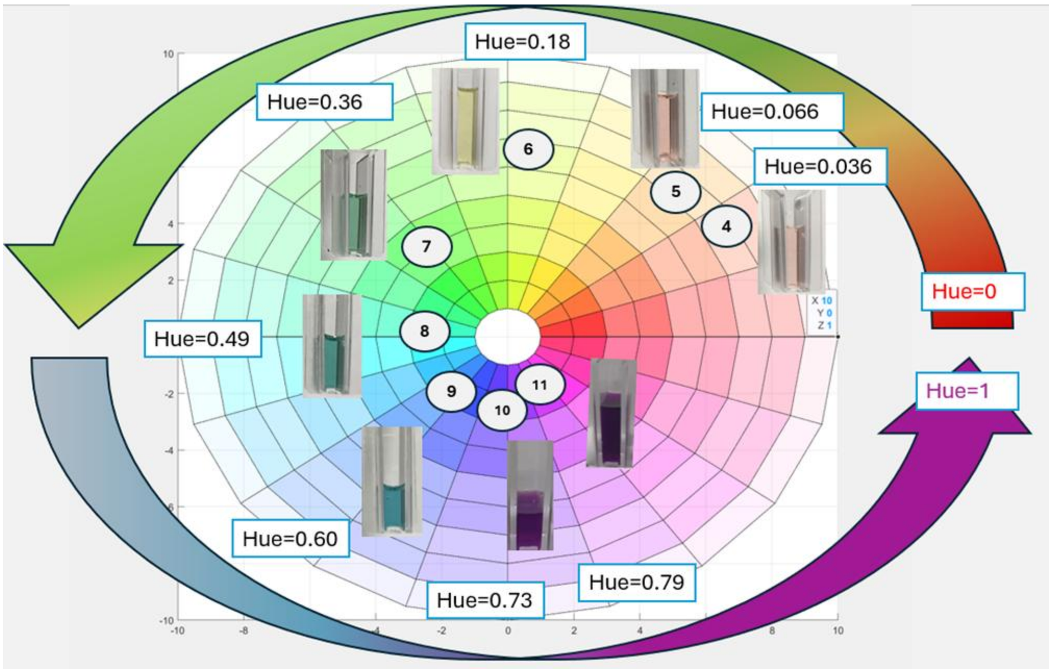

Figure 47 Hue values obtained through images

Figure 48 shows the comparison of two different concentrated dyes and their absorbance data from the sodium phosphate (SP) and phosphoric acid (PP) titrated solutions reveals that the UI dye exhibits a better absorption pattern at a ratio of 1:1:2 compared to 1:1:1.2 across the specified pH values.

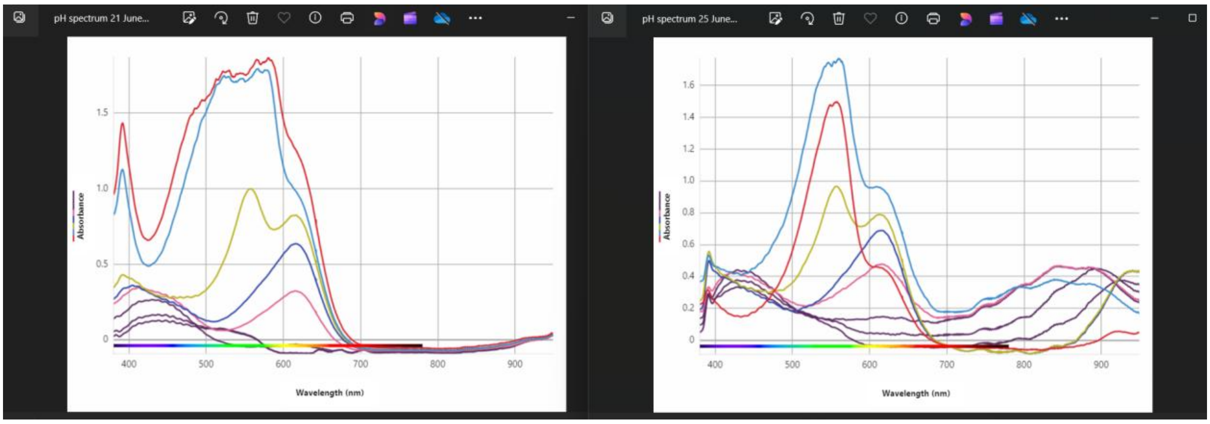

Figure 48 pH spectrum of SP and PP acid (Dye pH test1)

5.4.2 Results of Spectral Analysis to Colour Space Conversions Standard UI

The result values (Figure 49) from the absorption spectrum were exported from the spectrophotometer software. A prominent peak is observed in the wavelength region of 450 to 600 nm for pH levels 10 and 11, which corresponds to the blue, yellow, and green colour regions of the spectrum. At lower pH levels, significant absorbance is noted only within the 400 to 500 nm wavelength range. As the pH approaches neutral (around pH 7), the absorbance primarily consists of blue light (400 to 490 nm) and red light, resulting in a clear absence of green. Further decreases in pH lead to a shift in the spectrum from green to yellow and then to red, with major absorbance occurring in the violet and blue regions (400 to 490 nm). The correlation between physical colour and absorbance values has been validated using chart data.

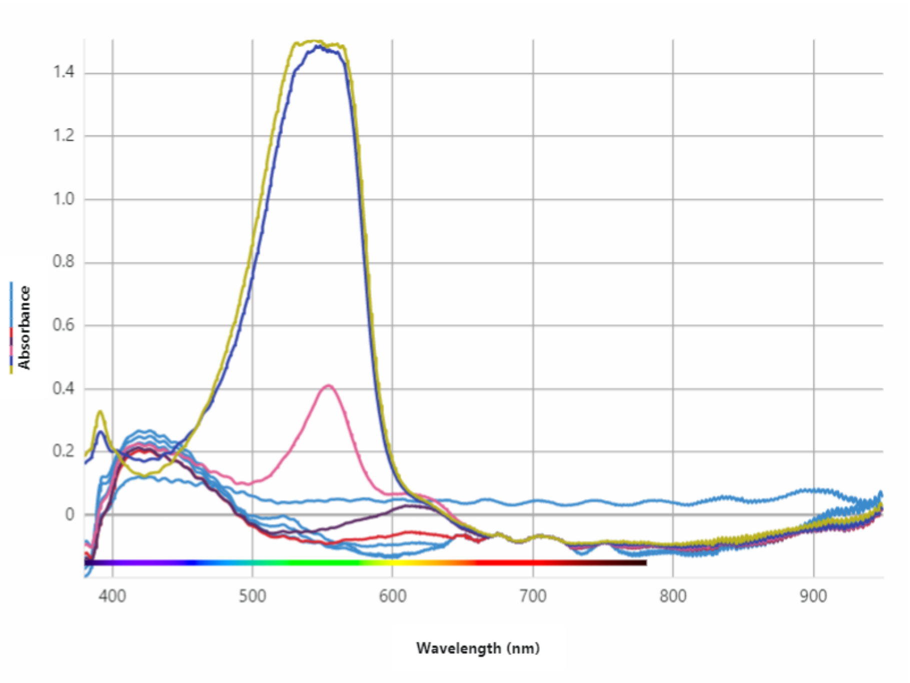

Figure 49 Standard UI dye spectrum

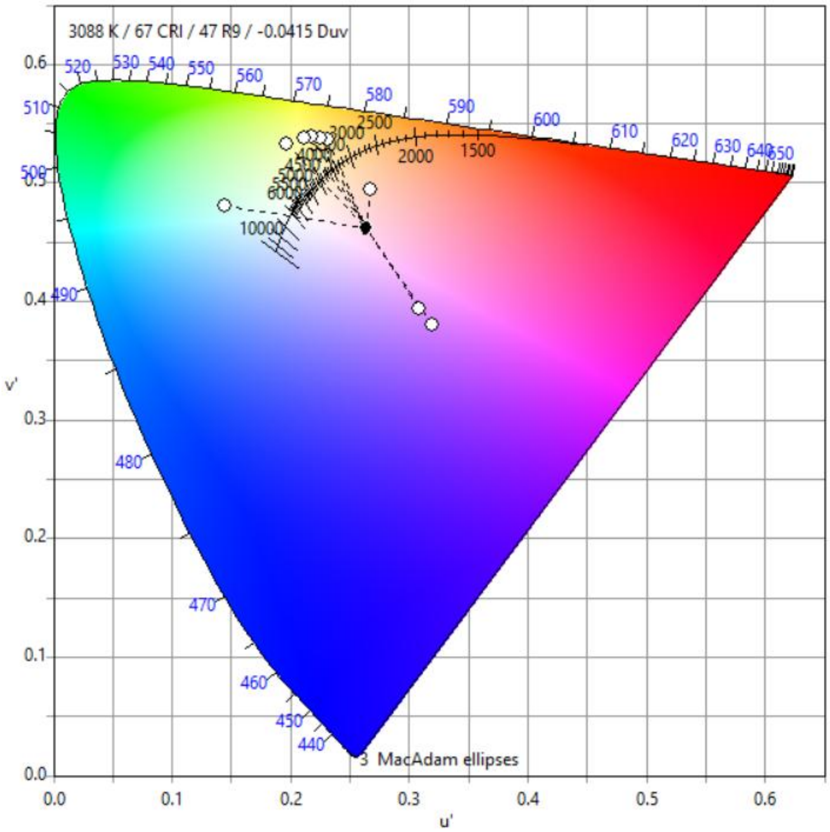

Figure 50 CIE diagram of standard UI dye spectrum

For UI dye Absorbance value for each pH plotted in OSRAM Colour Calculator, the CIE chart plotted as per Figure 50. In the CIE chart, pH values, 10 and 11 are representatively placed in the pinkish purple regions.

Table 10 L u’ v’ values and Hue values

UI Dye	**u' v’ Value**			**HSV value**		
pH value	**L**	**u'**	**v'**	**H**	**S**	**V**
3	100	0.265	0.495	0.0543	0.2542	254.937
4	100	0.232	0.537	0.1312	0.4213	254.8583
5	100	0.225	0.538	0.1401	0.4153	254.8491
6	100	0.217	0.5387	0.1499	0.4051	254.8304
7	100	0.211	0.537	0.1571	0.38	254.8207
8	100	0.196	0.532	0.1841	0.3248	254.8544
9	100	0.1445	0.4807	0.4512	0.1997	254.9691
10	100	0.308	0.3937	0.7781	0.4363	254.9898
11	100	0.3194	0.381	0.7772	0.4924	254.8904

UI Dye pH Vs Hue data trailed in MATLAB with the Gompertz function fit the pH vs Hue (Table 10) data the best.

$$pH = -1.08 + 11.569 * exp\ (-exp(-5.63(Hue + 1.2313))) \qquad [47]$$

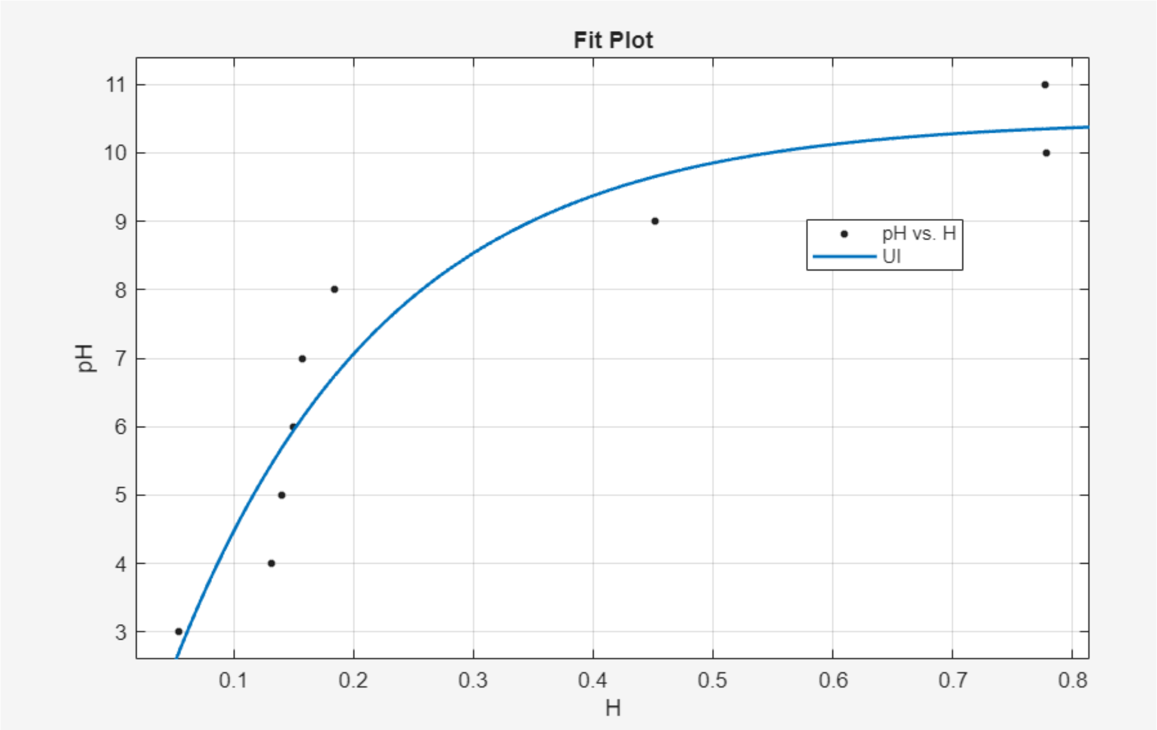

Figure 51 Hue vs pH curve fit for standard UI

The graph (Figure 51) illustrating the relationship between Hue and pH values, fitted with a Gompertz function, demonstrates that Hue increases as pH rises from 3 to 11. Beyond a pH of 10.5, the Hue values remain constant due to the phenolphthalein range, which shows a consistent hue above pH 10. Physical samples tested at pH values of 10, 11, and 11.4 exhibited similar colour patterns. In contrast, the variation in hue is significant from pH 3 to 9, with the colour patterns of the samples confirming the graph's findings. The absorbance spectra data at pH values above 10 were closely aligned with one another.

5.4.3 Results of Spectral Analysis to Colour Space Conversions IN alone and 25% IN in standard Dye

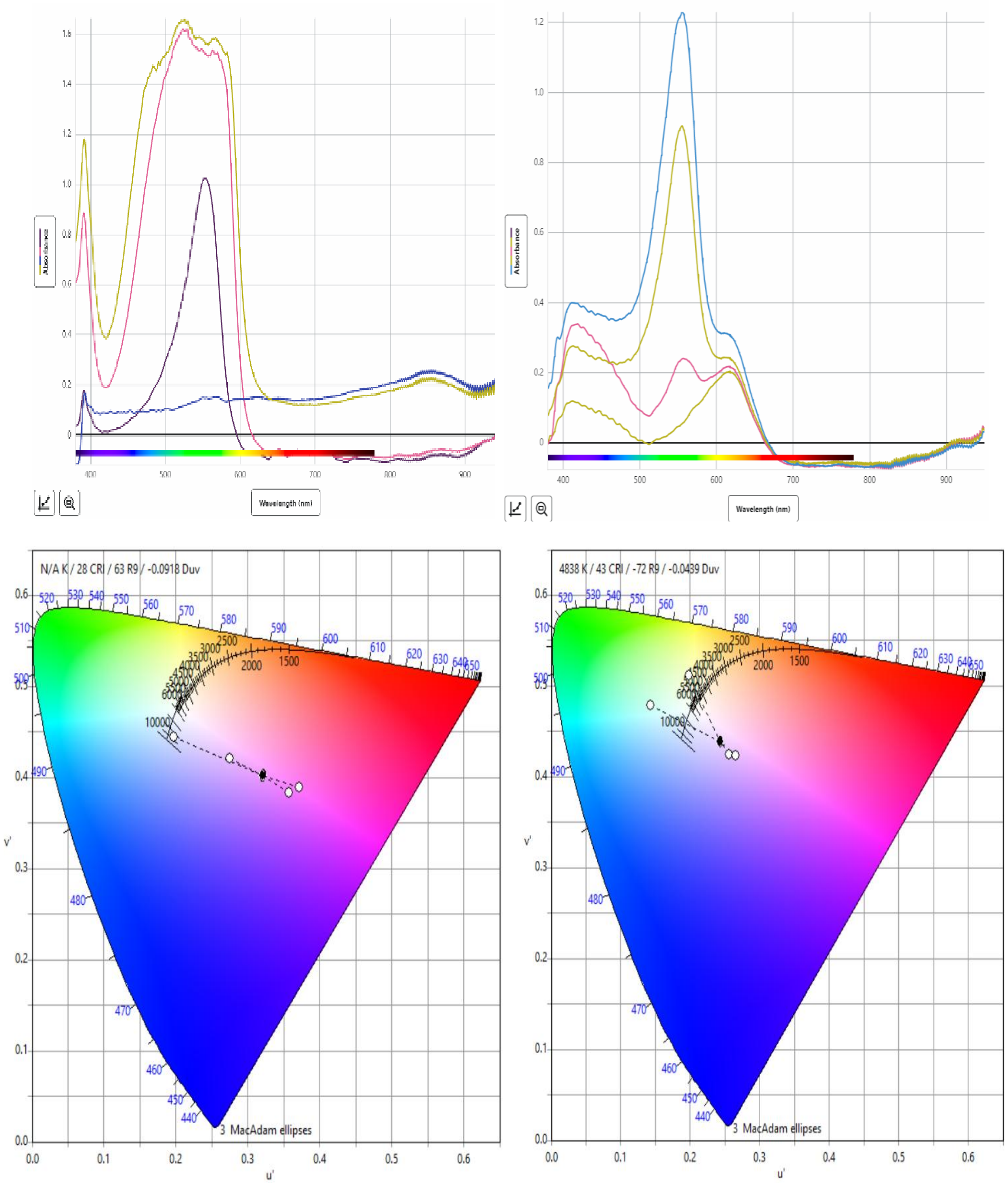

Figure 52 pH spectrum CIE chart comparison of phenolphthalein alone and 25% strength of phenolphthalein of standard UI dye

Phenolphthalein alone and a 25% reduced phenolphthalein in standard UI dye were selected for comparison. The absorption range extended up to 600 nm. The colour value points u’ and v’ on the chromaticity chart (Figure 52) shifted to the left, signifying a transition from reddish-purple to purplish-red. The standard UI dye illustrates the differences between standalone phenolphthalein and phenolphthalein mixed with BTB and MR. According to the chart, the hue variation was not significant between pH levels 9 and 11.

Table 11 L u’v’ values and Hue values of IN only Dye

IN alone	**u' v’ Value**			**HSV value**		
pH value	**L**	**u'**	**v'**	**H**	**S**	**V**
8	100	0.197	0.445	0.634	0.1581	254.97
9	100	0.2746	0.4207	0.7822	0.2808	254.977
10	100	0.357	0.3833	0.8148	0.5291	254.9845
11	100	0.371	0.3888	0.8387	0.5293	254.9628

Table 12 L u’v’ values and Hue values of IN25% in UI Dye

IN 25% of UI	**u' v’ Value**			**HSV value**		
pH value	**L**	**u'**	**v'**	**H**	**S**	**V**
8	100	0.143	0.478	0.4618	0.2036	254.8939
9	100	0.198	0.512	0.1907	0.1880	254.9162
10	100	0.2565	0.425	0.7566	0.2546	254.9758
11	100	0.265	0.421	0.7707	0.2682	254.9708

Table 11 L u’v’ values and Hue values of IN only Dye and, L u’v’ values and Hue values (Table 12) of IN25% in UI Dye, the comparison indicates the shift in Hue pattern when IN alone and IN strength reduce 25% from the standard UI dye. The saturation values at pH 10,11 were dropped in standard UI dye.

5.4.4 Results of Spectral Analysis to Colour Space Conversions 50% MR of standard UI

From the standard UI dye, 50% of Methyl Red dye is reduced from the dye formulation ratio to check the effects of absorption and colour values. Higher absorbance in the UV-vis spectrum (Figure 53) was observed at the lower pH range (pH values 3 to 6). Absorbance values for pH 10 and 11 were slightly higher at wavelength by 0.2 from the standard UI dye.

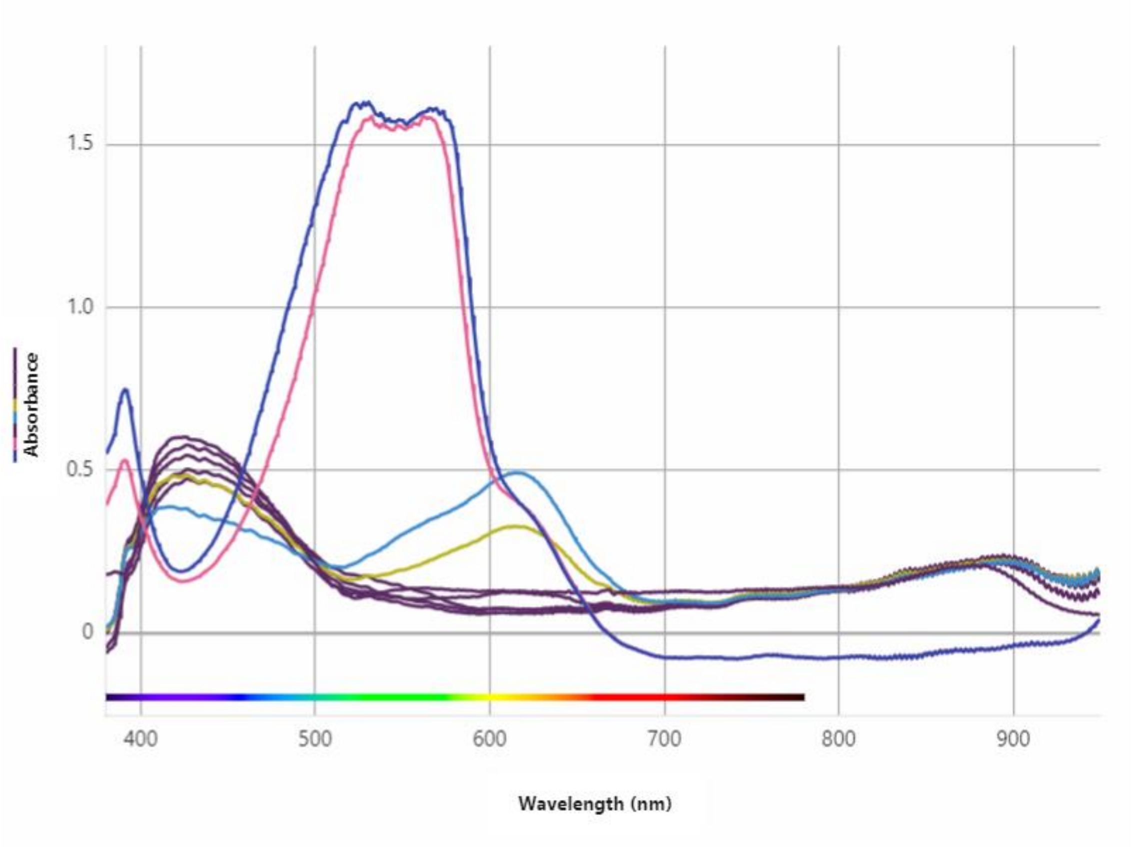

Figure 53 Mr 50% strength of standard UI dye spectrum

The chromaticity chart (Figure 54) there was no change in pH 9 compared to standard UI dye (0.45), The hue value remained almost the same at 0.46.

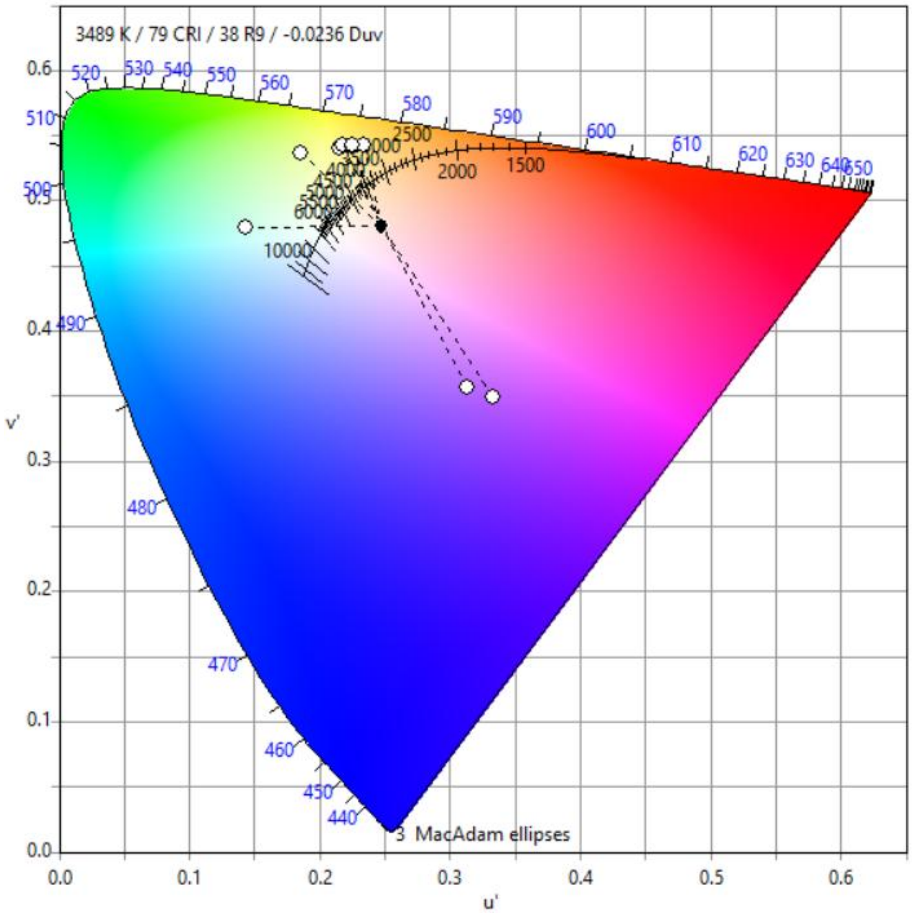

Figure 54 CIE diagram of MR 50% of standard UI dye spectrum

Table 13 L’u’v values and Hue values of MR50% in UI Dye

MR 50% of Dye	**u' v’ Value**			**HSV value**		
pH value	**L**	**u'**	**v'**	**H**	**S**	**V**
3	100	0.234	0.543	0.1388	0.4601	254.8258
4	100	0.227	0.543	0.1318	0.485	254.845
5	100	0.226	0.542	0.1384	0.4524	254.8424
6	100	0.217	0.543	0.149	0.4566	254.7963
7	100	0.215	0.541	0.1541	0.4194	254.8142
8	100	0.185	0.537	0.2047	0.3394	254.8492
9	100	0.148	0.478	0.4618	0.2103	254.9121
10	100	0.31	0.358	0.7496	0.5809	254.8162
11	100	0.333	0.348	0.7588	0.6264	254.8283

The following Gompertz function was trailed and fit the pH vs Hue data(Table 13) the best (Figure 55), Similar to BTB50% dye the hue value asymptotes after pH 10.5.

$$pH = -7.93 + 18.436 * exp\,(-exp(-6.12(Hue - 1.0472))) \qquad [48]$$

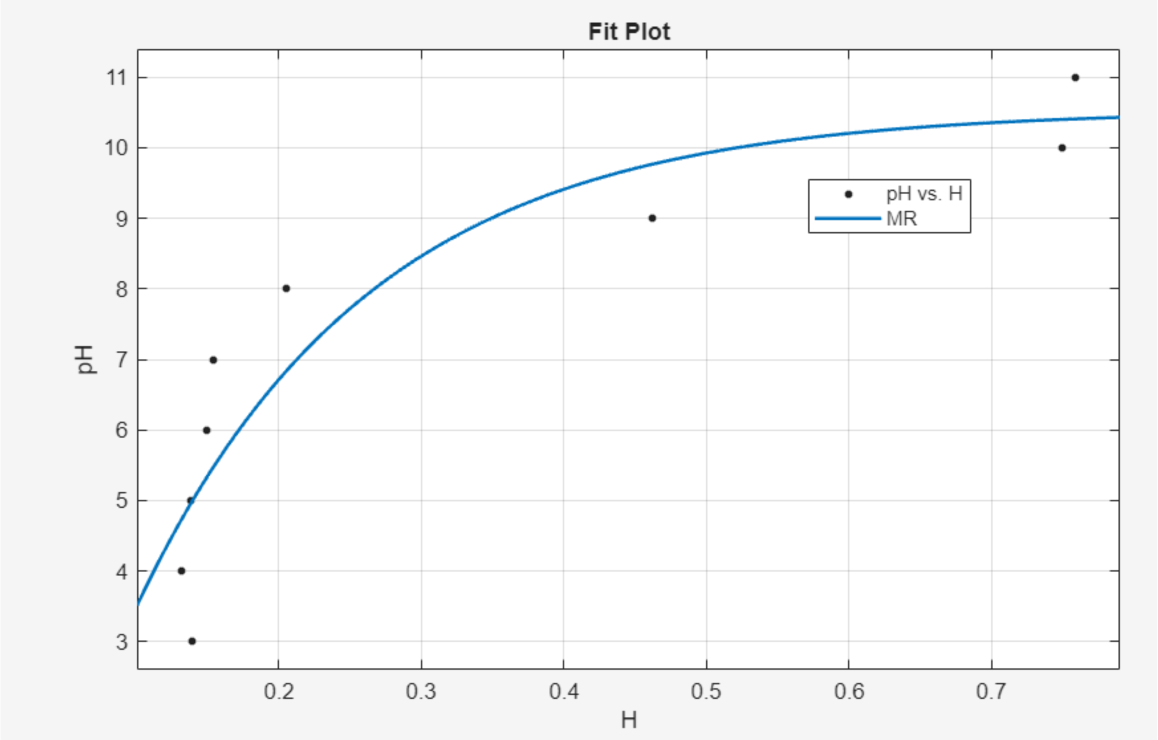

Figure 55 Hue Vs pH relation for MR50%

5.4.5 Results of Spectral Analysis to Colour Space Conversions 50% BTB of standard UI

The absorbance data were collected by spectrophotometer for the reduced BTB concentration in UI dye, Figure 56 Significance changes were observed in 400 to 500 nm spectrum range absorbance at lower pH values. When BTB was reduced, the absorbance value was reduced to approximately 0.25 in all lower pH values (pH 3 to 6) titrated liquid samples.

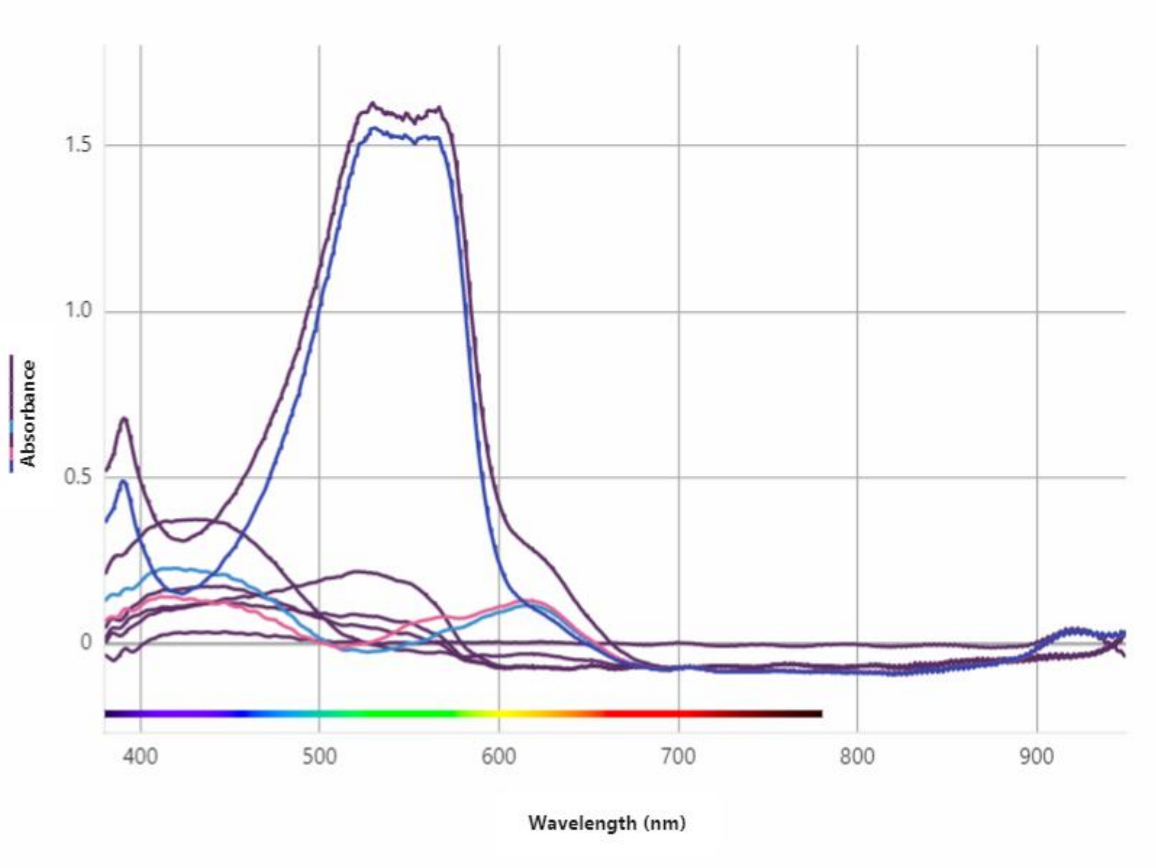

Figure 56 BTB 50% strength of standard UI dye spectrum

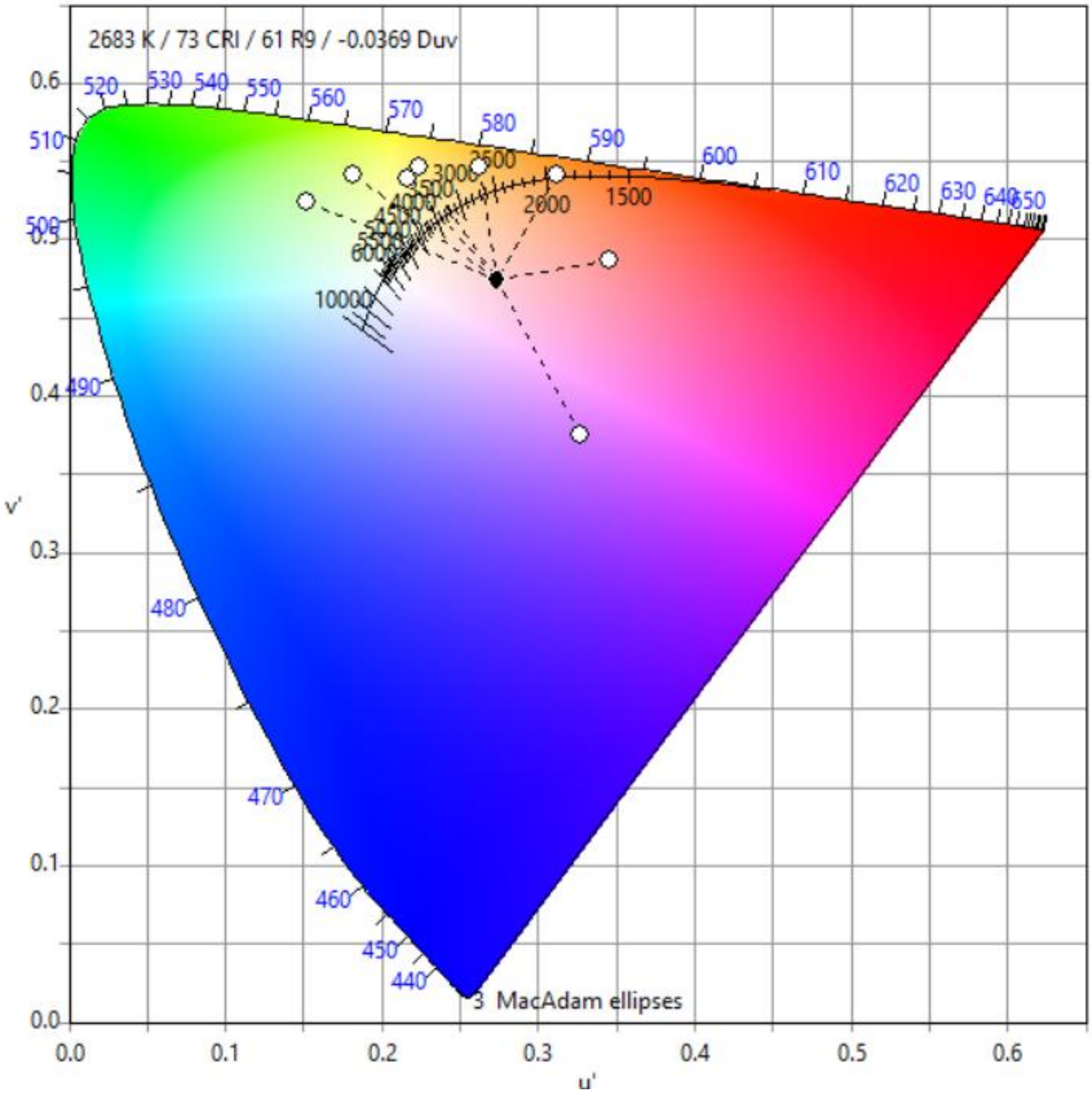

Figure 57 CIE diagram of BTB 50% of standard UI dye spectrum

Figure 57 illustrates the colour value shifting in the CIE chart Dye mixing ratio (MR) reduction to 50% from the standard UI dye. For the pH values of 9, 10, and 11, the colour values are evenly distributed in the CIE chart. The saturation value for pH 10 decreased from 0.58 to 0.46 in the BTB-reduced UI dye. Similarly, the saturation value for pH 11 shifted from 0.62 to 0.52. This demonstrates the effect of reducing the BTB. The low pH (4-6) comparison between MR50% and BTB 50% shows the shift in saturation value.

Table 14 L’u’v values and Hue values

BTB 50% of Dye	**u' v’ Value**			**HSV value**		
pH value	**L**	**u'**	**v'**	**H**	**S**	**V**
3	100	0.345	0.487	0.0054	0.4232	254.93
4	100	0.312	0.542	0.0788	0.7278	254.8573
5	100	0.262	0.546	0.1104	0.6288	254.8256
6	100	0.224	0.547	0.1439	0.5113	254.8216
7	100	0.216	0.54	0.1524	0.4039	254.8373
8	100	0.182	0.542	0.2038	0.4052	254.8261
9	100	0.152	0.524	0.2781	0.3038	254.8618
10	100	0.312	0.387	0.7769	0.4609	254.9974
11	100	0.327	0.375	0.777	0.5278	254.7859

The following Gompertz function was trailed and fit the pH vs hue data from Table 14 the best plotted in Figure 58. The hue value becomes a horizontal asymptote above a pH level of 10, and thus, the curve fit is only valid in the range of pH 3-10.

$$pH = 2.8236 + 7.6164 * exp\ (-exp(-11.9598(Hue - 0.1262))) \qquad [49]$$

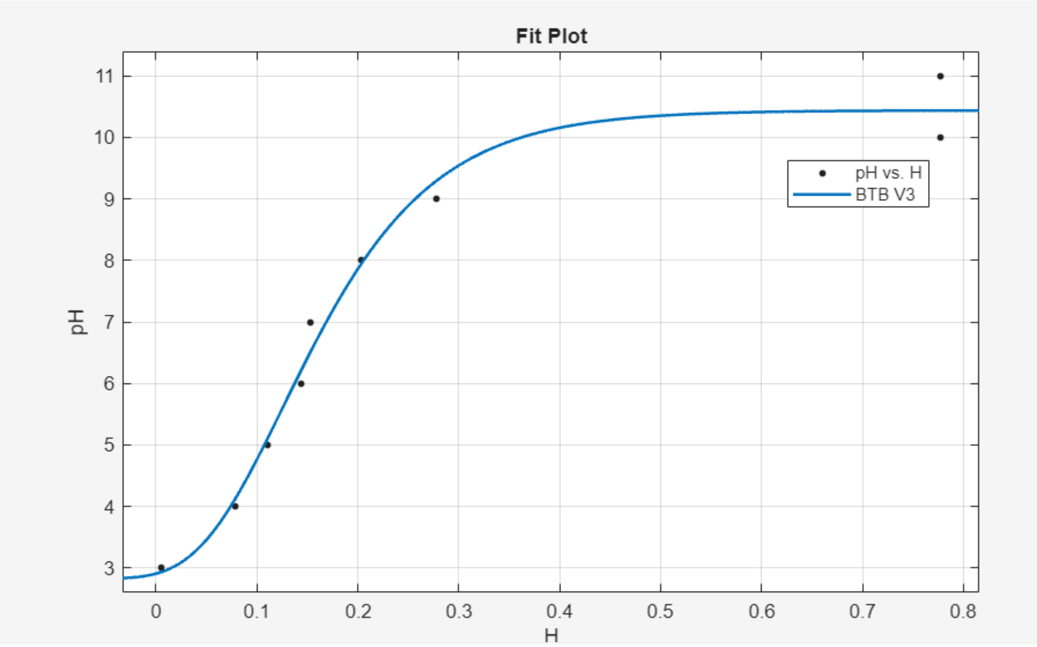

Figure 58 Hue vs pH relation MR 50%

5.4.5.1 Dye Stability Test

The dye stability test was conducted in an activated carbon microreactor CDI system, and the dye concentration was found to be slightly diluted, but the hue remained the same. In a comparison of 2 different microreactors as per Figure 59, the dye stability for 100 seconds was analysed and found the same hue. The dye seems to be effective for the expected test period. It was possible that in the liquid coated membrane that some residual demineralised water desorbed from the carbon and entered the reactor

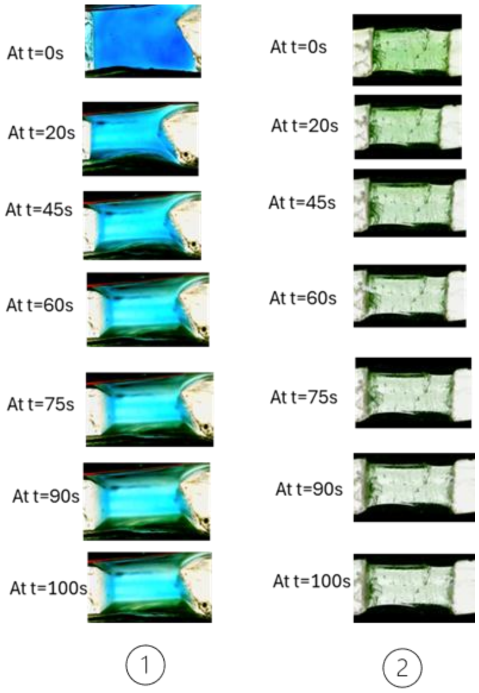

Figure 59 Dye stability test for 100s 1. Microreactor with sheet membrane, 2. Microreactor with liquid coated membrane in both test Hue remained same although in image 2 the brightness reduced

5.5 Discussion

The pH/Hue sensitivity study results in different opinions on how each combination affects the HSV value. It started with In Indicator alone and with a reduced 25% from the standard UI dye, which serves as the control to illustrate the indicator's standard response under normal conditions. The study then further details how different combinations of factors influence the indicator’s performance. Similarly, the "Indicator with BTB Varied" section explores how modifications to Bp affect the indicator's sensitivity, while the "Indicator with MR Varied" section examines the influence of changing MR on the indicator's response. The mathematical correlation sigmoidal function was tried to fit with pH vs Hue. Figures 51,55,58 show the UI dye and the dilution dyes vs Hue correlation with the Gompertz function. Finally, the dye stability test showed promising stability over a period of 100 seconds in the microreactor system. The summary of the tests conducted by varying In, BTB, and MR are tabulated in Table 15, the UI dye’s stability for the pH range 4-11 is shown.

Table 15 pH and respective Hue values for Dye experiment

pH	**3**	**4**	**5**	**6**	**7**	**8**	**9**	**10**	**11**
UI Dye-Hue	0.0543	0.1312	0.1401	0.1499	0.1571	0.1841	0.4512	0.7781	0.7772
BTB 50%	0.0054	0.0788	0.1104	0.1439	0.1524	0.2038	0.2781	0.7769	0.777
Mr 50%	0.1388	0.1318	0.1384	0.149	0.1541	0.2047	0.4618	0.7496	0.7588
IN 25%						0.4618	0.1907	0.7566	0.7707
IN alone						0.6315	0.634	0.7822	0.8148

5.6 Conclusion

This chapter has successfully developed a framework to assess the sensitivity of dye by establishing the pH-hue correlation and verifying the relationship by altering the components of UI dye. There is a clear understanding of how variation in IN, BTB, and MR affects the hue values in the overall pH distribution as detected by the colour imaging system. Chapter 4 provided a technical basis for characterising the indicator system under varying compositional conditions. The dye stability test revealed a key sensitivity of dye concerning adsorption and potential electrosorption of dye into activated carbon. Although the 100-second stability of the dye seemed suitable for further experiments, the sensitivity findings suggest further investigation and adjustments to the dye composition to mitigate the sensitivities and improve the performance of DOTH.

6 Chapter - New Method for Observation of Proton Concentration in EC Stack

6.1 Introduction

This chapter explains about the development of microreactor system and continuous monitoring system. Microfluidics system enables us to see the reaction across and experiment the different combinations of membrane with carbon. The expected reactions in CDI and mCDI units resemble this miniature reactor system arranged a micro vise structure. This was made possible using microfluidics reactor system and micro vise support structure.

6.2 Methodology

6.2.1 Optical Imaging Device with Linear Stage.

The optical image sensor is an ISM-PM200S CMOS sensor with optics comprised of a 21mm lens or 19mm lens configuration. These were wide-angle (8.1mm x 6.4mm field of view) and close-in (1.8mm by 1.5mm) configurations.

CNC 3018 high precision gantry system is used as for image observation and recording device in the experiment. The microscope camera is held in the gantry by the custom 3D printed holder and secured.

The imaging device was affixed (Figure 60) to the three-dimensional linear stage with the ability to move in the x and y direction in 10μm steps. Image focus was achieved by raising and lowering the z position of the stage in 10μm increments. The linear stage affixed the camera at the gantry by way of a custom bracket shaped to the contour of the camera.

Under the identical lighting conditions, we obtain the following relationship between Hue (as recorded by our optical image sensor) and pH as recorded by the AKTA pH sensor as shown below.

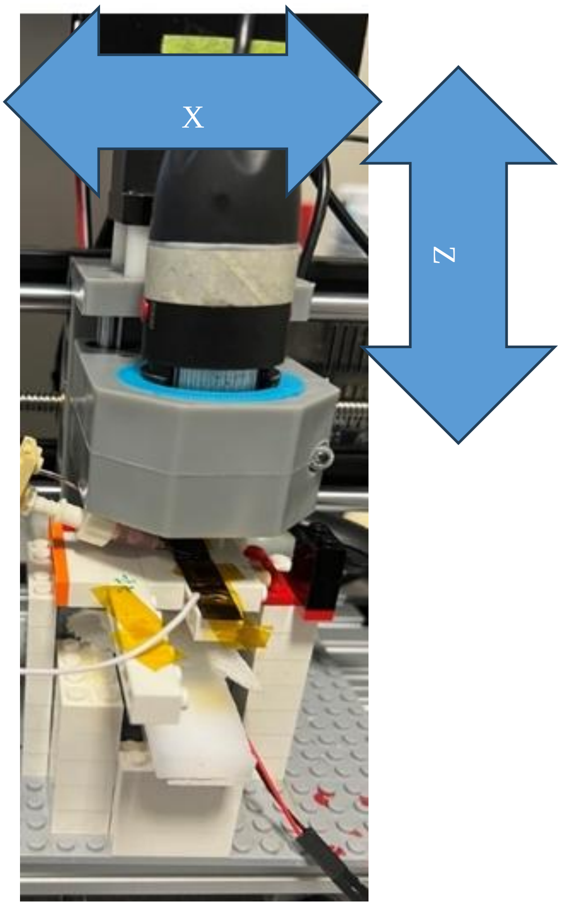

Figure 60 The 3018 gantry system with the camera added could move in the X/Y/Z plane in 10µm steps. As the microreactor was in a single plane with the full reactor in the frame, movements in the X and Z directions were only required.

6.2.2 Image Analysis in MATLAB

In pH spectrum image analysis, the following steps were followed to analyse the reactor image in the MATLAB

- Data conversion from Vernier spectral analysis program to Colour Calculator:

From the Vernier UV-Vis spectral analysis program, absorbance data was collected and exported into a CSV file format. pH absorbance value converted to transmittance value in Excel. The Transmittance curve is the inverted form of the absorbance curve. Wavelength vs absorbance values 360 to 830 nm visible spectrum region, and the 2-column data exported to notepad text format. Further, the *.txt file was imported into the colour calculator app, and colour values were calculated.

- Colour data from colour calculator to MATLAB:

From the colour calculator app, the spectra analysis was done, and the colour snip shot from the CIE chart was taken and imported into a MATLAB image file;

- Image selection and conversion into MATLAB analysis. Appendix 9.6.1,
- The choice of the interested cross-section channel in the reactor is selected. As per MATLAB code reference Appendix 9.6.2,
- RGB plots of the interested reactor column are plotted. Appendix 9.6.3,
- RGB Reference data file. Appendix 9.6.4,
- Conversion of RGB to Hue Saturation Value data and creating a polar plot. Appendix 9.6.5,
- The pH variation across the reactor is plotted in a graph Appendix 9.6.6.

6.2.3 Micro Reactor

6.2.3.1 Design of Microreactor

The basic design of this system consists of a transparent acrylic reactor centre microfluidic region, Activated carbon electrodes and steel base plates; this section is observed continuously with a camera fixed on a gantry which can travel along the x,y, and z axis of the microreactor region with adjusted focus length.

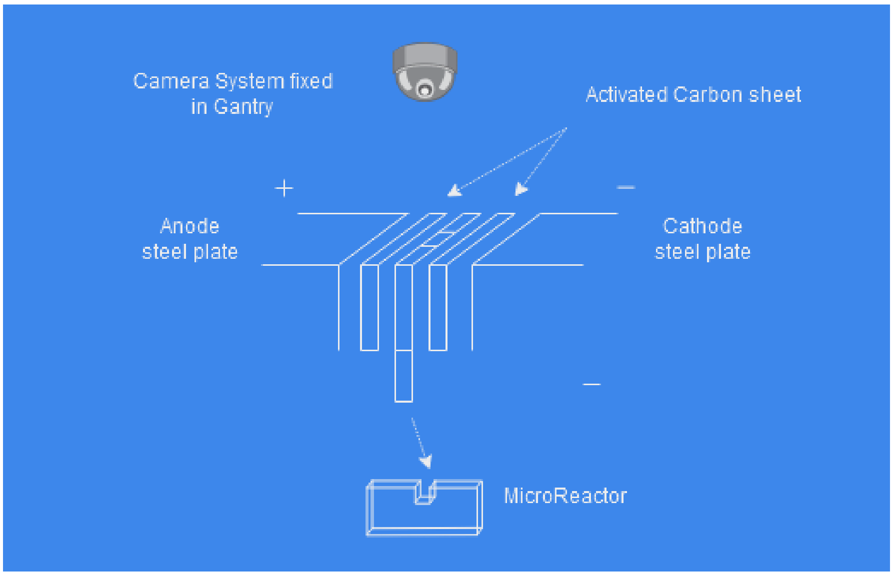

Figure 61 Micro reactor set-up

6.2.4 Carbon Electrode Preparation

A carbon sheet electrode was implemented in the microreactor cell, serving as both the anode and cathode, thereby replicating the functions of CDI electrodes (Figure 61). High-precision sharp edges were achieved through the laser cutting method. Alternatively, electrode sheets with sharp edges were produced using a scalpel. Throughout the preparation process, care was taken to ensure that the electrode sheets remained free of contaminants that could impair their performance. Oil and dust are known to adversely affect the efficiency of sheet electrodes.

6.2.5 Carbon Electrode Membrane Application

All different concentrations of membrane coatings were prepared in the laboratory for these experiments. Carbon sheets measuring 33 mm x 9.4 mm (each weighing 0.037 g) were used for the membrane application. A separate micropipette was employed to measure the AEX/CEX/DMSO (Dimethyl sulfoxide) chemicals.

The membrane was diluted using DMSO (volume %). For instance, to create a 25% dilution, 12.5 µL of the AEX/CEX membrane was mixed with 87.5 µL of DMSO in a petri dish, ensuring thorough mixing with a glass rod. The diluted membrane solution was then drawn into a micropipette and applied uniformly over the entire surface of the carbon sheet.

A laser-cut carbon sheet was placed on a glass plate (Hoefer) positioned above wax paper (Figure 62). The wax paper was kept flat without any creases to prevent the carbon from sticking tendency to the glass plate during the curing process. In the earlier stages, challenges such as the curling tendency of the carbon electrodes and sticking of the electrode sheets to the glass plates without the wax paper were encountered. To address this, the top edge of the electrode sheet was secured using Kapton tape, and the liquid membrane was applied uniformly over its surface. The glass plate base was slightly tilted at an angle of approximately 30 degrees to facilitate the even spreading of the membrane. The application began from the top (the side where the Kapton tape was fixed) and proceeded toward the bottom.

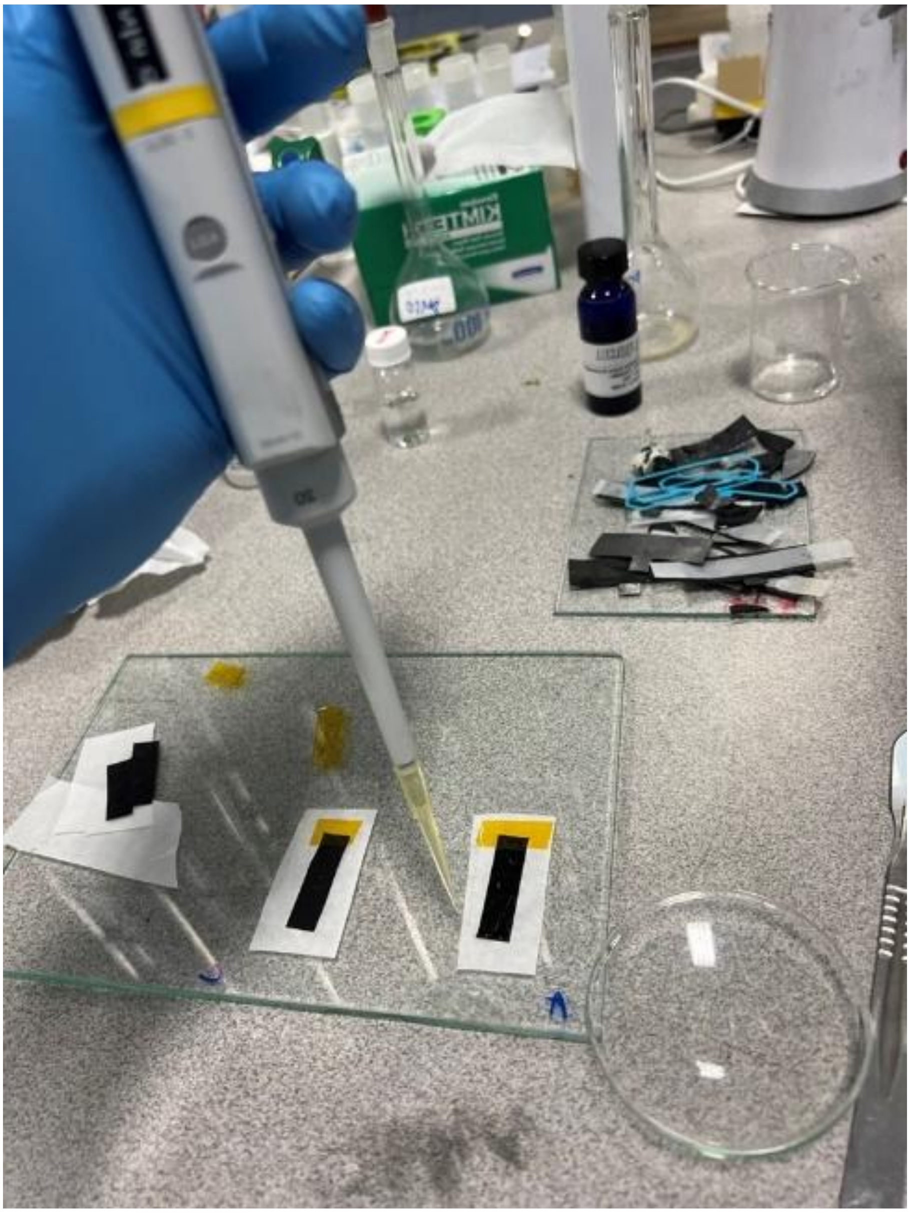

Figure 62 Membrane application on AC electrode (Reactor)

6.2.6 Membrane Curing

Membrane-coated AC sheets with the glass plate were left in a lab atmosphere (humidity < 30%) to dry for 8 hours, and then they were kept in a low vacuum for an additional 6 hours.

6.2.7 Electrode Base Plates

To supply power to the microreactor electrode, steel plates were employed as the primary contact from the power supply unit. These plates were carefully measured and cut to fit the micro vise clamps. A thin sheet measuring 0.1 mm was chosen for its malleability, allowing it to conform to the reactor slot. After cutting the sheet with scissors, it was bent at a 90-degree angle using the vise and left to sit for several hours to maintain a sharp edge. This procedure ensured that the edge was precise for the microreactor. The scissors used were platinum-coated and designed for high-precision cutting. The direct cut and bend method was implemented to create a finely edged steel base for the reactor. When inserting the bent steel base plates, the shorter edge at the L bend was placed into the reactor slot. The sharpness of the L bend was then verified using a microscope camera. If the sharp edge is not achieved, the steel base plate should either remain in the vise for additional time or be replaced with a fresh piece of steel to recreate the edge. Failure to obtain a sharp edge at the reactor slot could result in the accumulation of reactor solution beneath the steel plate, leading to undesirable outcomes.

6.3 Experiment

6.3.1 Reactor Design

6.3.1.1 Acrylic Reactor Base Section

The direct cut method was employed using titanium-coated scissors, followed by cutting the microreactor slot to a depth of 1.5 mm with a CNC machine using an end milling bit. A piece measuring 9.4 mm in width and 15 mm in height, matching the dimensions of the microreactor slot, was prepared. A scalpel equipped with a micro-USB camera was used to clean the internal section of the microreactor slot. An acrylic sheet was used because it is transparent, allowing for observation of the reaction across the reactor's cross-section.

6.3.1.2 Carbon Sheet

Three different sets of carbon were used in this experiment as electrodes.

1. Activated carbon sheet from a CDI module,
2. Graphite sheet,
3. Membrane-coated activated carbon sheet.

6.3.1.3 Assembly Procedure

Anode and cathode-side electrode sheets, made of AC or graphite, are positioned on both sides of acrylic plates. The lower section of the electrode, extending 50% below the acrylic plate, was secured on both sides using Kapton tape. The top section of the acrylic sheet is aligned with the AC/graphite sheets.

6.3.2 Fluid Delivery System

The syringe was set up on a micromanipulator platform, featuring a 60x60 mm V-type trimming system with four axes. An acid-resistant silicone tube (4.8mm) was custom fitted with a holder positioned near the reactor, ensuring that the needlepoint was aligned straight and in close proximity to the reactor. A 34G needle was selected for the precise delivery of dye over the reactor slot. By applying pressure to the silicone tube, a fine droplet was delivered accurately onto the top of the reactor cell.

6.3.3 Micro Reactor Testing Procedure

This section outlines the procedure for testing electrical connections to the electrode, assembling the microreactor, levelling and voltage testing, preparing chemicals, and setting up the microreactor with backlighting.

6.3.3.1 Prerequisite

Thorough testing of the electrical connections to the electrode was performed. The complete assembly of the microreactor, as outlined in the Reactor Assembly section, was finalized. Levelling and voltage testing at the steel base of the electrode were conducted.

6.3.3.2 Preparation of Reagents

The procedure involved two main components. The first component was a standard dye, while the second was a titrated solution of Sodium Phosphate (SP) and Phosphoric Acid (PA) with adequate ionic strength. The preparation of the universal indicator dye was conducted as detailed in section 4.6. The titration solution was prepared using an acid-base titration method. A saturated solution of Sodium Phosphate was placed in a Polyethylene (PE) container reservoir, similar to the setup used for the VIS spectrophotometer experiment, as described earlier, excluding the spectrophotometer flow cell. This setup was employed to circulate the solution and achieve the desired pH, specifically targeting a pH of 7 for the experiment. Initially, the reservoir was filled with the Sodium Phosphate solution. After circulating the base solution for 5 minutes, the pH sensor (AKTA) indicated a reading of approximately 11.3. At this point, Phosphoric Acid (5% weight/volume) was introduced into the reservoir. The acid was gradually added until the pH reached and stabilised at 7 for 5 minutes. The titrated solution (SP+PA) was then drawn into a 5 ml syringe fitted with a 22G needle. The universal indicator dye was transferred into a 1 ml syringe using a 34G needle, or a 30G needle if the 34G syringe experienced back pressure or frequent blockages.

6.3.3.3 Loading the Reactor

Carbon electrodes for the respective test were securely positioned in the clamping section of the micro vice. Appropriate torque was applied using the torque mechanism to ensure the reactor's stability. This step is crucial for maintaining good conductivity between the electrode sheet and the base steel plate. The top side must be flush with the reactor electrode level. To prevent the bowing of the carbon sheet, a Teflon insert was placed between the electrode sheet and the reactor region. The electrode wires were fastened with Kapton tape to the structure to prevent disconnection during gantry movement.

The assembled microreactor was positioned on the gantry system base, with the microreactor located above the backlight setup. The resistance of the electrode assembly was checked with a multimeter and found to have an open contact.

6.3.3.4 Reactor Backlighting Setup

The backlighting arrangement was crucial in the microreactor setup. The Jaycar LED Array Type ZD0657 (4400K) backlighting for the microreactor was set up with an acrylic sheet light diffuser arrangement and applied proper voltage (5-10V) was with the power control unit to achieve optimum brightness. The colour of the pH 7 solution was verified after assembly with the backlight intensity adjustment by varying the voltage.

6.3.3.5 Reactor Priming and Starting

The CDI cells of the microreactor electrodes were kept in a shunt condition, which means that the anode and cathode electrode wires were shorted together. The Teflon insert, used to prevent bowing, was removed. Video capture in the system was initiated, and a titrated solution was drawn into a 5 ml syringe. This solution was added carefully to avoid damaging the electrode sheet in the reactor. Proper wetting was confirmed by adjusting the microscope camera to observe the edge of the reactor. Once the priming was deemed satisfactory, the power supply unit was energised while keeping the foot pedal switch in the "Off" position. This step ensured the power supply was ready for when the titrated solution was introduced into the reactor. The titrated solution was then added dropwise using the fluid delivery system in the microreactor section. Following this, 1-2 drops of dye were delivered into reactor slot 1 using a 1 ml syringe. A few seconds were allowed for mixing to observe a uniform pH 7 colour (cyan). Upon confirming the expected pH 7 colour in the reactor, the foot pedal switch was released to apply power to the electrodes. Observations were recorded as a video file. Occasionally, the upper meniscus of the liquid dropped into the reactor, causing an artifact effect. Adjustments to the camera focus could be made to correct any artifacts observed. Polarity switching of the electrode power supply was performed using the CDI H-bridge toggle switch. This was done to observe the reverse electrode effect within the microreactor and to desorb the adsorbed sodium and phosphate ions from the activated carbon sheets.

6.3.3.6 Reactor Interchange Procedure

System shutdown steps followed as, power off the gantry, power off the lighting. Next stage Gantry unit candle software command was used to move the reactor assembly out of the camera focus section. The reactor assembly was pulled out from the stack locking mechanism, by loosening the grub screw. The spent microreactor was removed using tweezers; the reactor slot and steel plates were cleaned with IPA (Isopropyl alcohol) until no residual dye was present. Following the drying of the reactor slot, the new reactor setup with different AC/membrane arrangements was set in for testing and torqued using the torque mechanism. The procedure is repeated from the priming stage.

6.3.4 Membrane Application

The membrane application in the activated carbon step was to test the actual Faradaic reaction in the CDI system. The Faradaic reaction effects mentioned in Section 2.4.7 were significant in CDI. Unlike CDI, in the mCDI, the faradaic reactions are limited due to the presence of a membrane.

In our experimental study, we conducted three distinct sets of membrane applications. The first set utilized membranes applied directly onto graphite surfaces, while the second set involved membranes integrated with activated carbon sheets. Additionally, we explored various concentrations of membranes on activated carbon to assess their performance under different conditions. This comprehensive approach allowed us to examine the interactions and effectiveness of the membranes across different substrates.

The SEM images were analysed following the application of the membrane coating on activated carbon (AC). A uniform coating was observed, with the liquid membrane diluted to a concentration of 12.5% on both the carbon surface and the inner layer. The macro pores of the AC were examined to assess the depth of the membrane application within the layer. At the points of breakage, the sublayers of the membrane materials were clearly visible, demonstrating the protrusion of the polymer membrane through the pores of the activated carbon electrode. The SEM analysis revealed an approximate coating thickness of 1 to 3 microns for both cation-exchange (CEX) and anion-exchange (AEX) membranes on the AC electrode 9.6.

6.4 Experiment Observations (from Videos)

6.4.1 Activated Carbon with Membrane Sheet

In this reactor, we observed a top-down view of the microreactor's conditions as the electrochemical reaction occurred with some minor distortion noted due to the meniscus (Figure 63). The design of this reactor closely resembled that of a real-life mCDI (Membrane Capacitive Deionization) unit, though it incorporated various membrane configurations that differed from standard designs. The reactor assembly consisted of two layers of FumaSep membrane sheets—anion exchange (AEX) and cation exchange (CEX)—which are crucial for facilitating ion selectivity during the mCDI reaction process. This configuration effectively replicated the characteristics of mCDI, ensuring that it provided a robust simulation of real-world applications.

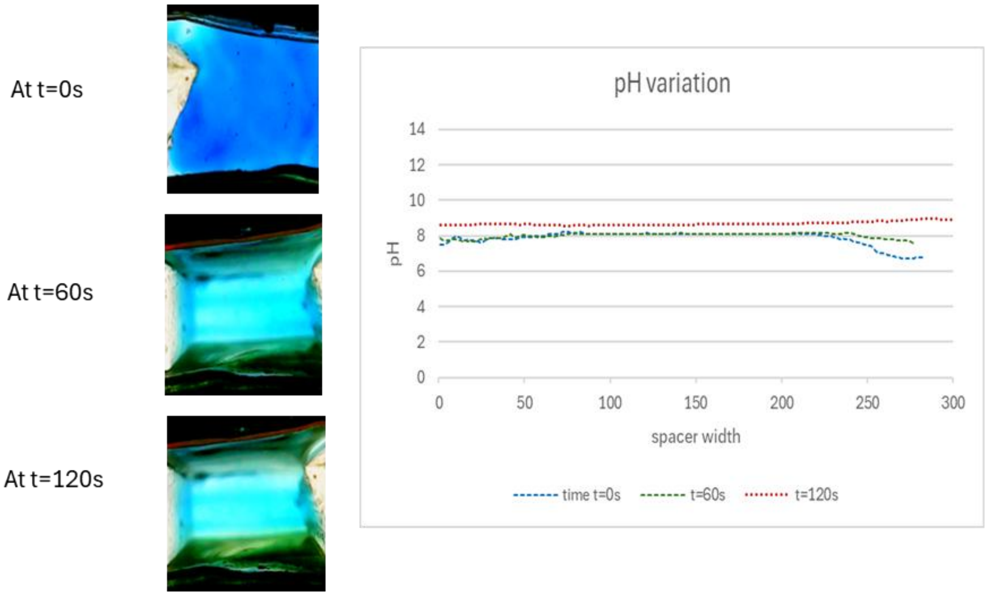

Figure 63 Microreactor top view (with AEX/CEX membrane) at different timings and pH variation chart across the reactor cross-section view from the top. Reactor Size:1 mm

In this microreactor experiment, double-sheet membranes were used. 2.0 V potential difference was applied across the electrode. At three different time intervals, Video snapshots were analysed. Initially, at t=0s, the pH was 7.46, and it was consistent across the reactor spacer width. At t=60s, the pH was 7.8, and at t=120s, it was 8.62. The dye colour pattern Figure 63 were similar in all three different timings throughout the reactor spacer with no chemical reaction observed in the reactor during the experiment. The pH levels between the electrodes remained stable, showing no significant changes. The absence of a Faradaic reaction indicates that the double membrane arrangement used in the reactor was effective in preventing electrochemical reactions, which are typically responsible for changes in pH and the generation of current. Overall, the results confirmed that the chosen configuration did not facilitate any electrochemical reactions.

6.4.2 12.5% Liquid Membrane Coated AC

The observations below result from various membrane configurations. This is the lowest membrane coating tested in the microreactor. The coating efficiency of this membrane was analysed effectively. The SEM images confirmed the coating efficiency as expected

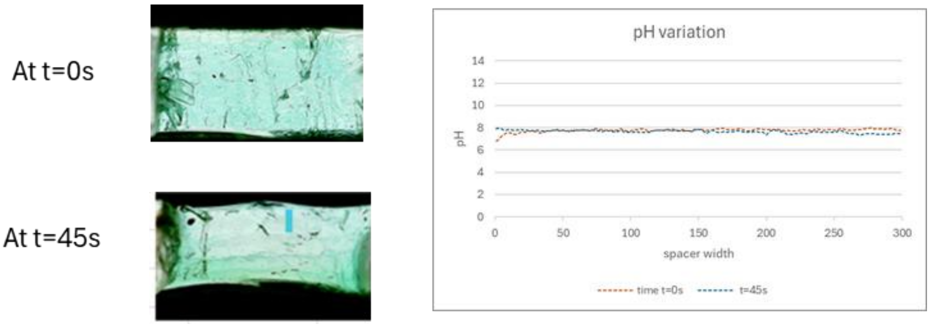

Figure 64 12.5% liquid membrane-coated reactor and pH variation. Reactor Size:1 mm

A 2.0 V potential difference was applied across the electrode. A liquid membrane-coated electrode sheet with a concentration of 12.5% was used in this microreactor. Video snapshots were analysed at two different time points. Initially, at *t=0s*, the pH was 6.76 and it was consistent across the reactor spacer width. At *t=45s*, the pH was 7.9. The dye colour Figure 64 the pattern was consistent across the two different timings throughout the reactor spacer width. This behaviour resembled that of the sheet membrane; no significant pH change indicated no Faradaic reaction occurred.

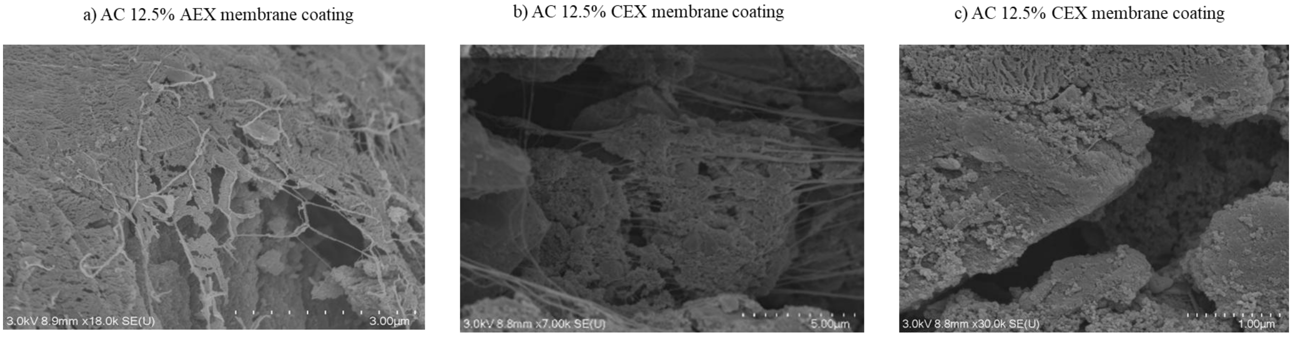
a) AC 12.5% AEX membrane coating

b) AC 12.5% CEX membrane coating

c) AC 12.5% CEX membrane coating

Figure 65 SEM images of activated carbon sheet with 12.5% membrane coating

The SEM images in Figure 65 confirm the coating efficiency of the liquid membrane applied on the AC electrode sheet.

6.4.3 25% Liquid Membrane Coated AC

The following observations represent the change in pH rate of the microreactor with a 25% diluted liquid membrane coating.

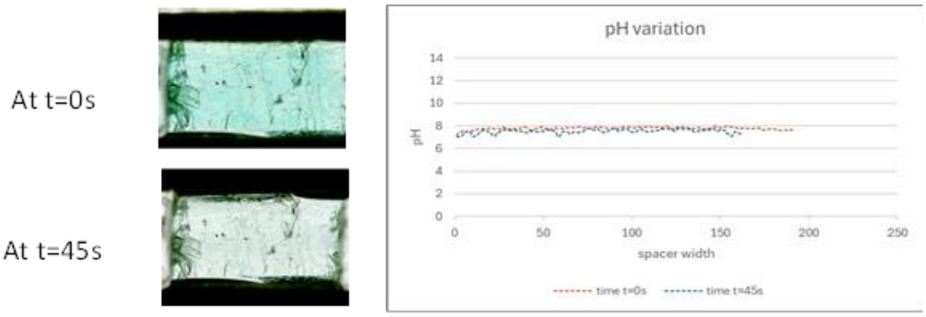

Figure 66 25% liquid membrane-coated reactor snapshot and pH variation. Reactor Size:1 mm

This experiment used microreactors with 25% concentration Liquid membrane-coated electrode sheets. Video snapshots were analysed at two different time intervals. Initially, at t=0s, the pH was 7.15, and it was consistent across the reactor spacer width. At t=45s, the pH was 7.04. The dye colour pattern Figure 66 was consistent across two different timings throughout the reactor spacer width. This behaviour was similar to that of a sheet membrane; there was no significant change in pH, and it was concluded that no Faradaic reaction occurred.

6.4.4 50% Liquid Membrane Coated AC

The activated carbon with a 50% concentration was selected to compare the reaction rate at the next concentration level of membrane coating.

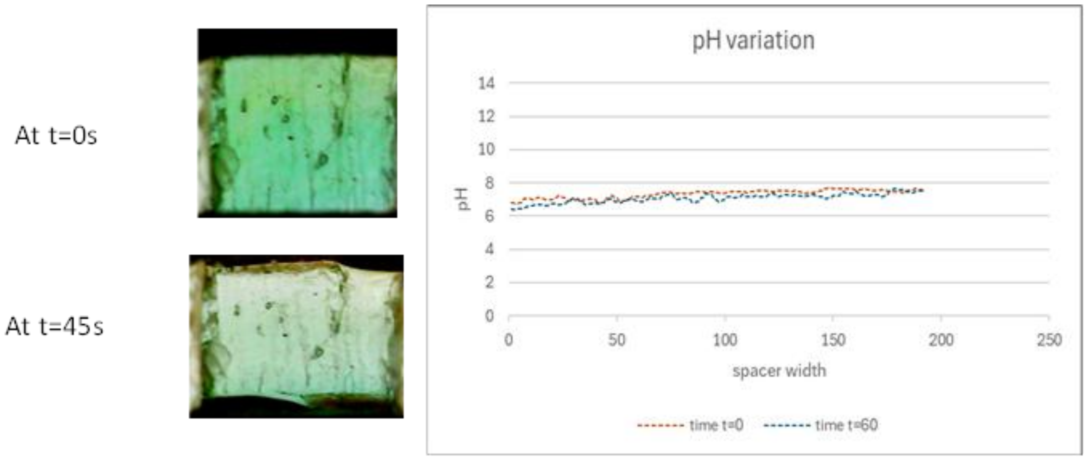

Figure 67 50% liquid membrane coated reactor snapshot and pH variation. Reactor Size:1 mm

Liquid membrane-coated electrode sheets with a 50% concentration were used in this microreactor. Video snapshots were analysed at two different times. Initially, at *t=0s*, the pH was 6.82, and it was consistent across the reactor spacer width. At *t=45s*, the pH was 6.44. The dye colour pattern Figure 67 was similar in all 2 different timings throughout the reactor spacer width. This characteristic was similar to sheet membrane, and there was no significant pH change, indicating that no Faradaic reaction occurred.

6.4.5 75% Liquid Membrane Coated AC

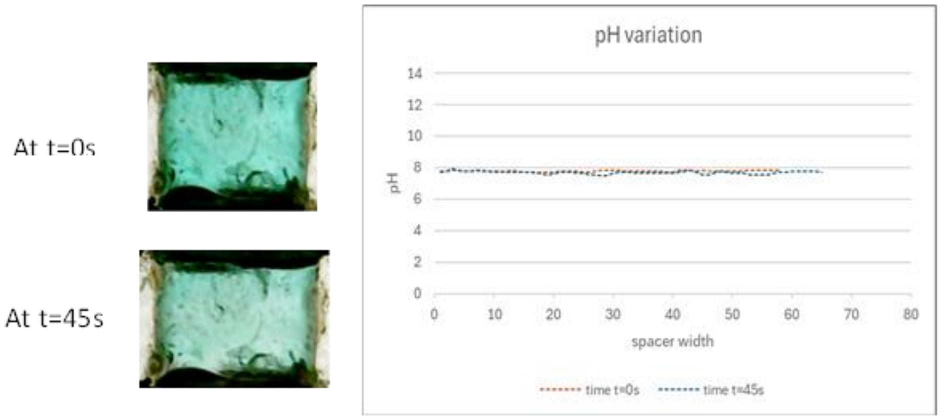

Figure 68 75% liquid membrane coated reactor snapshot and pH variation. Reactor Size: 1 mm

Liquid membrane-coated electrode sheets with 75% concentration were used in this microreactor. Video snapshots were analysed at two different time points. Initially, at *t=0s,* the pH was 6.8, and it was consistent across the reactor spacer width. At *t=45s,* the pH was 6.4. The dye colour pattern Figure 68 was similar in all two different timings throughout the reactor spacer width. This behaviour was similar to sheet membrane, there was no significant pH change, it was considered no Faradaic reaction occurred.

6.4.6 Graphite with 100% Liquid Membrane Coated

Upon completion of testing all the AC electrodes from maximum to minimum concentration of membrane coating, the membrane coating checked in plain graphite sheet electrode, coating and curing done as per Section 6.2.5

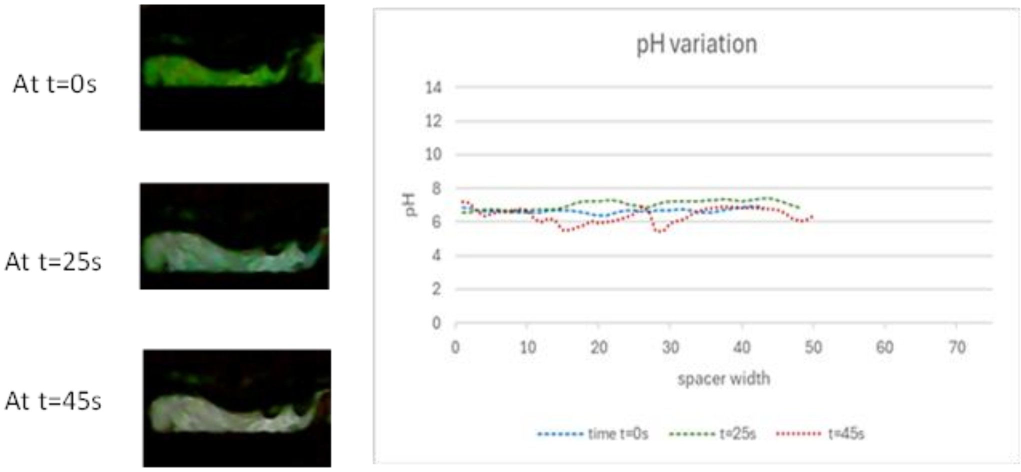

Figure 69 100% liquid membrane coated reactor snapshot and pH variation. Reactor Size:500-micron

Highly conductive graphite electrodes coated with a 100% liquid membrane were used in this microreactor. Video snapshots were examined at three different time points. Initially, at *t=0s,* the pH was 6.8 and it was consistent across the reactor spacer width. At t=25s, the pH was 6.53; further at t=45s, the pH value was 7.21. At *t=45s,* there was a minor fluctuation was seen in the middle of the spacer; it was assumed to be noisy data. The dye colour pattern Figure 69 was similar in all 3 different timings throughout the reactor spacer width. This performance was similar to that of a sheet membrane; there was no significant pH change, and it was considered that no Faradaic reaction occurred.

SEM images Figure 70 of the graphite electrode coated with a membrane were taken to confirm the presence of a membrane layer.

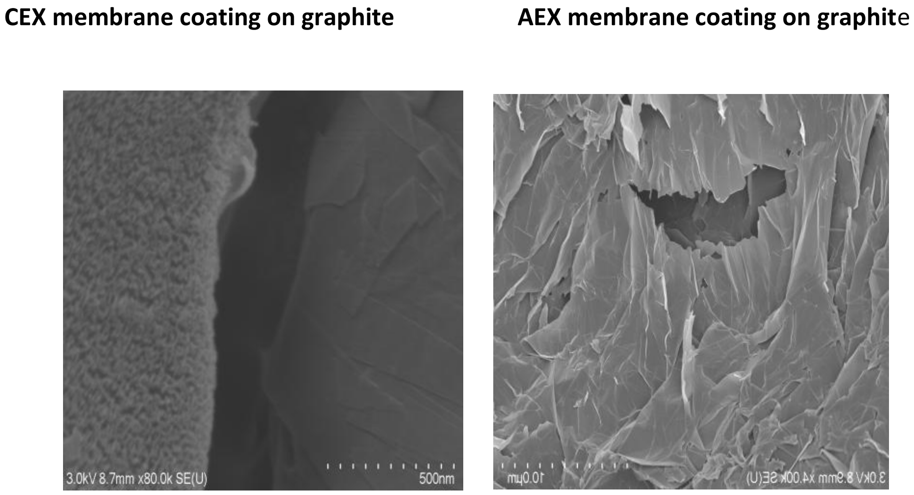

CEX membrane coating on graphite

AEX membrane coating on graphite

Figure 70 Graphite electrode with 100% IEX membrane coating

6.4.7 Plain Graphite

Plain graphite electrodes were utilized in this microreactor to compare it with the previous reactor, avoiding membrane interference.

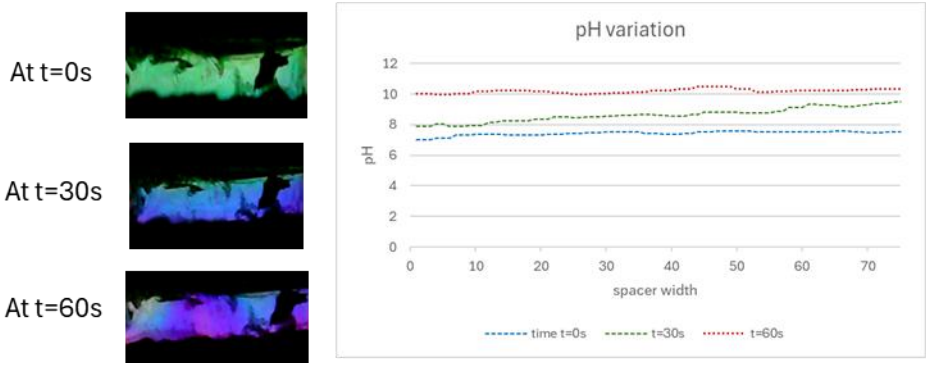

Figure 71 Plain graphite reactor snapshot and pH variation. Reactor Size:500-micron

Microreactor reactions were recorded, and video snapshots were analysed at 3 different timings. Initially, at *t=0s*, the pH was 7.0, and it was consistent across the reactor spacer width. At *t=30s* the pH was 7.9. A pink colour was observed at the cathode electrode side. Which began shifting upwards and across the channel, confirming a high pH region in the reactor further at *t=60s* pH value peaked at 10.04. The distinguishable dye colour pattern Figure 71 was evident at 3 different short intervals throughout the reactor spacer width. This behaviour confirmed significant pH change, leading to the conclusion that a Faradaic reaction occurred.

6.4.8 Plain Activated Carbon Sheet

In this experiment stage, we integrated activated carbon sheets free from membrane coatings into the microreactor for a side-by-side comparison with graphite. The results of this reaction were quite revealing.

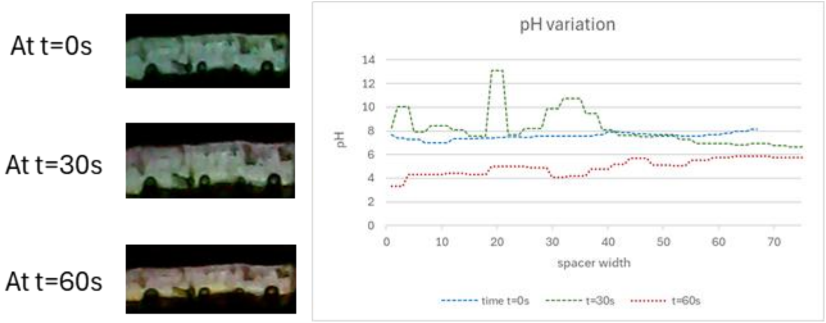

Figure 72 Industrial activated carbon sheet reactor. Reactor Size: 250 micron 3.5V

Industrial-activated carbon sheets were used in this microreactor. Video snapshots were analysed at 3 different timings. Initially, at *t=0s*, the pH was 6.7, and it was consistent across the reactor spacer width. At *t=30s* the pH was 8.2. An orange colour was observed at the anode electrode side. Which began shifting upwards and across the channel, confirming a low pH region in the reactor further; at *t=60s,* the pH value dropped to its lowest 3.3. The distinguishable dye colour pattern Figure 72 was evident at 3 different short intervals throughout the reactor spacer width. This behaviour confirmed significant pH change, leading to a conclusion that a Faradaic reaction occurred.

The next experiment was set to check the reaction rate at a faster rate by increasing the potential difference at 4.0 V

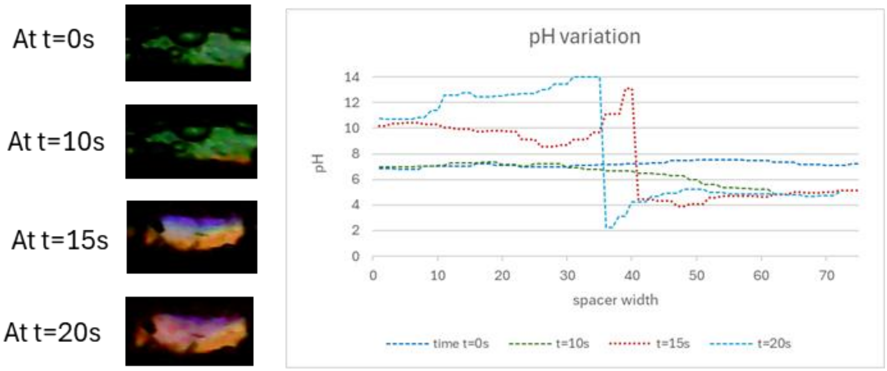

Figure 73 Activated carbon reactor snapshot and pH variation Reactor Size: 250 micron at 4.0 V

Industrial-activated carbon sheets were used in this microreactor. Video snapshots were analysed at 4 different timings. The reaction was rapid at 4.0V timings taken within 20 seconds. Initially, at *t=0s*, the pH was 6.8, and it was consistent across the reactor spacer width. At *t=10s,* the pH was 6.9. A pink colour was observed at the cathode electrode side. Which began shifting upwards and across the channel, confirming a high pH region in the reactor further at *t=15s,* pH value peaked at 10.2, *t=20s,* pH value further raised 10.8. At *t=20s,* the pH variation across the spacer from 14 to 3.9, A beautiful complete spectra were observed (Figure 73). It displayed all pH ranges within the reactor width. This behaviour confirmed significant pH change, leading to the conclusion that a fast Faradaic reaction occurred.

6.4.9 Activated Carbon Sheet with 250μm Reactor

This experiment was carried out to check the pH variation across the reactor at 2.0V applied electrical potential.

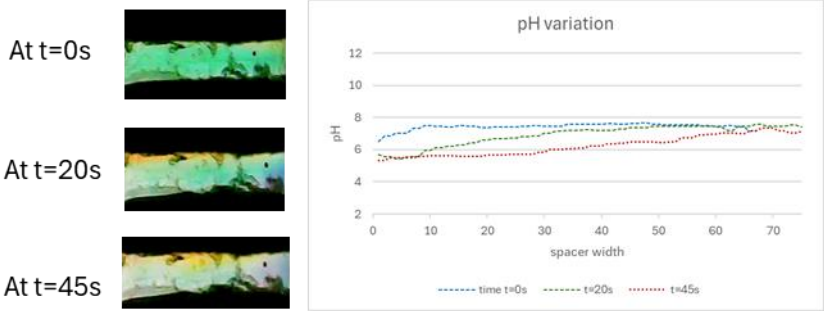

Figure 74 Activated carbon reactor with pH variation. Reactor Size: 250micron

In this experiment activated carbon sheets were used in this microreactor. Video snapshots were analysed at 3 different timings. Reaction snapshots at taken from 0 to 45 seconds. Initially, at *t=0s,* the pH was 6.7 and it was consistent across the reactor spacer width. At *t=20s* the pH was 5.4. An orange colour was observed at the anode electrode side., confirming a low pH region in the reactor further at *t=20s* pH value dropped to 5.3, At *t=45s,* the pH value further dropped to 5.3. At t=25s, the pH variation across the spacer from 5.3 to 7.4, A spectra (Figure 74) with orange-green and pale pink was observed. It displayed all pH ranges within the reactor width. This behaviour confirmed significant pH change, leading to a conclusion that a Faradaic reaction occurred.

6.5 Micro Reactor Experiment Results

The microreactor experiment results provide significant insights into how electrode materials and membrane applications influence the faradaic reaction and pH variation across the microreactor region.

Table 16 Microreactor Results

Electrode material	Membrane Application	Faradaic Reaction	pH spectrum	Rate of formation
Industrial AC sheet	100% Liquid membrane application	Nil	Nil	Nil
Industrial AC sheet	75% Liquid membrane application	Nil	Nil	Nil
Industrial AC sheet	50% Liquid membrane application	Nil	Nil	Nil
Industrial AC sheet	25% Liquid membrane application	Nil	Nil	Nil
Industrial AC sheet	12.5% Liquid membrane application	Nil	Nil	Nil
GPC AC sheet	100% Liquid membrane application	Nil	Nil	Nil
Graphite (500micron)	100% Liquid membrane application	Nil	Nil	Nil
Industrial AC sheet	Double membrane	Nil	Nil	Nil
Industrial AC sheet	Single membrane	Yes	Yes	Slow
Plain Graphite	No membrane	Yes	Yes	Rapid

Table 16 Micro reactor Results present important observations from the experiment conducted on CDI and MCDI arrangements.

Graphite Electrode microreactor:

The use of plain graphite electrodes without a membrane resulted in a faster faradaic reaction, as described in section 2.4.

Industrial AC electrodes:

Faradaic reactions were observed in AC electrodes. In contrast, the membrane-coated electrodes acted as a barrier to Faradaic reactions, as noted in the literature review section. In the case of graphite, the uniform coating influenced the performance of the cell during electrolysis and impacted overall cell efficiency. No pH spectra were detected. In activated carbon, up to 12.5% membrane coating, Faradaic reactions were absent, corroborating the findings of the research team outlined in Section 2.4.

6.6 Microreactor Problems and Recommendations

Developing and constructing the CDI microreactor to allow desirable experiments presented unique problems.

Electrolyte leaking from the reactor during experiments shortened its run time. To solve this, the reactor cell was wrapped with Teflon tape.

The reactor's microscale made dispensing electrolytes and UI fluids difficult to do manually. A manual syringe with a needle made the carbon electrode membranes susceptible to damage. This was solved by mounting the syringe and needle onto a 3-axis micromanipulator platform adjacent to the reactor platform.

The UI dye would absorb into the carbon membranes within a limited number of runs. This can be solved by reducing the cross-section surface area facing each carbon membrane electrode and increasing the UI dye concentration. An alternative reactor with these characteristics not used in this study exhibited improved dye colour retention.

When too much electrolyte was added to the reactor, it formed a convex meniscus, resulting in optical artifacts. To avoid this, the electrolyte was kept below the top edge of the reactor.

Some outstanding problems with potential solutions had yet to be fully implemented. Throughout this study, there was a growing need for a more precise steady-flow method of UI/electrolyte delivery via needle-on syringe. Potential solutions included a hand-operated syringe-screw mechanism and a computer-operated stepper motor syringe-screw mechanism.

6.7 Discussion

The results from microreactor experiments explained important information regarding the electrode material choice, membrane configuration on faradic reaction, and pH variations. The microreactor system effectively indicated the real-time reaction with respect to time in CDI cells. Adsorption desorption cycles reversed and the exact opposite spectra reversal from cathode to anode and vise versa were observed in the graphite/AC CDI microreactor system. Minor UI dye adsorption was observed only in the activated carbon sheets during the initial stage, likely due to the physical adsorption of dye by the porous carbon. Experiment observations were carried out for the first 2 cycles of the CDI operations, due to the physical adsorption effect.

Graphite electrodes:

First, we see the plain graphite, these electrodes exhibited a clear faradaic reaction, significant pH variation, and a rapid rate of gas bubble formation. This indicated the critical role of CDI membranes acting as an additional barrier suppressing the faradic reaction. The absence of the membrane allowed free proton movement and rapid reaction kinetics, resulting in a varying pH range in the reactor.

AC electrodes:

When we investigated AC sheets results, the double membrane configuration experiment results supported that the double layer of membrane provision suppressed the electrochemical reaction. AC electrodes without membranes produced a pH variation in the reactor, the rate of reaction was slower than the graphite electrode. The results confirm membrane layer significantly suppress the faradaic process regardless of type of carbon used as an electrode.

6.8 Conclusion

The study highlighted the role of DOTH, the proton movement within the spacer channel of CDI electrode was visualized and corresponding pH range was confirmed by the UI dye indicator. This approach, which combined colorimetric analysis using pH-sensitive dye formulation integrated with a micro fluidic device, effectively provided insights into localized chemical environment between electrodes. These values follow the correlation with spread in MATLAB function conversion. As mentioned by (Tang, He et al. 2017), our study exactly matched the faradaic reaction characteristics of CDI pH value of 4 to 12 during the CDI and mCDI operation as per graph in Figure 16 .

Key findings were;

- Development of a stronger dye for DOTH: A stable relationship between pH -Hue established,
- Validation of Dye: Formulated UI dye exhibits stable pH-Hue relationship, and remained consistence, this validates the reliability of real-time pH monitoring,

- Membrane configuration: Varying concentration of membrane application and testing in CDI proved even a minimal coating of 12.5% membrane inhibits the proton movement from carbon to spacer channel under similar operating conditions compared with graphite and plain AC sheets.

The experiment results are in relation to research carried out by Kovalsky et al, Lee et al, section 2.4. In conclusion, this study provides a real-time optical observation method for advanced diagnostics in CDI technology. In depth research and analysis in this section can significantly enhance the design and performance of CDI and mCDI cells. This development is crucial for ensuring the effectiveness and extended service duration.

7 Future work

There are several areas for improvement in the future, such as the development of a continuous flow cell reactor arrangement for the microreactor DOTH experiment to visualise Faradaic reactions in the CDI electrode. This would require a redesign of the system to include a precision fluid delivery system. Such a design would enable the observation of CDI under conditions more similar to how a full cell operates in an industrial module.

The four key areas this research can pursue for further development in the future,

1. Enhanced Flow Cell Arrangement for the Microreactor DOTH Experiment

Investigate improvements in the flow cell design to enable better visualisation and understanding of Faradaic reactions occurring in the CDI electrode. Enhancements in this area will help optimize system performance and provide insights into the underlying electrochemical processes.

2. Cost-effective Integration of CDI and mCDI in Industrial CDI Stacks

Explore the feasibility of combining standard CDI and mCDI modules in industrial-scale stacks. The research will focus on optimising this combination for efficient descaling of the mCDI section, potentially reducing costs while maintaining high desalination efficiency.

3. Advancements in CDI for Electrolyser Development

Investigate further improvements to the CDI section with the goal of developing it into a CDI electrolyser. This research will involve optimising the system for both desalination and energy recovery, thereby expanding the potential applications of CDI technology.

4. Membrane Material and Thickness Optimization

Study various membrane materials and their thicknesses to achieve a balance between minimising undesired reactions and enhancing ion transport efficiency. This research is critical for improving the overall performance of CDI systems, particularly regarding energy efficiency and longevity.

8 References:

Al-Rajabi, M. M., F. A. Abumadi, T. Laoui, M. A. Atieh and K. A. Khalil (2024). "Capacitive deionization for water desalination: Cost analysis, recent advances, and process optimization." Journal of Water Process Engineering **58**: 104816.

Anderson, M. A., A. L. Cudero and J. Palma (2010). "Capacitive deionization as an electrochemical means of saving energy and delivering clean water. Comparison to present desalination practices: Will it compete?" Electrochimica Acta **55**(12): 3845-3856.

Arulrajan, A., J. Dykstra, A. Wal and S. Porada (2021). "Unravelling pH Changes in Electrochemical Desalination with Capacitive Deionization." Environmental Science & Technology **XXXX**.

Bales, C., P. Kovalsky, J. Fletcher and T. Waite (2019). "Low cost desalination of brackish groundwaters by Capacitive Deionization (CDI) – Implications for irrigated agriculture." Desalination **453**: 37-53.

Behnam, P., M. Faegh and M. Khiadani (2022). "A review on state-of-the-art applications of data-driven methods in desalination systems." Desalination **532**: 115744.

Chen, L., X. Yin, L. Zhu and Y. Qiu (2018). "Energy recovery and electrode regeneration under different charge/discharge conditions in membrane capacitive deionization." Desalination **439**: 93-101.

Church, J. A., N. J. White and J. R. Hunter (2006). "Sea-level rise at tropical Pacific and Indian Ocean islands." Global and Planetary Change **53**(3): 155-168.

CIE (2018). Colorimetry 2018.

Dykstra, J. (2018). Desalination with porous electrodes.

Dykstra, J., K. Keesman, M. Biesheuvel and A. Wal (2017). "Theory of pH changes in water desalination by capacitive deionization." Water Research **119**.

Energy, U. D. o. (2019). "Desalination."

Han, L., K. Karthikeyan and K. B. Gregory (2015). "Energy consumption and recovery in capacitive deionization using nanoporous activated carbon electrodes." Journal of The Electrochemical Society **162**(12): E282.

He, D., C. Wong, W. Tang, P. Kovalsky and T. Waite (2016). "Faradaic Reactions in Water Desalination by Batch-Mode Capacitive Deionization." Environmental Science & Technology Letters **3**.

Herald, N. (2024). "Elevated levels of arsenic in Auckland drinking water."

Hukka, J., T. Katko, H. Mattila, P. Pietila, S. Sandelin and O. Seppälä (2007). "Inadequacy of positivistic research to explain complexity of water management." International Journal of Water **3**.

Jameson, D. and L. M. Hurvich (1964). "Theory of brightness and color contrast in human vision." Vision Research **4**(1): 135-154.

Kim, Y.-J., J.-H. Kim and J.-H. Choi (2013). "Selective removal of nitrate ions by controlling the applied current in membrane capacitive deionization (MCDI)." Journal of Membrane Science **429**: 52–57.

Kovalsky, P. (2016). "Measurement of local pH in CDI."

Lee, J.-B., K.-K. Park, H.-M. Eum and C.-W. Lee (2006). "Desalination of a thermal power plant wastewater by membrane capacitive deionization." Desalination **196**(1): 125-134.

Martyr-Koller, R., A. Thomas, C.-F. Schleussner, A. Nauels and T. Lissner (2021). "Loss and damage implications of sea-level rise on Small Island Developing States." Current Opinion in Environmental Sustainability **50**: 245-259.

Narain, V. (2000). "India's water crisis: the challenges of governance." Water Policy **2**(6): 433-444.

Nave, C. R. R. (2024). "HyperPhysics." from http://hyperphysics.phy-astr.gsu.edu/hbase/vision/colsys.html.

Noor, A. (2023). "Demineralisation of dairy whey products using MCDI."

Nur, A., N. Nazriati, F. Fajaroh, A. Arthaningrum, I. Nurcahyani, D. Cipto and F. Kurniawan (2021). "Electrosynthesis of Cu/hydroxyapatite as the catalyst for hydrogen production via NaBH4 hydrolysis." IOP Conference Series: Materials Science and Engineering **1070**: 012023.

Ott, A. (2023). "Field Testing of mCDI Desalination for the Pacific Islands to Safeguard Against Climate Change."

Porada, S., L. Borchardt, M. Oschatz, M. Bryjak, J. S. Atchison, K. J. Keesman, S. Kaskel, P. M. Biesheuvel and V. Presser (2013). "Direct prediction of the desalination performance of porous carbon electrodes for capacitive deionization." Energy & Environmental Science **6**(12): 3700-3712.

Porada, S., R. Zhao, A. van der Wal, V. Presser and P. M. Biesheuvel (2013). "Review on the science and technology of water desalination by capacitive deionization." Progress in Materials Science **58**(8): 1388-1442.

Qin, M., A. Deshmukh, R. Epsztein, S. K. Patel, O. M. Owoseni, W. S. Walker and M. Elimelech (2019). "Comparison of energy consumption in desalination by capacitive deionization and reverse osmosis." Desalination **455**: 100-114.

Richards, J., T. Chambers, S. Hales, M. Joy, T. Radu, A. Woodward, A. Humphrey, E. Randal and M. G. Baker (2022). "Nitrate contamination in drinking water and colorectal cancer: Exposure assessment and estimated health burden in New Zealand." Environmental Research **204**: 112322.

Saquib, S., A. Gupta and A. Joshi (2022). Chapter 21 - Emerging water crisis: Impact of urbanization on water resources and constructed wetlands as a nature-based solution (NbS). Current Directions in Water Scarcity Research. A. L. Srivastav, S. Madhav, A. K. Bhardwaj and E. Valsami-Jones, Elsevier. **6:** 447-468.

Shi, H. (1996). "Activated carbons and double layer capacitance." Electrochimica Acta **41**(10): 1633-1639.

stats.gov.nz (2020). "Ground water quality Indiacator."

Talebi, S., G. Q. Chen, B. Freeman, F. Suarez, A. Freckleton, K. Bathurst and S. E. Kentish (2019). "Fouling and in-situ cleaning of ion-exchange membranes during the electrodialysis of fresh acid and sweet whey." Journal of Food Engineering **246**: 192-199.

Tang, W., D. He, C. Zhang, P. Kovalsky and T. D. Waite (2017). "Comparison of Faradaic reactions in capacitive deionization (CDI) and membrane capacitive deionization (MCDI) water treatment processes." Water Research **120**: 229-237.

UNSGD-6 (2023). "SDG-6."

WHO, U. (2019). 1 in 3 people globally do not have access to safe drining water.

Zhai, Z., L. Zhang, T. Du, B. Ren, Y. Xu, S. Wang, J. Miao and Z. Liu (2022). "A review of carbon materials for supercapacitors." Materials & Design **221**: 111017.

Zhang, C., D. He, J. Ma, W. Tang and T. D. Waite (2018). "Faradaic reactions in capacitive deionization (CDI) - problems and possibilities: A review." Water Research **128**: 314-330.

9 Appendix

9.1 Development of CDI Technology

History of CDI technology from (Al-Rajabi, Abumadi et al. 2024)

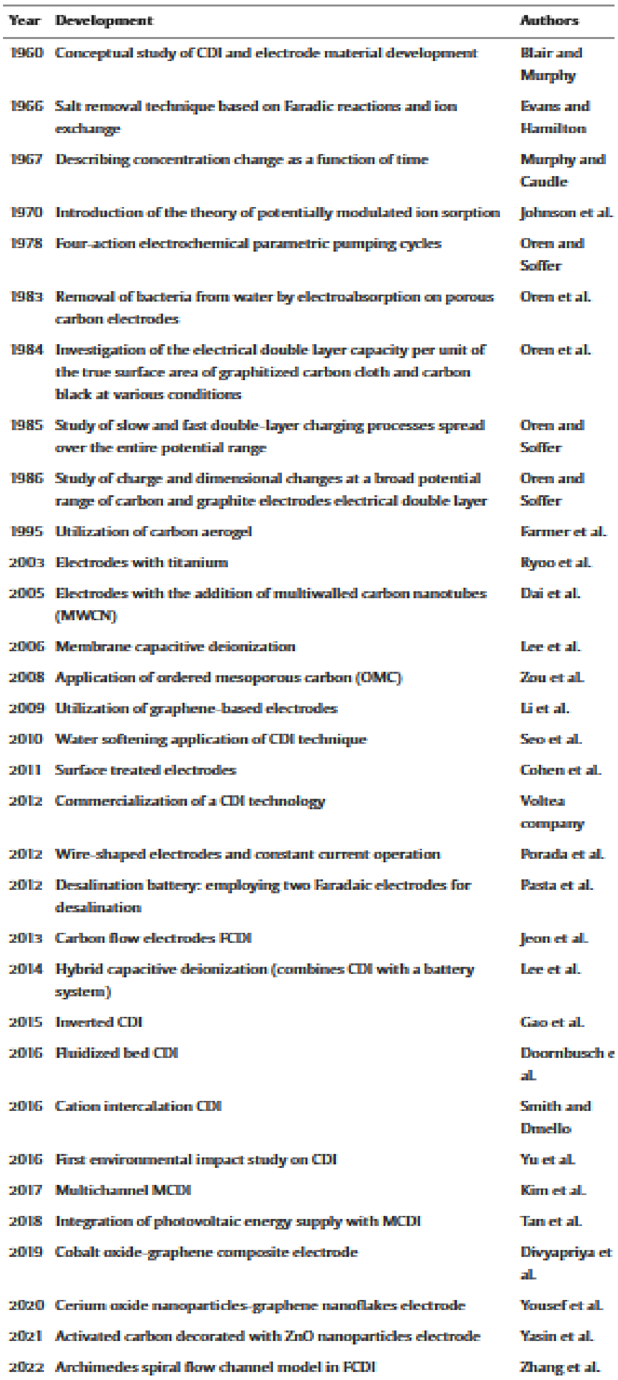

Year	Development	Authors
1960	Conceptual study of CDI and electrode material development	Blair and Murphy
1966	Salt removal technique based on Faradic reactions and ion exchange	Evans and Hamilton
1967	Describing concentration change as a function of time	Murphy and Caudle
1970	Introduction of the theory of potentially modulated ion sorption	Johnson et al.
1978	Four-action electrochemical parametric pumping cycles	Oren and Soffer
1983	Removal of bacteria from water by electroabsorption on porous carbon electrodes	Oren et al.
1984	Investigation of the electrical double layer capacity per unit of the true surface area of graphitized carbon cloth and carbon black at various conditions	Oren et al.
1985	Study of slow and fast double-layer charging processes spread over the entire potential range	Oren and Soffer
1986	Study of charge and dimensional changes at a broad potential range of carbon and graphite electrodes electrical double layer	Oren and Soffer
1995	Utilization of carbon aerogel	Farmer et al.
2003	Electrodes with titanium	Ryoo et al.
2005	Electrodes with the addition of multiwalled carbon nanotubes (MWCN)	Dai et al.
2006	Membrane capacitive deionization	Lee et al.
2008	Application of ordered mesoporous carbon (OMC)	Zou et al.
2009	Utilization of graphene-based electrodes	Li et al.
2010	Water softening application of CDI technique	Seo et al.
2011	Surface treated electrodes	Cohen et al.
2012	Commercialization of a CDI technology	Voltea company
2012	Wire-shaped electrodes and constant current operation	Porada et al.
2012	Desalination battery: employing two Faradaic electrodes for desalination	Pasta et al.
2013	Carbon flow electrodes FCDI	Jeon et al.
2014	Hybrid capacitive deionization (combines CDI with a battery system)	Lee et al.
2015	Inverted CDI	Gao et al.
2016	Fluidized bed CDI	Doornbusch e al.
2016	Cation intercalation CDI	Smith and Dmello
2016	First environmental impact study on CDI	Yu et al.
2017	Multichannel MCDI	Kim et al.
2018	Integration of photovoltaic energy supply with MCDI	Tan et al.
2019	Cobalt oxide-graphene composite electrode	Divyapriya et al.
2020	Cerium oxide nanoparticles-graphene nanoflakes electrode	Yousef et al.
2021	Activated carbon decorated with ZnO nanoparticles electrode	Yasin et al.
2022	Archimedes spiral flow channel model in FCDI	Zhang et al.

9.2 Capacitance Test of Carbon Material (Shi 1996)

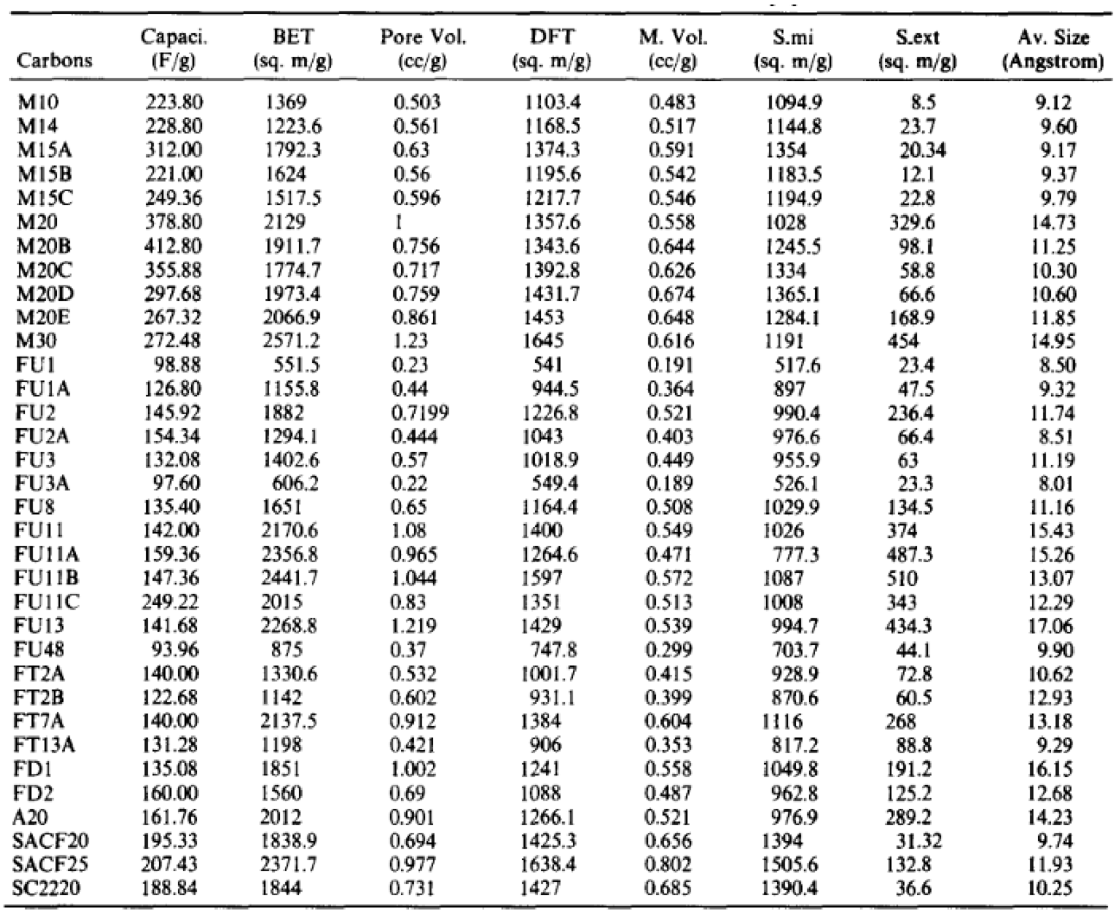

Carbons	Capaci. (F/g)	BET (sq. m/g)	Pore Vol. (cc/g)	DFT (sq. m/g)	M. Vol. (cc/g)	S.mi (sq. m/g)	S.ext (sq. m/g)	Av. Size (Angstrom)
M10	223.80	1369	0.503	1103.4	0.483	1094.9	8.5	9.12
M14	228.80	1223.6	0.561	1168.5	0.517	1144.8	23.7	9.60
M15A	312.00	1792.3	0.63	1374.3	0.591	1354	20.34	9.17
M15B	221.00	1624	0.56	1195.6	0.542	1183.5	12.1	9.37
M15C	249.36	1517.5	0.596	1217.7	0.546	1194.9	22.8	9.79
M20	378.80	2129	1	1357.6	0.558	1028	329.6	14.73
M20B	412.80	1911.7	0.756	1343.6	0.644	1245.5	98.1	11.25
M20C	355.88	1774.7	0.717	1392.8	0.626	1334	58.8	10.30
M20D	297.68	1973.4	0.759	1431.7	0.674	1365.1	66.6	10.60
M20E	267.32	2066.9	0.861	1453	0.648	1284.1	168.9	11.85
M30	272.48	2571.2	1.23	1645	0.616	1191	454	14.95
FU1	98.88	551.5	0.23	541	0.191	517.6	23.4	8.50
FU1A	126.80	1155.8	0.44	944.5	0.364	897	47.5	9.32
FU2	145.92	1882	0.7199	1226.8	0.521	990.4	236.4	11.74
FU2A	154.34	1294.1	0.444	1043	0.403	976.6	66.4	8.51
FU3	132.08	1402.6	0.57	1018.9	0.449	955.9	63	11.19
FU3A	97.60	606.2	0.22	549.4	0.189	526.1	23.3	8.01
FU8	135.40	1651	0.65	1164.4	0.508	1029.9	134.5	11.16
FU11	142.00	2170.6	1.08	1400	0.549	1026	374	15.43
FU11A	159.36	2356.8	0.965	1264.6	0.471	777.3	487.3	15.26
FU11B	147.36	2441.7	1.044	1597	0.572	1087	510	13.07
FU11C	249.22	2015	0.83	1351	0.513	1008	343	12.29
FU13	141.68	2268.8	1.219	1429	0.539	994.7	434.3	17.06
FU48	93.96	875	0.37	747.8	0.299	703.7	44.1	9.90
FT2A	140.00	1330.6	0.532	1001.7	0.415	928.9	72.8	10.62
FT2B	122.68	1142	0.602	931.1	0.399	870.6	60.5	12.93
FT7A	140.00	2137.5	0.912	1384	0.604	1116	268	13.18
FT13A	131.28	1198	0.421	906	0.353	817.2	88.8	9.29
FD1	135.08	1851	1.002	1241	0.558	1049.8	191.2	16.15
FD2	160.00	1560	0.69	1088	0.487	962.8	125.2	12.68
A20	161.76	2012	0.901	1266.1	0.521	976.9	289.2	14.23
SACF20	195.33	1838.9	0.694	1425.3	0.656	1394	31.32	9.74
SACF25	207.43	2371.7	0.977	1638.4	0.802	1505.6	132.8	11.93
SC2220	188.84	1844	0.731	1427	0.685	1390.4	36.6	10.25

9.3 Appendix – PhreeqC Database Additions

```
SOLUTION_MASTER_SPECIES
#
#element    species alk    gfw_formula   element_gfw
In          In-     2.0    In            318.328
Bp          Bp-     2.0    Bp            624
Mr          Mr-     2.0    Mr            269

SOLUTION_SPECIES

In- + H+ = HIn
        -log_k  9.7
Bp- + H+ = HBp
        -log_k  7.0
Mr- + H+ = HMr
        -log_k  5.2
```

9.4 Appendix – PhreeqC Input File

```
SOLUTION 40
   temp      25
   pH        4
   pe        4
   redox     pe
   units     mol/kgw
   density   1
   In       0.001
   Bp        0.001
   Mr        0.0001
   -water    1 # kg

SOLUTION 45
   temp      25
   pH        4.5
   pe        4
   redox     pe
   units     mol/kgw
   density   1
   In       0.001
   Bp        0.001
   Mr        0.0001
   -water    1 # kg

SOLUTION 50
   temp      25
   pH        5
```

```
   pe        4
   redox     pe
   units     mol/kgw
   density   1
   In        0.001
   Bp        0.001
   Mr        0.0001
   -water    1 # kg

SOLUTION 55
   temp      25
   pH        5.5
   pe        4
   redox     pe
   units     mol/kgw
   density   1
   In        0.001
   Bp        0.001
   Mr        0.0001
   -water    1 # kg

SOLUTION 60
   temp      25
   pH        6
   pe        4
   redox     pe
   units     mol/kgw
   density   1
   In        0.001
   Bp        0.001
   Mr        0.0001
   -water    1 # kg

SOLUTION 65
   temp      25
   pH        6.5
   pe        4
   redox     pe
   units     mol/kgw
   density   1
   In        0.001
   Bp        0.001
   Mr        0.0001
   -water    1 # kg

SOLUTION 70
   temp      25
   pH        7
   pe        4
```

```
    redox     pe
    units     mol/kgw
    density   1
    In        0.001
    Bp        0.001
    Mr        0.0001
    -water    1 # kg

SOLUTION 75
    temp      25
    pH        7.5
    pe        4
    redox     pe
    units     mol/kgw
    density   1
    In        0.001
    Bp        0.001
    Mr        0.0001
    -water    1 # kg

SOLUTION 80
    temp      25
    pH        8
    pe        4
    redox     pe
    units     mol/kgw
    density   1
    In        0.001
    Bp        0.001
    Mr        0.0001
    -water    1 # kg

SOLUTION 85
    temp      25
    pH        8.5
    pe        4
    redox     pe
    units     mol/kgw
    density   1
    In        0.001
    Bp        0.001
    Mr        0.0001
    -water    1 # kg

SOLUTION 90
    temp      25
    pH        9
    pe        4
    redox     pe
```

```
    units     mol/kgw
    density   1
    In        0.001
    Bp        0.001
    Mr        0.0001
    -water    1 # kg

SOLUTION 95
    temp      25
    pH        9.5
    pe        4
    redox     pe
    units     mol/kgw
    density   1
    In        0.001
    Bp        0.001
    Mr        0.0001
    -water    1 # kg

SOLUTION 100
    temp      25
    pH        10
    pe        4
    redox     pe
    units     mol/kgw
    density   1
    In        0.001
    Bp        0.001
    Mr        0.0001
    -water    1 # kg

SOLUTION 105
    temp      25
    pH        10.5
    pe        4
    redox     pe
    units     mol/kgw
    density   1
    In        0.001
    Bp        0.001
    Mr        0.0001
    -water    1 # kg

SOLUTION 110
    temp      25
    pH        11
    pe        4
    redox     pe
    units     mol/kgw
```

```
density   1
In        0.001
Bp        0.001
Mr        0.0001
-water    1 # kg
```

9.5 MATLAB Code for Image Analysis (pH Variation in the Microreactor)

9.5.1 Image Selection and Conversion into MATLAB

```
a=imread('IN251 11.PNG');
S=size(a);
f5=figure('Name','Reactor Snippet')
figure(f5)
image(a);
drawnow();
imgx=size(a,2);
```

9.5.2 Cross-section Channel in the Reactor is Selected

```
fprintf('select pixel column from 1 to %.0f of snip',imgx);
c=input(': ');
f2Title=sprintf('Column %.0f of Snippet',c);
f2=figure('Name',f2Title);
figure(f2)
image(a(:,c,:))

r=a(:,c,1);
g=a(:,c,2);
b=a(:,c,3);
```

9.5.3 RGB plots of the Interested Reactor Column

```
f3=figure('Name','rgb plots of snippet column');
figure(f3)
plot(r, 'r')
hold on
plot(g, 'g')
plot(b, 'b')
hsvCol=zeros(size(a,1,4));
hsvCol(:,:,1:3)=rgb2hsv(r,g,b);

hsvCol2(S(1),4)=0;
for i=1:S(1)
    hsvCol2(i,1)=a(i,c,1);
    hsvCol2(i,2)=a(i,c,2);
    hsvCol2(i,3)=a(i,c,3);
end
```

9.5.4 RGB Reference Data File

```
%rgb colours from phreeqc pH 4-11 table
%should change this to proper spiral
%{
rgbRef=[216 118 67
216 118 67
229 170 135
238 199 174
246 226 213
221 240 209
189 227 166
146 200 230
94 144 210
94 144 210
94 144 210
52 91 146
52 91 146
103 54 152
103 54 152];
%}

rgbRef=[233.1364  209.0152  201.4697
  240.4545  214.1901  202.1736
  223.5207  228.7934  176.5207
  154.0000  208.2975  183.8595
  117.4298  199.6033  193.0579
   97.3636  184.4463  201.2397
  148.3506   39.8052  179.2035
   88.6349   16.8452  103.5159]
```

9.5.5 Conversion of RGB to Hue Saturation Value Data and Creating a Polar Plot

```
%converting to hsv
hsvRef=zeros(size(rgbRef,1),4);
hsvRef(:,1:3)=rgb2hsv(rgbRef(:,1),rgbRef(:,2),rgbRef(:,3));
hsvRef(:,4)=4:1:11;

%hsv polar plotting
f4=figure('Name','polar HSV plot');
figure(f4)
polarplot(2*pi*hsvCol(:,:,1),hsvCol(:,:,2),'-or')
hold on
polarplot(2*pi*hsvCol(1,:,1),hsvCol(1,:,2),'-ob')
polarplot(2*pi*hsvCol(size(hsvCol,1),:,1),hsvCol(size(hsvCol,1),:,2),'-og')
polarplot(2*pi*hsvRef(:,1),hsvRef(:,2),'-ok')
legend('sample','start(top of snip)','end(bottom of snip)','reference')

%checks nearest colour in hsvRef (phreeqc), and matches pH to hsvCol sample
for t=1:size(hsvCol,1)
    [value,index]=min(abs(hsvRef(:,1)-hsvCol(t)));
    hsvCol(t,:,4)=hsvRef(index,4);
end
```

9.5.6 The pH Variation Across the Reactor Plotted in a Graph

```
%results
fprintf('interpolated pH from reference (top to bottom of snippet):\n')
disp(hsvCol(:,:,4))

hsvCol3=hsvCol2(:,1:3)
ZZ=[];
Z=rgb2hsv(hsvCol3(:,1),hsvCol3(:,2),hsvCol3(:,3))
for i=1:S(1)

    ZZ(i,1)=Z(i,1,1);
    ZZ(i,2)=Z(i,1,2);
    ZZ(i,3)=Z(i,1,3);
end

figure
subplot(2,1,2)
subplot(2,1,1)
xx=S(1):-1:1;
yy=[];
for i=1:S(1)
yy(i)=5.9579*ZZ(i,1)^3.8833+9.0488*ZZ(i,1)^0.2390;
end
%yy=HSV2PH(ZZ(:,1));
subplot(2,1,2)
plot(yy,xx)
subplot(2,1,1)
image(a)

xlabel('pH')
title('pH Profile')
```

9.5.7 MATLAB Code for pH Spectrum RGB to HSV

```
A=imread('ph4.png')
mean(mean(A(:,:,1)))
mean(mean(A(:,:,2)))
mean(mean(A(:,:,3)))
[h,s,v]=rgb2hsv(254.8818,218,144)
```

9.6 SEM Image of IEX Membrane

9.6.1 AEM Coating in Activated Carbon Sheet

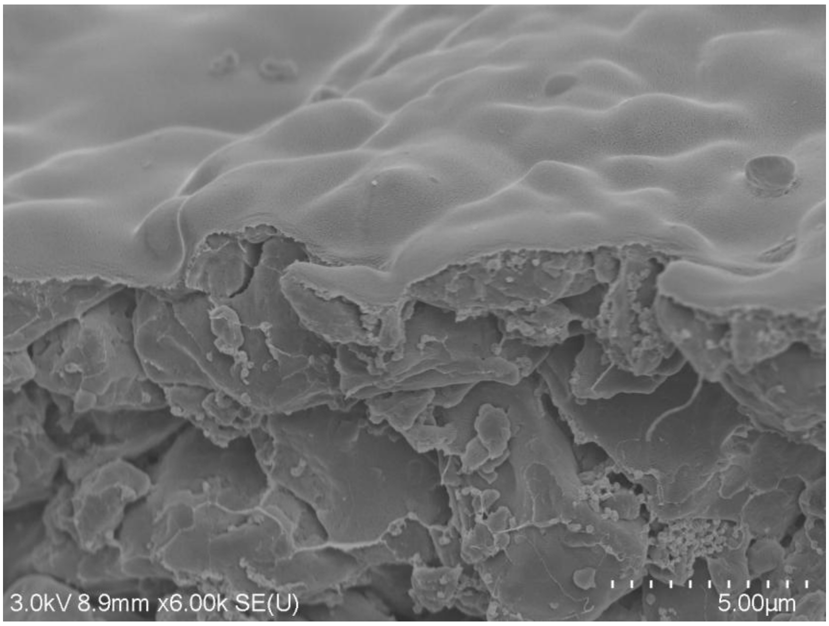

9.6.2 CEM Coating in Activated Carbon Sheet

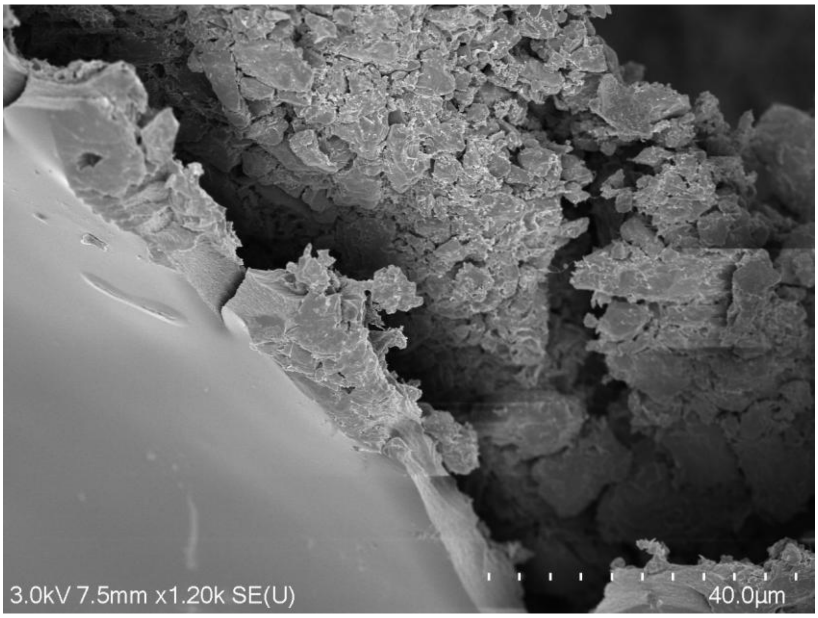

9.7 Images of Microreactor, Acrylic Sheet, Teflon Sealed Reactor